

---

Doctoral Dissertations

Student Theses and Dissertations

---

Spring 2012

## X-ray crystallography for the study of nickel and iron salicylaldimines

Carla Schmiesing Eribal

Follow this and additional works at: [https://scholarsmine.mst.edu/doctoral\\_dissertations](https://scholarsmine.mst.edu/doctoral_dissertations)

 Part of the [Chemistry Commons](#)

Department: Chemistry

---

### Recommended Citation

Eribal, Carla Schmiesing, "X-ray crystallography for the study of nickel and iron salicylaldimines" (2012). *Doctoral Dissertations*. 1814.

[https://scholarsmine.mst.edu/doctoral\\_dissertations/1814](https://scholarsmine.mst.edu/doctoral_dissertations/1814)

This thesis is brought to you by Scholars' Mine, a service of the Missouri S&T Library and Learning Resources. This work is protected by U. S. Copyright Law. Unauthorized use including reproduction for redistribution requires the permission of the copyright holder. For more information, please contact [scholarsmine@mst.edu](mailto:scholarsmine@mst.edu).

**X-RAY CRYSTALLOGRAPHY FOR THE STUDY OF  
NICKEL AND IRON SALICYLALDIMINES**

**by**

**CARLA SUE SCHMIESING ERIBAL**

**A DISSERTATION**

**Presented to the Graduate Faculty of the  
MISSOURI UNIVERSITY OF SCIENCE AND TECHNOLOGY**

**In Partial Fulfillment of the Requirements for the Degree**

**DOCTOR OF PHILOSOPHY**

**in**

**CHEMISTRY**

**2012**

**Approved by:**

**Ekkehard Sinn, Advisor  
Robert Aronstam  
Chariklia Sotiriou-Leventis  
Pericles Stavropoulos  
Jay Switzer**

## ABSTRACT

X-ray diffraction of single crystals has developed dramatically over the last century by combining fundamental theories of light, diffraction, and statistics to generate the complete, geometric structure of molecules. The quality of the resulting X-ray structure data are reported in  $R_1 < 5\%$ ,  $wR2 < 12\%$  and a goodness of fit value of one. This technique was applied specifically to the evaluation of the spin crossover (SCO) compound  $[\text{Fe}(\text{salpm})_2]\text{BF}_4 \cdot 0.5\text{EtOH}$  and how the molecule's geometry changed during a two-step thermal LS-HS conversion. The crystal structure was measured at 100, 175, 225, and 296 K to yield final  $R_1$  values of 0.047, 0.054, 0.051, and 0.058, respectively. The coordination bond lengths show the spin transitions occur between 100-175K at one crystallographically unique Fe and between 175-225K at the other Fe site. No strong long range interactions are found, suggesting a gradual spin transition. Reaction of Ni(N-alkyl-sal)<sub>2</sub> complexes with Ni(NO<sub>3</sub>)<sub>2</sub> form either nickel dimeric,  $[\text{Ni}(\text{Rsal})(\text{NO}_3)(\text{MeOH})]_2$  or trinuclear complexes,  $\text{Ni}_3(\text{Rsal})_4(\text{NO}_3)_2$ . The binuclear complexes, with orthogonal bridging ligands, show overall ferromagnetic interactions. The crystal structures for  $\text{Ni}_3(\text{Rsal})_4(\text{NO}_3)_2$  from methyl to benzyl were solved and indicate no steric restriction on formation for the series. The trinuclear compounds form an isosceles triangle of metal atoms with the isopropyl analog showing an overall antiferromagnetic interaction with  $J=+11.386$  and  $J_{23}=-13.891$ . Lastly, xanthene spirolactam derivatives were structurally analyzed to determine binding modes for their selective and sensitive ( $\mu\text{M}$ ) detection of metals  $\text{Cr}^{3+}$ ,  $\text{Fe}^{3+}$ ,  $\text{Ni}^{2+}$ ,  $\text{Co}^{2+}$  and the nerve gas mimic, dichlorophosphate.

## ACKNOWLEDGMENTS

My heartfelt appreciation to the Missouri University of Science and Technology for a Chancellor's Fellowship for my graduate study, and specifically the Missouri S&T Chemistry department staff and faculty for their extensive flexibility throughout my study. I would like to thank my advisor, Dr. Ekkehard Sinn for his continued support, academic freedom and general good cheer. The American Crystallographic Association generously provided a summer course travel grant for which I am grateful. I would also like to thank Dr. Reinhard Paschke of Martin-Luther-Universität Halle-Wittenberg, Germany for his generous hospitality and financial support for a summer visiting research position. Thank you so much to the entire Department of Chemistry at Western Michigan University for treating me as one of their own, support and understanding during my research time there.

Extreme gratitude goes out to my current and previous group members both at Missouri S&T and Western Michigan. Most especially, Zahra Afrasiabi, who mentored and guided me during my first tumultuous years. Aruna Weerasinghe, who listened with a kind ear and for his constant, patient advice and support. Fasil Abebe and Mary Sajini Devadas, for their helpfulness in the lab and friendship out of the lab.

I would like to thank my entire family for their advice, love and support, especially my mother, Mary Jo Schmiesing, for her faithful and ever-present ear, without which I could not proceed. Lastly, thanks be to God, which by His grace and endless love protects and guides me every day of my life. May I not waste His blessing.

## TABLE OF CONTENTS

	Page
ABSTRACT .....	iii
ACKNOWLEDGMENTS .....	iv
LIST OF ILLUSTRATIONS.....	ix
LIST OF TABLES.....	xi
 SECTION	
1. INTRODUCTION .....	1
2. SINGLE CRYSTAL X-RAY DIFFRACTION.....	8
2.1. THEORY .....	8
2.1.1. Advent of X-rays .....	8
2.1.2. Diffraction .....	9
2.1.3. Intensities.....	12
2.1.4. The Phase Problem .....	15
2.1.4.1. Patterson.....	16
2.1.4.2. Direct methods .....	17
2.1.5. Symmetry.....	18
2.1.5.1. Lattice types and the unit cell .....	18
2.1.5.2. Point and space groups.....	20
2.1.5.3. Systematic absences.....	21
2.1.5.4. Symmetry in both spaces .....	22
2.1.6. Summary.....	22

2.2. PRACTICE.....	23
2.2.1. Sample .....	23
2.2.2. Diffractometer .....	25
2.2.3. Experimental Process .....	27
2.2.3.1. Obtaining the diffraction pattern.....	28
2.2.3.2. Analyzing the diffraction pattern .....	32
2.2.3.3. Refining the structure and results.....	36
3. TEMPERATURE EFFECTS ON X-RAY STRUCTURAL DETERMINATION OF A SPIN CROSS-OVER Fe(III) COMPLEX.....	39
3.1. INTRODUCTION .....	39
3.2. BACKGROUND OF SCO .....	41
3.2.1. Applications.....	41
3.2.2. Mechanism.....	42
3.2.3. Physical Methods to Study SCO .....	42
3.2.4. Chemical Changes that Affect SCO Behavior .....	45
3.3. EXPERIMENTAL.....	46
3.3.1. LS-LS 100K Structure Solution and Refinement .....	46
3.3.2. LS-HS 175K Structure Solution and Refinement.....	52
3.3.3. HS-HS 225K Structure Solution and Refinement .....	53
3.3.4. HS-HS 296K Structure Solution and Refinement .....	55
3.4. DISCUSSION.....	58
3.5. SUMMARY/CONCLUSION.....	66
4. APPLIED X-RAY STRUCTURE ELUCIDATION.....	68

4.1. INTRODUCTION .....	68
4.2. ABSOLUTE STRUCTURE .....	68
4.2.1. X-ray Dispersion.....	68
4.2.2. Absolute Structure Parameters .....	69
4.2.3. Example: 5,6-Dihydro-1,10-Phenanthroline Compounds .....	70
4.3. TWINNING.....	72
4.3.1. Types and Indications.....	72
4.3.2. Tools and Methods .....	75
4.3.3. Example: Hydrazinecarbothioamide Nickel Complex .....	77
4.4. SYMMETRY AMBIGUITY.....	79
5. NICKEL SALICYLALDIMINES.....	82
5.1. INTRODUCTION.....	82
5.2. MAGNETISM.....	84
5.2.1. Mononuclear Complexes.....	87
5.2.2. Binuclear Complexes.....	93
5.2.3. Trinuclear Complexes.....	96
5.3. LIGAND STERIC MEASUREMENT.....	97
5.4. EXPERIMENTAL.....	99
5.4.1. Synthesis.....	100
5.4.2. X-ray Structure Determination .....	104
5.4.3. Magnetic Measurements.....	104
5.5. EXPERIMENTAL.....	105
5.5.1. Synthesis and General Characterization .....	105

5.5.2. Binuclear Structures .....	108
5.5.3. Trinuclear Complexes.....	112
5.6. CONCLUSIONS .....	119
6. XANTHENE SPIROCYCLIC DETECTORS .....	122
6.1. INTRODUCTION.....	122
6.2. RHODAMINE-B FOR THE DETECTION OF Cr <sup>3+</sup> .....	123
6.3. ELECTRONIC EFFECTS ON THE DETECTION OF DCP.....	126
6.4. FLUOROSCEIN FOR THE DETECTION OF Ni <sup>2+</sup> AND Co <sup>2+</sup> .....	134
6.5. CONCLUSION .....	141
BIBLIOGRAPHY .....	143
VITA .....	155



## LIST OF ILLUSTRATIONS

Figure	Page
2.1. Interference of radiation from two slits at different scattering angles, $\theta$ [20] .....	10
2.2. Reflection of waves from planes of atoms .....	12
2.3. Atomic scattering factors, $f$ , for atoms or ions vs. $\sin \theta/\lambda$ .....	14
2.4. Bravais lattices.....	19
2.5. Eulerian geometry goniometer .....	26
2.6. Experimental steps of crystal structure determination .....	28
2.7. Equations of residual R-values.....	38
3.1. ORTEP diagram of of $[\text{Fe}(\text{salpm})_2]\text{BF}_4 \cdot 0.5\text{EtOH}$ .....	59
3.2. Unit cell dimensions and volume of $[\text{Fe}(\text{salpm})_2]\text{BF}_4 \cdot 0.5\text{EtOH}$ .....	62
4.1. Structure of $[\text{Cu}(\text{HAP})_2 \text{CNCH}_3]\text{CF}_3\text{SO}_3$ .....	71
4.2. Example diffraction patterns of a twinned crystal.....	73
4.3. ORTEP diagram of $\text{Ni}_2\text{L}_2(\text{py}) \cdot \text{DMSO}$ .....	79
4.4. ORTEP diagram $\text{Cu}(\text{C}_{26}\text{H}_{20}\text{N}_6\text{O}_4)_2$ .....	81
5.1. d orbital splitting in different ligand fields.....	88
5.2. Splitting of energy terms of a $d^8$ ion.....	91
5.3. Energy level splitting of a $S_1=S_2=1$ binuclear complex .....	95
5.4. Geometric definition of a solid angle, $\Omega = A/r^2$ .....	98
5.5. Formation of binuclear and trinuclear complexes .....	105
5.6. ORTEP diagram of $[\text{Ni}(\text{benzylsal})(\text{NO}_3)(\text{MeOH})]_2$ .....	109
5.7. Effective magnetic moment per Ni atom of $[\text{Ni}(\text{iprsal})(\text{NO}_3)(\text{MeOH})]_2$ .....	111

5.8. Molecular structure of $\text{Ni}_3(\text{etsal})_4(\text{NO}_3)_2$ .....	114
5.9. Coupling scheme applied to the trinuclear complexes.....	116
5.10. Energy level for isosceles triangle arrangement of 3 $S=1$ spin centers.....	117
5.11. Effective magnetic moment of $\text{Ni}_3(\text{iprsal})_4(\text{NO}_3)_2$ .....	118
6.1. Structure of sensor <b>1</b> .....	124
6.2. Fluorescence changes of <b>1</b> .....	126
6.3. Synthesis of <b>1-6</b> .....	128
6.4. ORTEP and packing diagrams of compound <b>1</b> .....	129
6.5. Fluorescence spectra of compound <b>1</b> .....	132
6.6. Structure of sensors <b>1</b> and <b>2</b> .....	135
6.7. Packing diagrams for compound <b>2</b> .....	137
6.8. Packing diagrams for Compound <b>1</b> .....	138
6.9. UV-vis absorption spectra of <b>1</b> and <b>2</b> .....	139
6.10. Fluorescence emission changes in <b>1</b> .....	140

## LIST OF TABLES

Table	Page
3.1. Crystal data and structure refinement for $[\text{Fe}(\text{salpm})_2]\text{BF}_4 \cdot 0.5\text{EtOH}$ .....	47
3.2. Atomic displacement parameters of $[\text{Fe}(\text{salpm})_2]\text{BF}_4 \cdot 0.5\text{EtOH}$ .....	50
3.3. Summary of the treatment of disorder .....	58
3.4. Average coordination bond lengths for $[\text{Fe}(\text{salpm})_2]\text{BF}_4 \cdot 0.5\text{EtOH}$ .....	61
3.5. Difference between the average Fe-L bond lengths .....	65
4.1. Common warning signs for twinning [102] .....	75
5.1. Steric Paramters for bi- and tri-nuclear nickel(II) N-alkylsalicylaldimines .....	110
5.2. Geometric parameters of $\text{Ni}_3(\text{iprsal})_4(\text{NO}_3)_2$ .....	113
5.3. Ni···Ni distances (Å) for $\text{Ni}_3(\text{Rsal})_4(\text{NO}_3)_2$ .....	114
6.1. Selected geometric parameter for compound <b>1</b> .....	125
6.2. Crystal data and refinement parameters .....	130
6.3. Association constants of compounds <b>1-6</b> with DCP .....	133

## 1. INTRODUCTION

Structure is one of the central concepts of chemistry. The amount of experimental explanation and predictive power that can be generated from knowing the atom connectivity and molecular conformation is undeniably great. Currently, the easiest way to determine molecular structure is by X-ray diffraction, wherein a day's time, the identity, solid state bondlengths, hydrogen-bonding and intermolecular interactions are all determined with one experiment. X-ray structures in conjunction with other measurements of reaction rates, electrochemical properties, magnetic interactions and many other properties provide a complete picture of the interesting chemical properties of a system. The following sections describe the application of X-ray crystallography and the insight gained from it to separate projects done independently, Section 5, or in collaboration with other researchers, Sections 3,4, and 6. Background of the theory and experimental practice of single-crystal X-ray diffraction is given in Section 2. A general background of elucidating electronic structure by magnetism measurements is given at the beginning of Section 5 as the direct comparison of molecular and electronic structure in applied in Sections 3 and 5.

Section 3 discusses the X-ray structural determination of  $[\text{Fe}(\text{salpm})_2]\text{BF}_4 \cdot 0.5\text{EtOH}$  at four different temperatures and how the X-ray results alone indicate characteristics of a two-step Spin CrossOver (SCO) phenomenon. The primary application for SCO materials in recent years has been towards information storage. On the molecular level this requires the stability of two different states and easy conversion between the two. Spin crossover materials exist such that the high-spin (HS) and low-

spin (LS) interconversion can be manipulated by perturbations such as heat, pressure and light. Multi-step LS-HS conversions are typically attributed to more than one unique site for the metal ions[1] such that the intermolecular interactions are different for each site. The structural reorganization of the coordination sphere during SCO can be significant especially in the case of Fe(II) which converts from a LS diamagnetic form to a HS paramagnetic form. For Fe(III) and other SCO compounds, the coordination bondlengths and angles also change significantly. Intermolecular interactions affect how the SCO even is propagated between metal centers throughout a material and is termed cooperativity. It is known that the presence of solvent molecules and nature of counterions also affect the characteristics of the SCO even though they do not directly interact with the SCO site. Each of these attributes must be considered in the analysis of a SCO event and since both the intra- and inter-molecular structures give critical information, rarely is an analysis done which does not involve the X-ray crystal structure.

Iron(III) complexes with Schiff base ligands are the most extensively studied Fe(III) SCO compounds [2] and their magnetic behavior can be tuned by a variety of chemical modifications. This versatility may generate even wider applications than other, more limited SCO compounds. This is why we are interested in expanding the study of Fe(III) complexed with N-(pyridin-2-ylmethyl)-salicylideneamine (Hsalpm). The perchlorate complex,  $[\text{Fe}(\text{salpm})_2]\text{ClO}_4 \cdot 0.5\text{EtOH}$ , has recently been shown to undergo a two-step thermal SCO transition [3]. The  $\text{BF}_4^-$  analog was synthesized and studied by crystallography because it produced suitable crystals. However, the magnetic susceptibility is yet undetermined, nothing is known about the complex, but is proposed to have interesting SCO properties. The X-ray crystal structure was determined

for  $[\text{Fe}(\text{salpm})_2]\text{BF}_4 \cdot 0.5\text{EtOH}$  in this case, not only measure cooperativity throughout the sample, but also predict the magnetic transition temperatures and HS/LS populations.

The results indicate a two-step transition occurring in the temperature ranges of 100-175 K and 175-225 K, higher temperatures than the perchlorate analog, and also that the 100-175 K transition is incomplete as residual HS iron sites remain down to 100 K. The SCO behavior is now known, thus elucidating the electronic structure and allowing us to predict the magnetic properties.

Section 4 contains examples of interesting practical problems both solved by the application of X-ray diffraction and encountered in structural determination by X-ray diffraction. The first problem concerned the absolute structure of a 1,10-phenanthroline compound projected for the use in medicinal chemistry applications [4]. Since biological interactions are strongly dependent on the absolute stereochemistry of molecules, it is of great importance to separate and unequivocally identify the absolute configuration. In this case the circular dichroic measurements were ambiguous, but the compound crystallized easily. The researcher sought out X-ray crystallography to help with the determination. Unfortunately, X-ray crystallography is also stereochemically ambiguous unless there is the presence of strong anomalous scattering of the X-rays. Anomalous scattering is very small for light atoms but large for heavy ones. Thus, once the heavy atom is present, the configuration can be determined with a high level of confidence. It was suggested that the researcher coordinate the phenanthroline to a metal ion for absolute structure determination. Consequently, the X-ray structure of the phenanthroline complex with copper(II) provided the exact stereochemistry later supported by LCMS.

Two other problems frequently encountered in X-ray crystallography are twinning and symmetry ambiguity. When not recognized and handled correctly, these issues lead to incorrect unit cell dimensions, and structural distances which are compared and used extensively in conjunction with other experimental data[1, 5, 6]. The task of critically analyzing the data for systematic absence violations, incorrect weighting schemes and symmetry relationships are illustrated in the structures of a hydrazinecarbothioamide nickel complex and a copper hydrazone complex  $\text{Cu}(\text{C}_{26}\text{H}_{20}\text{N}_6\text{O}_4)_2$ .

Section 5 describes the study of nickel(II) salicylaldimines with regards to their nuclearity, geometry and magnetic properties. Polynuclear complexes of paramagnetic atoms, such as nickel, have long been studied for their interesting magnetic properties. However synthesis of complexes of more than two metal atoms generally occurs arbitrarily according to the chosen reaction conditions and there is little predictability or selectivity as to the number of metal centers in the product. This can especially be the case for salicylaldimine-type ligands. For example, the reaction of  $\text{Ni}(\text{SCN})_2$  with salen ligands produces mononuclear and two different trinuclear products[7]. Even where the possible structural variability is lessened by a tetradentate ligand, many different products are formed. As in the reaction of  $\text{Ni}(\text{CH}_3\text{COO})_2 \cdot 4\text{H}_2\text{O}$  with 2-[(3-methylaminopropylimino)-methyl]-phenol which generates a co-crystal of bi- and trinuclear products[8]. Our interest resides in the generation of a unique trinuclear nickel complex,  $\text{Ni}_3(\text{Rsal})_4(\text{NO}_3)_2$ , in preference to a binuclear product,  $\text{Ni}_2(\text{Rsal})_2(\text{NO}_3)_2 \cdot \text{MeOH}$ , formed from the same reactants. Previously during the syntheses of the binuclears, the serendipitous formation of the trinuclear product was suggested to be dependent on the imine substituent, but was not completely investigated

[9]. Using variable reaction conditions we were able to selectively form the trinuclear product based on the coordination power of the solvent and also the mixing rate.

Understanding of the exchange coupling interactions between paramagnetic centers is important for generation of new materials, particularly in the realm of single molecular magnets (SMM). SMM require slow relaxation of the magnetization which is dependent on the total spin of the molecule and on its magnetic anisotropy [6]. If the energy barrier to the inversion of the magnetic moment is large enough to prevent a thermal jump or quantum tunneling, the material displays ideal characteristics for molecular based information storage [10]. In order to synthesize and rationalize molecules with large total spins, it is crucial to know the sign and strength of the exchange interactions within the molecule. In some systems both the sign and strength of the exchange interactions are dependent on the geometry of the superexchange pathways between the paramagnetic centers. As is the case with a known hexanuclear SMM of manganese, such that when the Mn-O-N-Mn angle is less than 30 the exchange constant is antiferromagnetic, and ferromagnetic when above 30[11]. Therefore important information can be gained by comparing the molecular structure from X-ray crystallography with the electronic structure derived from magnetic measurements.

In a previous study [12] of a trinuclear nickel complex with a structurally similar bridging core to  $\text{Ni}_3(\text{Rsal})_4(\text{NO}_3)_2$ , the magnetic susceptibility measurements were well fit to a scalene triangle with  $J_{12} = -32.7 \text{ cm}^{-1}$ ,  $J_{13} = +12.5 \text{ cm}^{-1}$ , and  $J_{23} = +25.0 \text{ cm}^{-1}$ . Even though, the fit was good and the geometry of the  $\text{Ni}_3$  triangle was truly scalene according to the crystal structure, the researchers were unable to determine an explanation for the observed signs of the couplings. Indeed, by inspection of the structure, the coupling



interactions are hard to definitively explain. However, if the coupling along each side of the triangle, a fragment containing only two nickels, could be rationalized to its molecular coordination mode, this would provide a starting point for the rationalization of three 2-nickel fragments that when combined form the triangular complex. As the nickel(II) salicylaldimines exhibit both the binuclear fragments and the trinuclear triangular complex, we have applied them in order to explain the confusing mixture of positive and negative couplings within such trinuclear systems. Our results indicate that the geometrical orthogonality of the salicylaldimine ligands to the bridging plane between each binuclear fragment is an important factor determining the presence of antiferromagnetic or ferromagnetic exchange within the fragment. The geometrical evidence of these trinuclears from X-ray structure determinations combined with the magnetic measurements provides a strong platform from which to explain magnetostructural parameters within larger hexanuclear nickel complexes capable of generating the large total spin required by SMM.

Section 6 reports the structural and spectroscopic studies of fluorescent turn-on sensors synthesized from a xanthene spirolactam construct used for the detection of metal ions and organophosphorus compounds. The environment is infused with contaminants from agricultural and industrial processes and detection of these substances is vitally important to ensure food safety, water quality and public health. Optical detection is easily recognized by untrained personnel and easily adapted for field use. An optical sensor that initializes upon interaction with a substrate rather than quenches, attracts more attention. It is important that sensors are selective and sensitive towards a particular substrate. Also a sensor that can produce different responses depending on the substrate

is also desirable. The xanthene spirocyclic compounds are a versatile group of compounds that exhibit the turn-on optical activity, are easy to modify and have excellent optical properties such as high quantum yield, good stability and long emission wavelengths.

By modifying the inamine substituent of the spirolactam ring of fluorescein and rhodamine with pentacyclic furan substituents, we were able to selectively and sensitively detect the heavy metal contaminant,  $\text{Cr}^{3+}$ , the nerve gas mimic, dichlorophosphate, and transition metals,  $\text{Ni}^{2+}$ ,  $\text{Fe}^{3+}$  and  $\text{Co}^{2+}$ . X-ray crystallography was used to determine the possible binding pockets available to the substrates. Results indicate that interaction of the substrate with the carbonyl of the colorless spirocycle causes an electron delocalization and breaking the N-C bond of the spirolactam ring, generating an intense color. The compounds exhibit  $\mu\text{M}$  sensitivity and excellent selectivity which combined with the other properties already mentioned, are promising detectors for environmental and biological applications.

## 2. SINGLE CRYSTAL X-RAY DIFFRACTION

### 2.1. THEORY

Theories of light, statistics, space and diffraction all play a role in structure determination by diffraction methods. Diffraction of x-rays has expanded greatly into separate techniques with specific methods and theories. While some of the theory applies to other techniques, the explanations put forth will predominantly remain in the context of small molecule X-ray crystallography.

**2.1.1. Advent of X-rays.** In 1895, Röntgen experimented and described a new form of electromagnetic radiation encompassing the wavelength range from  $10^{-8}$ - $10^{-10}$  m, which became known as X-rays [13]. The energy of this radiation lent itself to a whole, new gamut of applications. In fact, the benefits of its use for biological imaging were immediately recognized when Röntgen produced an image of the bones in his wife's hand. The exploration of the properties and applications of X-rays proceeded rapidly through the turn of the century. The first X-ray absorbance spectroscopy measurements were conducted by de Broglie in 1913 to show the absorption K-edges of Ag and Br [14, 15]. Scattering of X-rays gives information concerning the shape and size of macromolecules, and took off later in the 1930s and developed into the modern technique known as small angle X-ray scattering (SAXS). An extension of the scattering behavior of light is diffraction, where light passing edges or narrow slits produce fringes of parallel light and dark bands. The diffraction of X-rays was initially studied by von Laue with experiments showing distinct patterns on film [13]. Quickly, by 1913, x-ray diffraction of 3D arrays by Bragg expanded our understanding of molecular structure [16] by

experimentally showing that solid NaCl was not made of individual molecules but was an extended array of sodium and chloride ions. In 1929 Kathleen Lonsdale showed benzene to have 6 equidistant bonds using X-ray diffraction [17]. By 1954 Dorothy Hodgkin had determined the molecular structure of vitamin B<sub>12</sub> [18] and myoglobin, the first protein of ~150 amino acids was determined by Max Perutz and Sir John Cowdery Kendrew [19]. Large increases in computational power and speed in the latter half of the nineteenth century allowed small molecule structures to be solved routinely.

The process from diffraction pattern to molecular structure is complicated and even though computers take away the need for in depth understanding of all the steps, lack of basic understanding of the process leads to many unsolved structures, poor quality determinations and actual errors. A firm grasp of the theory of X-ray crystallography should begin with an understanding of diffraction, specifically diffraction through crystals.

**2.1.2. Diffraction.** Light from a point source spreads out in all directions. When this light passes an object the light scatters and spreads into the area that would have been blocked by the object. This phenomenon is known as diffraction. Diffraction is usually explained using Huygens's principle that every point on a wave front can be considered as a point source of tiny wavelets that spread out in the forward direction at the speed of the wave itself [20]. Therefore, when passing an object, radiation will bend and then produce an image or pattern on a screen. This diffraction pattern can be seen to have darker and lighter sections spread out in a particular arrangement. These intensity differences are due to the constructive and destructive interference caused by the phase relationship of the wavelets generated at the object. The intensity also depends on the

scattering angle of the resultant wavelets. The angular spread of the pattern depends on the ratio of the wavelength ( $\lambda$ ) of the radiation used to the minimum dimension ( $x$ ) of the object causing the scattering. The larger the value of  $\lambda/x$ , the larger the angular spread of the diffraction pattern [16].

The interference of waves resulting in the diffraction pattern is usually described in context of Young's 1801 double slit experiment (Figure 2.1) where monochromatic

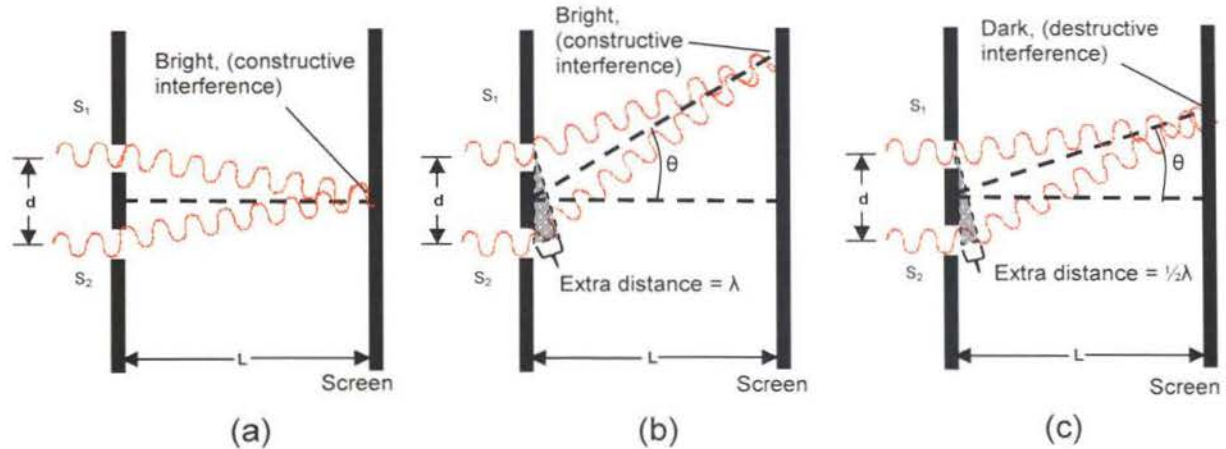


**Figure 2.1.** Interference of radiation from two slits at different scattering angles,  $\theta$  [20].

radiation passing through the slits and diffracting at different angles is shown. In Figure 2.1a, both waves arrive at the screen in phase and thus their amplitudes are added, constructive interference. When the diffraction angle ( $\theta$ ) of the waves increases, the distance of travel to the screen is larger for one wave than the other. When the extra distance traveled by one wave is equal to  $n\lambda$  ( $n=1, 2, 3\dots$ ), the phases of the waves coincide and again produce constructive interference. However, if  $\theta$  is such that the extra

distance of travel for one wave is  $1/2\lambda$ , both waves arrive at the screen completely out of phase and the dark line from destructive interference is present (Figure 2.1c). At intermediate angles where the phase difference is between 0 and  $1/2$ , neither complete constructive nor destructive interference occurs so intermediate intensities will be seen on the screen. Because diffraction is occurring at both slits, the combination of interference between waves from the same slit and waves scattering at the same angle from the other slit determines the intensity of the diffraction. The distance between the slits relates which regions of the screen are illuminated. Narrow spacing between the slits produces wide illuminated regions, while wide spacing produces narrow illuminated regions, a reciprocal relationship. Adding more slits of equal spacing narrows the areas of complete constructive illumination such that the diffraction pattern only shows sharp lines.

Combining a 1D grating with a given spacing of slits with another 1D grating with a different spacing of slits will yield a 2D diffraction pattern showing reciprocal spacings that are perpendicular to their original orientation [16]. This is the fundamental correlation between distances and orientation in real space, where the actual slits (or atoms) exist, and distances in reciprocal space, where the diffraction pattern exists.

One hundred years ago in 1912, Max von Laue, along with Friedrich and Knipping discovered the diffraction of X-rays through crystals, thus receiving the Nobel Prize only two years later [21]. Laue explained the conditions for diffraction from 3D arrays in terms of the reciprocal lattice. In 1915, W.H Bragg and W. L. Bragg shared the Nobel Prize for their contributions to crystallography. The Braggs described the conditions for diffraction, not in terms of the reciprocal lattice as von Laue had done, but in real space [22]. If one imagines planes to extend between the points of a crystal

lattice, then the diffracted beam can be thought of as “reflecting” off these planes so that the angle of incidence is equal to the angle of reflection. Constructive interference will occur when waves scatter from adjacent parallel planes such that their path difference is an integral multiple of the wavelength of the radiation. This relationship bears out in the equation  $n\lambda = 2d \sin \theta$ , where  $d$  is the perpendicular distance between adjacent planes,  $\theta$  is the complement of the angle of scatter,  $n$  is an integer and  $\lambda$  is the wavelength of the radiation used (Figure 2.2). The angle between the radiation and the incident beam is  $2\theta$ , also known as the scattering angle.

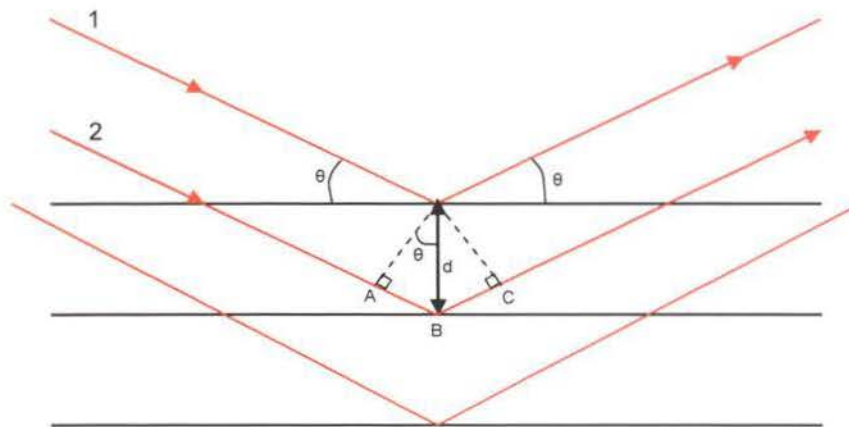


**Figure 2.2.** Reflection of waves from planes of atoms. When two waves, 1 and 2, of equal phase enter a crystal, they will constructively interfere upon exit if their path difference satisfies the equation  $n\lambda = 2d \sin \theta$ .  $AB + BC = 2d \sin \theta$ .

**2.1.3. Intensities.** As when adding adjacent slits sharpens the lines of diffraction maxima in one dimension, and combining two 1D gratings sharpens the diffraction maxima in two dimensions to produce circles, having many uniformly stacked, adjacent gratings in three dimensions produces sharply defined spheres in reciprocal space. These

spheres are often called “reflections” of the X-rays and exhibit particular intensities and positions. As in the case where the location of constructive interference depended on the distance between slits, the angular position of a reflection depends on the dimensions of the repeating lattice, the unit cell. The intensities of each diffraction sphere, on the other hand, are almost solely based on the types of scatterers (atoms) and their arrangement (structure) within the unit cell [4 p 63].

As the electromagnetic radiation interacts with each individual electron, the waves coherently scattered from the electrons of one atom and in the direction of the beam ( $2\theta=0$ ), scatter in phase and the sum of their amplitudes provides the intensity of the diffraction for that atom. The scattering from all the electrons of one atom is known as the atomic scattering factor,  $f$ , and is proportional to the atomic number of the atom, or more precisely the number of electrons retained by the atom. The scattering from each electron at different angles combine with slightly different phases and partially, destructively interfere causing the decrease in the scattering factor amplitude (intensity) with increasing angle,  $2\theta$ . When waves diffract from electrons in an atom, the magnitude of the phase difference will, proportionally, cause greater interference if the radiation is of a shorter wavelength [23 p144] Therefore, it is common to see the atomic scattering factors of elements graphed relative to the diffraction angle and wavelength,  $\sin \theta/\lambda$  (Figure 2.3).



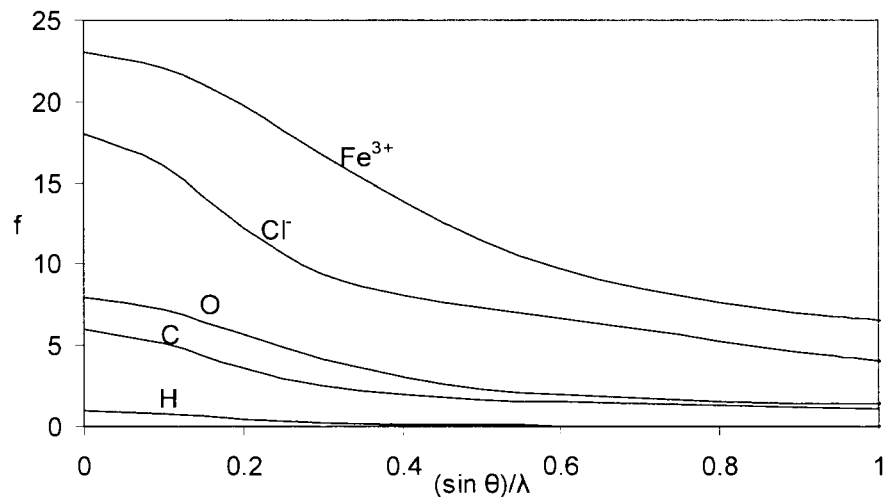


**Figure 2.3.** Atomic scattering factors,  $f$ , for atoms or ions vs.  $\sin \theta/\lambda$ . The scattering factor of an atom is equal to ratio of the amplitude of a wave scattered by the atom to that of a wave scatter by a single electron [24].

Atomic scattering factors provide a measure of the scattering by each individual atom and it would make sense that the scattering associated with an entire structure/unit cell could be approximated by summing the independent scattering contributions of the constituent atoms [4, p 69]. This must be done keeping in mind that scattered waves have both amplitude and phase. A wave scattering from an atom,  $j$ , can be expressed in complex notation as

$$F_j = f_j(\cos \alpha_j + i \sin \alpha_j) \quad (2.1)$$

where  $f_j$  is the amplitude or atomic scattering factor and  $\alpha_j$  is the phase. As stated previously, when adding the scattering from different electrons, or in this case, atoms, there will be a difference in phase. This phase difference depends on the fractional coordinates  $(x,y,z)$  of the atom in the unit cell and the indices of the reflection  $(h,k,l)$  being considered which is expressed in the equation,

$$\alpha = 2\pi(hx + ky + lz) \quad (2.2)$$

Combining equations 1 and 2 and summing over all atoms in the unit cell will give

$$F_{hkl} = \sum_j f_j [\cos 2\pi(hx_j + ky_j + lz_j) + i \sin 2\pi(hx_j + ky_j + lz_j)] \quad (2.3)$$

where  $F_{hkl}$  is called the structure factor, whose amplitude squared is proportional to the intensity of the diffracted beam (equation 2.4). It is important to keep in mind that every

$$|F_{hkl}|^2 \propto I_{hkl} \quad (2.4)$$

atom in the unit cell contributes to every structure factor,  $F_{hkl}$ , according to its position in the cell and its identity[25]. Each diffracted “reflection” is described mathematically by a structure factor equation describing the original diffracted wave of light from the crystal lattice.

**2.1.4. The Phase Problem.** The goal of the crystallography experiment is to determine the positions of the atoms,  $x, y, z$  within the unit cell. The equation for the structure factor (equation 2.3) provides the relationship to calculate  $x, y, z$  for any reflection of a certain  $h, k, l$  value. However, the structure factor contains both a magnitude and a phase. Unfortunately, from the diffraction of X-rays we are able to measure directly only intensity, which allows us to figure out the amplitude from equation 4 but not the sign (+ or -) of the structure factor,  $F_{hkl}$ . The phase information of the wave needed to solve the structure factor equation is lost. This is commonly referred to as the “phase problem” of crystallography.

But, theoretically, if we did have the phases, calculation of the atomic positions can be conducted by the standard mathematical method of a Fourier transform. The Fourier theorem states that any function of a single-valued continuous variable can be

expanded as a series of sines [26]. This mathematical manipulation relates the structure factor equation (equation 2.3) with the following equation for electron density,

$$\rho_{x,y,z} = \frac{1}{V} \sum_{hkl} F_{hkl} \exp[-i2\pi(hx + ky + lz)] \quad (2.5)$$

where  $\rho_{x,y,z}$  is the electron density at any place (x,y,z) in the unit cell, V is the volume of the unit cell. Note the summation is over all values of h, k, and l. Equation 5 essentially gives a 3D map of the amount of electron density per unit volume. By placing atoms at the locations of the highest electron density, the structure of the unit cell contents can be geometrically constructed.

#### 2.1.4.1. Patterson.

Again, how do we get the phases of the diffracted waves? The phase problem has been tackled many different ways, but initially, most successfully by A. Patterson in 1935 and became the predominate method used from the 1930s to 60s. The Patterson function,  $P(u,v,w)$ , consists of a Fourier series that depends only on the indices, (h,k,l) and the  $|F|^2$  values for the diffracted beam are used (equation 2.6) [4

$$P(u, v, w) = \frac{1}{V} \sum_{all\ hkl} |F|^2 \cos 2\pi(hu + kv + lw) \quad (2.6)$$

p114].  $u,v,w$  is another coordinate system often referred to as Patterson space or a Patterson vector map that is the size and shape of a unit cell. The map relates electron density. When two atoms in the unit cell are separated by vector (u,v,w), then there will be a peak in the Patterson map at (u,v,w). Every peak in the Patterson map will correspond in orientation and length with a vector between two atoms. The peak heights of these vectors are proportional to the product of the atomic numbers of the atoms at the ends of the vectors. The origin of these vectors, however, can be anywhere. This makes interpretation of a Patterson map extremely complicated unless there is perhaps a peak of

unusual height at  $u, v, w$  which would correspond to many pairs of atoms relating to that vector or perhaps atoms with high atomic numbers. The largest peaks will give the relative positions of the heaviest atom and thus will provide a good starting point (trial structure) for determination of the other atoms either by further inspection of the Patterson map or with other Fourier methods [23 p159]. In essence the Patterson method solved the phase problem by performing a Fourier synthesis of the structure factor equation without the phases.

**2.1.4.2. Direct methods.** With the advent of fast computers in the late 1960s, a statistical approach, known as direct methods, for determining the phases of the reflections overcame the Patterson technique. Using the supposition that electron density must be nonnegative throughout the unit cell and must contain approximately spherical peaks (atoms), there are limits to the possible phase angles for individual reflections. Then relationships are used, like the Sayre probability relationship that states for three reflections, in a centrosymmetric structure, the sign of one phase is likely to be the product of the signs of the other two phases. The three reflections are related such that  $h, k, l$  and  $h', k', l'$  are related to  $h'', k'', l''$  by their difference,  $h'' = h' - h''$ ,  $k'' = k' - k''$  and  $l'' = l' - l''$  [4, p112]. Also using normalized structure factors,  $E$ , structure factors assuming atoms have no thermal motion and determined directly from diffraction data, a distribution of  $E$ -values can be generated, (equation 2.7) where  $\langle |F|^2 \rangle$  is the average

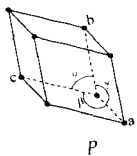
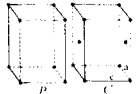
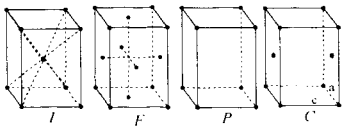
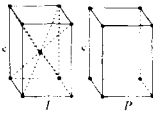
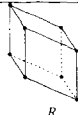
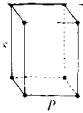
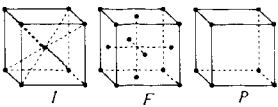
$$E^2 = |F|^2 / \langle |F|^2 \rangle \quad (2.7)$$

structure factor magnitude in a shell of  $(\sin \theta)/\lambda$ . This  $E$ -value distribution is dependent on the presence or absence of a center of symmetry and is used to estimate the quality of the data [26] such that if the average  $|E^2 - 1|$  value is close to 0.736 the structure is

noncentrosymmetric and if closer to 0.968, the structure is centrosymmetric. Also other methods are used to predict and optimize the phases of the strongest reflections to generate E-maps, from which the atomic positions can be determined [23, p160].

**2.1.5. Symmetry.** So far, through the fundamentals of diffraction, we have described how the types and positions of atoms within the unit cell affect the intensities and phases of the diffracted radiation. Followed by a summary of how those measured intensities and estimated phases are used to generate a 3D map of the structure. However, there is one other property of crystals in real space that drastically affects the diffracted pattern in reciprocal space, the symmetry of the crystal. So, in order to understand the affects, a basic knowledge of symmetry and crystals and how they are described is required.

**2.1.5.1. Lattice types and the unit cell.** A crystal is defined as any homogeneous solid with long-range three-dimensional internal order [26]. The smallest basic structural pattern outlined by an imaginary parallelepiped, that translated in three dimensions forms the entire crystal lattice, is known as the unit cell. It has edge lengths of  $a$ ,  $b$ ,  $c$  and angles  $\alpha$ ,  $\beta$ ,  $\gamma$  as shown in Figure 2.4. More than one choice of parallelepiped is available for most crystals, the unit cell chosen is the one that best represents both the translational and rotational symmetry of the entire crystal in addition to having the smallest possible lengths and angles closest to  $90^\circ$ . The unit cell shapes fall into 7 categories called crystal systems, depending on their rotational symmetry (Figure 2.4). Then in the mid-1800s, Frankenheimer and Bravais systematically determined that centering the unit cells such that an additional lattice point is in the body center, face centers, or edge-centers of the unit cell, the unit cell may contain more of the symmetry

Crystal System	Restrictions on axes and angles	Bravais Lattice
Triclinic	None	
Monoclinic	$\alpha = \gamma = 90^\circ$	
Orthorhombic	$\alpha = \beta = \gamma = 90^\circ$	
Tetragonal	$a = b$ $\alpha = \beta = \gamma = 90^\circ$	
Trigonal	$a = b = c$ $\alpha = \beta = \gamma$ or $a = b$ $\alpha = \beta = 90^\circ$ $\gamma = 120^\circ$	
Hexagonal	$a = b$ $\alpha = \beta = 90^\circ$ $\gamma = 120^\circ$	
Cubic	$a = b = c$ $\alpha = \beta = \gamma = 90^\circ$	

**Figure 2.4.** Bravais lattices. Unit cell representation, crystal systems and lattice centering also shown with symbols [24].

of the crystal compared to the primitive (one lattice point) unit cell. Combination of four lattice types and the seven crystal systems yields the 14 Bravais lattices shown with their symbols in Figure 2.4 . It is important to note that the lattice coordinate system is only a series of imaginary points used to describe the symmetry of the structure of the atoms molecules etc. that form the crystal. When these 14 lattices are combined with translational symmetry elements (discussed next), it was found that there is only 230

possible arrangements in which to pack atoms in the regularly repeating patterns found in crystalline solids. These are known as the 230 crystallographic space groups and are tabulated in the International Tables of Crystallography.

**2.1.5.2. Point and space groups.** The concept of symmetry is obvious to many people. If an object can be rotated, reflected or turned inside out without changing any distinguishable characteristics, it possesses symmetry. The axis around which it is rotated, the plane in which an object is reflected and the center point in which the object is inverted (turned inside out) are known as symmetry elements. The action about the symmetry element is called the symmetry operation. For example, the operations of rotation, reflection, inversion are all point-symmetry operations since each leaves a point within the object stationary. Rotation axes are designated by an integer,  $n$ , such that when the object is rotated  $360^\circ/n$ , it is unchanged from its starting position. While an object or molecule may have a local, rotation axis of 5, 7, or 8, it has been proven that only rotation axes of 1,2,3,4 and 6 are possible for structures built on 3D lattices [4, p92]. Roto-inversion axes are designated by  $\bar{n}$ , where again the structure is rotated by  $360^\circ/n$ , but is then inverted through a point on the axes to produce the original object. Mirror planes,  $m$ , are reflections through a plane, but are equivalent to a two-fold roto-inversion axis,  $\bar{2}$ , oriented perpendicular to the plane. A mirror plane will convert right hands into left hands, hence change the chirality of a molecule. Of the total number of ways to combine the rotation axes, 1,2,3,4,6 and the roto-inversion axes,  $\bar{1}$ ,  $\bar{2}$ ,  $\bar{3}$ ,  $\bar{4}$ ,  $\bar{6}$ , there are only 32 three-dimensional combinations known as the crystallographic point groups.

Since interest not only lies in the symmetry of the structure, but also how it is related to the structures nearby, space symmetry must be considered. By definition, the

unit cell is stacked side by side in all three dimensions. This provides not only simple movement (pure translation) of the entire unit cell along one dimension, but it can also produce other space-symmetry operations like screw axes and glide planes. A screw axis,  $n_r$ , is the combination of a rotation of  $360^\circ/n$  and a translation parallel to the axis by the fraction  $r/n$  of the period along that axis. For example a 3-fold screw axis,  $3_1$ , along the axis  $b$ , would first rotate the structure by  $120^\circ$  and then translate  $1/3$  of the unit cell length along axis  $b$ . Glide planes are the result of a mirror operation and a translation. Since mirrors are two-fold, a glide plane will cause a translation of halfway along the unit cell edge and depending on the parallel axis, can be an a-glide, b-glide or c-glide [4, p96]. Combining the 32 crystallographic point groups and these space-symmetry operations yields 230 different possible ways of packing objects in three dimensions such that the contents of the unit cell are arranged exactly the same throughout the solid; the 230 space groups.

**2.1.5.3. Systematic absences.** Translational symmetry (lattice centering, screw axes, glide planes) in real space has important implications when it comes to the diffraction pattern produced in reciprocal space. In fact, these translational elements cause certain reflections, that ordinarily satisfy the diffraction condition ( $n\lambda = 2d\sin\theta$ ) to be absent. This is caused by the translation symmetry element producing a plane of atoms where there would not be one in the absence of translational symmetry. This new plane of atoms of exactly the same electron density, therefore same structure factor amplitude, will cause complete destructive interference for specific sets of planes. As an example, for any plane,  $h,k,l$  in a C-centered lattice, any reflection where  $h+k=2n+1$  will not be observed in the diffraction pattern. These systematic absences help to classify the



diffraction pattern to space groups that exhibit the specific combination of translational symmetry elements [26].

**2.1.5.4. Symmetry in both spaces.** The symmetry relation between real and reciprocal space allows for certain similarities and differences. Certain symmetry in real space, like four-fold rotation and mirrors, will transfer as a four-fold and mirror symmetry in reciprocal space. However, diffraction patterns are always centrosymmetric and translational symmetry in real space does not cause any translational symmetry in reciprocal space. The symmetry of the diffraction pattern in reciprocal space is usually classified into one of the eleven Laue point groups[25] in order to determine which part of the diffraction data is unique and which is redundant [26].

**2.1.6. Summary.** X-ray radiation is ideal for exploring the structure of molecules due to its wavelength being a comparable size to the distances between atoms such that regularly repeating arrays of atoms diffract the X-rays into distinct patterns. The spacing of the reflections within the diffraction pattern provide a measure of the unit cell lengths and angles taking into account that any distance,  $d$  in real space is  $1/d$  in reciprocal space. Identification of the space group of the crystal is valuable for identifying symmetrical parts of a molecule but also simplifies analysis of the diffraction pattern by identifying sections that are equivalent. So, in order to determine the space group, the symmetry of the diffraction pattern, the Laue point group is determined. Then, statistical analysis of normalized structure factors, specifically the  $|E^2-1|$  value, allows for good determination of the centrosymmetry of the crystal. From the reflections found to be systematically absent, the lattice type as well as translational symmetry is ascertained which usually constrains the possible space groups to a very short list. The diffraction

pattern is again analyzed where the measured intensities of the reflections give information regarding the electron density present in each crystal plane that satisfies the diffraction condition, ( $n\lambda = 2d\sin\theta$ ). Combined with the probable space group and intensities, estimated phases are determined, and produce an electron density map showing atom positions in real space.

## 2.2. PRACTICE

Relating theory and practice finds the researcher with an ever-changing toolbox. While regretful for some and to the delight of others, the tools of one era are exchanged for the tools of another. Today, the mathematical understanding and manual precision have been replaced by software manipulation skills and data analysis understanding. X-ray crystallography is no exception; however, the process from diffraction pattern to complete structure solution, still requires an understanding of more than one theory and the practical skills to connect them. Without this, meaningful solutions and their interpretation is impossible for all but simple, well-behaved samples.

**2.2.1. Sample.** Every characterization technique has limits to the type, size, stability and other physical properties of the samples conducive to generate meaningful data. For crystallography, it is the very specific, regularly repeating, solid form present in single crystals. The crystal chosen for measurement needs to be of the correct size. The size can vary from 0.01mm for a micro-focus X-ray source to 0.8mm for a tube source, depending on the diameter of the X-ray beam. It is important that the crystal remain entirely within the beam during the entire collection period so as to ensure accurate corrections for absorption.

Perfect single crystals are free of dislocations, point defects, cracks and impurities. However, real crystals will almost always have some of these conditions, but they typically occur in growth boundary regions between the nice, regular domains which can be tilted from each other from  $1^{\circ}$ - $1^{\circ}$  [26 p A0-3]. The domain structure of crystals, mosaic structure, requires that real crystals be rotated so that each domain has an opportunity to satisfy the diffraction condition and thus contribute to the intensity of the reflection. Single crystals also typically exhibit birefringence so exhibit sharp extinction when rotated between polarizers on a microscope. When only part of the crystal is extinguished, it is often a sign of twinning. Perhaps the most important thing to keep in mind when choosing a crystal for measurement, is the crystal habit, or shape. The crystal needs to be representative of the sample from which it is taken. Was the sample homogeneous? A sample containing platelets, needle and block crystals all in the same sample most likely consists of a mixture of compounds, impurities or polymorphs.

Sample stability is of paramount importance. Even today, most X-ray diffraction experiments require samples to remain in the beam for hours or even days. Crystals that are volatile or contain volatile components, such as solvent, often dry out under ambient conditions. Some sample crystals sublime or melt at higher temperatures and some react with water or oxygen in the air. The current and common method of controlling these situations is to cool the sample during measurement using liquid nitrogen. Not only does the low temperature and nitrogen atmosphere allow the sample to remain stable, but the temperature also decreases the molecular movement of atoms, producing better diffraction patterns.

Both the quality and the size of crystals depend on the complicated process of crystal growth. Growing crystals from solution usually requires a balance of factors to slowly lower the saturation point and control the rate of nucleation so that only a few large crystals form [4 p 9]. There are many methods, and variations of them, generally employed to grow single crystals such as solvent evaporation, slow cooling, solvent diffusion and sublimation. Growth of the best crystals occurs over long periods of time, and by controlling factors such as temperature, pH and ionic strength such that the regular arrangement of molecules can form.

**2.2.2. Diffractometer.** Like most radiation techniques, the hardware components necessary to conduct the experiment fall to a source, a sample and a detector. For a source, a monochromatic beam of light is desired for diffraction experiments and is typically produced by directing a high energy electron beam towards a metal target, usually Mo, Cu or Ag. The electrons interact with the electrons of the target and at a certain voltage, are able to ionize an inner core electron. Subsequent filling of the inner hole by an outer electron releases energy of a characteristic X-ray wavelength. When the electron transitions from the L-shell to the hole in the K-shell, it is designated a  $K_{\alpha}$  transition. Relaxation from the M-shell to the K-shell would yield a  $K_{\beta}$  x-ray emission. Other X-rays of significantly lower intensity, white radiation, are also emitted due to incomplete energy transfer between the high energy electron and the electrons of the metal. Both the  $K_{\beta}$  wavelength and much of the white radiation are removed by a filter or a monochromator. The  $K_{\alpha}$  radiation that encounters the sample is actually an average of two different energy transitions from the s and p subshells from the L shell, which are too close in energy to easily be separated. For example the Mo  $K_{\alpha 1}$  emits at a wavelength of

0.70926 Å and the Mo  $K_{\alpha 2}$  emits at 0.71354 Å and is therefore typically referenced experimentally as 0.71069 Å [26 p V-9].

The crystal sample is usually delicately placed on the end of a glass fiber with an amorphous, therefore non-diffracting, medium of glue, epoxy or oil. The glass fiber is mounted onto a goniometer which allows for precision rotation of the crystal in the orientation necessary to get a complete diffraction set of data. The center of the goniometer is the desired location of the crystal sample and where the X-rays are targeted from the source. Figure 2.5 shows the Eulerian geometry goniometer with four degrees of freedom;  $\varphi$ ,  $\omega$ ,  $\chi$ , and  $2\theta$ , centered on the Cartesian coordinate system of the laboratory,  $X_1$ ,  $Y_1$ ,  $Z_1$ . Angles  $\omega$  and  $2\theta$  are always remain cocentric around the  $Z_1$  axis and the detector is typically mounted on the  $2\theta$  arm so that position of the detector is directly equal the  $2\theta$  value for a diffracted reflection [16 p46]. The  $X_1$  axis follows the source radiation and with the  $Y_1$  axis and crystal form the goniometer equatorial plane [27 p280].

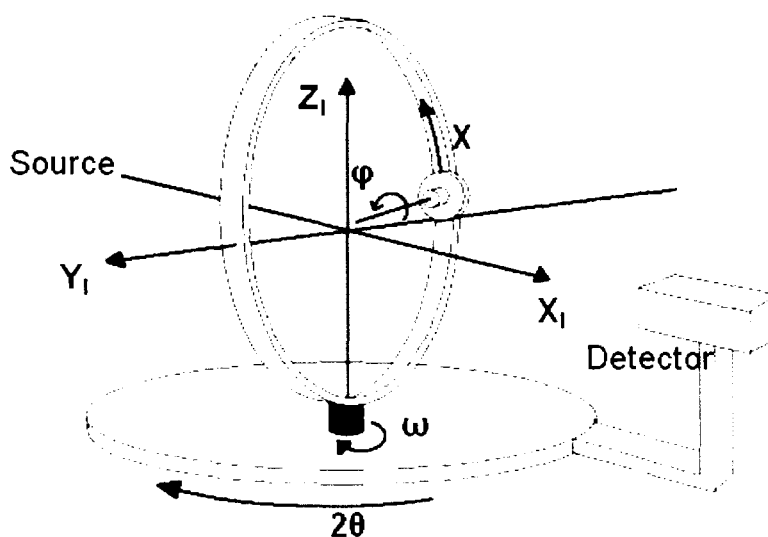


**Figure 2.5.** Eulerian geometry goniometer. Four rotational degrees of freedom and the laboratory coordinate axes are shown[26].

Detectors have seen much advancement from the original film methods, to image plates and scintillation counters, to the CCD detectors used today on most instruments. CCD detectors combine the automation benefits of scintillation counters with the advantage of measuring multiple reflections in one 2D image. The X-rays first hit the detector and excite a phosphorescent screen which emits visible photons that are coupled to a CCD chip through fiber optics. The CCD chip converts the electrical charge in each pixel into a number which is then stored digitally [26 p A3-9]. Another major advantage of the automated CCD detector is that the crystal axes need not be aligned with the diffractometer's axes, as was the case with older detectors [27 p 286]. The two-dimensional image that also contains the quantitative data, for a given set of angles is called a frame. Hundreds of frames with thousands of reflections are typically taken for one structure determination, so the dynamic range, spatial resolution and speed of the detector are very important.

**2.2.3. Experimental Process.** Obtaining the diffraction pattern and determining the structure in the lab provides chronological application of the theories involved, but also adds more practical considerations. The following will describe the general process, additional considerations for each step and specification of the software programs used in this research to carry out the process. Figure 2.6 outlines the general process.

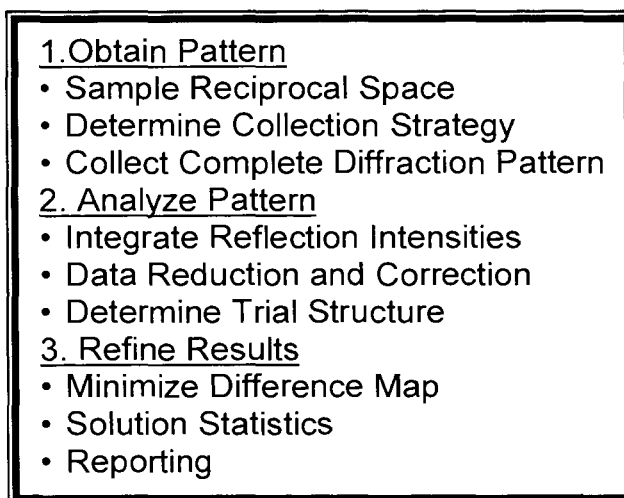


**Figure 2.6.** Experimental steps of crystal structure determination.

**2.2.3.1. Obtaining the diffraction pattern.** The first measurements typically taken are a sampling of reciprocal space. Once the crystal is centered on the diffractometer, three series of ~20 diffraction frames each are taken by the host software. It is important that the series are orthogonal and overlap in order to get a representative sample of reciprocal space because the unit cell dimensions and lattice type are determined from these frames.

To begin, high intensity reflections are chosen, such that the intensity,  $I$ , is greater than three times the intensity standard deviation,  $\sigma$ . The geometric positions of the reflections are used to determine the lengths and directions of reciprocal lattice vectors, defined in Cartesian lab frame. The three shortest, non-coplanar reciprocal lattice vectors would give the reciprocal unit cell vectors,  $a^*$ ,  $b^*$ ,  $c^*$  [26 p XII-2]. Then a series of geometrical and matrix manipulations typically done by computers is used to calculate

the orientation matrix. The orientation matrix converts the reciprocal lattice vectors expressed in Cartesian lab space coordinates ( $X_1, Y_1, Z_1$ ) to reciprocal lattice vectors expressed in reciprocal space dimensions ( $a^*, b^*, c^*$ ). Using this information, it is possible to index the reflections. Indexing is the process of identifying the order,  $n$ , of the reflection that satisfies  $n\lambda = 2d\sin\theta$  in all three dimensions, thus giving values for  $h, k, l$ . The  $h, k, l$  values of a reflection designate the position of the reflection relative to the origin of the reciprocal lattice and, in real space, designates the family of crystal reflection planes. Accuracy of the orientation matrix is crucial as it determines the diffractometer angles and indices of the reflections. The process of refining the orientation matrix uses the basis that sets of three indexed, linearly independent reflections can each, alone, determine the orientation matrix and unit cell [27 p 296]. The added determinations and variations in the computed orientation matrix provide a more accurate value for the matrix and a measurement of the error.

If the unit cell chosen is indeed the primitive cell consisting of the shortest non-coplanar vectors of the reciprocal lattice (Niggli cell), it is unique such that it will mathematically transform into only one Bravais lattice type. Most of the time, the symmetry inherent of the Bravais lattice is the same as the metric symmetry of the contents of the unit cell. In cases like where a monoclinic unit cell has  $\beta$  very close to  $90^\circ$ , the reduced cell will predict an orthorhombic unit cell. Choice of the wrong unit cell at this point in the experiment can easily be missed if the intensities of the diffracted reflections are not considered using Friedel's law [27 p 309]. The law states that the intensity of the diffracted wave from one set of planes,  $[h, k, l]$  will be the same as the intensity of a reflection  $[\bar{h} \bar{k} \bar{l}]$  centro-symmetrically related. These intensity



relationships are demonstrated differently in each diffraction pattern depending of the lattice type. For example, a triclinic lattice will produce four, specific pairs of equivalent reflections;  $I_{hkl} = I_{\bar{h}\bar{k}l}$ ,  $I_{\bar{h}kl} = I_{h\bar{k}l}$ ,  $I_{h\bar{k}\bar{l}} = I_{\bar{h}kl}$ , and  $I_{hk\bar{l}} = I_{\bar{h}\bar{k}l}$ . Due to the two-fold axis present in the monoclinic point group  $2/m$ , two sets of four equivalent intensities would be found in the diffraction pattern;  $I_{hkl} = I_{\bar{h}\bar{k}l} = I_{h\bar{k}\bar{l}} = I_{\bar{h}kl}$  and  $I_{\bar{h}kl} = I_{h\bar{k}l} = I_{hk\bar{l}} = I_{\bar{h}\bar{k}l}$  [27 p 311]. The Laue symmetry of the diffraction pattern should never be of a higher order than the metric symmetry of the crystal.

Thus far, the orientation matrix, unit cell dimensions with errors, and the Bravais lattice have been determined using only the 3 orthogonal series of images. This information is now used to derive the instrumental conditions necessary for collection of the diffraction pattern. Factors of time, redundancy, resolution and completeness are all factored in the calculation of the collection strategy. The maximum resolution,  $d$ , or ability to discern peaks in the electron density map, for a crystal of high quality in which all the reflections can be collected is  $0.459\lambda$  [27 p 331] and is calculated from the equation,  $d = \lambda/2\sin(\theta_{\max})$  where  $d$  is approximately the distance between the peaks. For Mo radiation,  $d = 0.33\text{\AA}$  and can easily provide resolution at the atomic level were bonds are of the order of 1-3  $\text{\AA}$ . However, the reflections most important for high resolution are the reflections that occur at high diffraction angles. So, if the reflection data is limited to low angle reflections, i.e. for a poor quality crystal, the peaks in the density map may not be resolvable. The minimum resolution projected for the quality of crystal and the wavelength of the radiation is calculated from the small number of frames already measured. The minimum resolution generally acceptable for a structure is 0.84  $\text{\AA}$ .

Rather than crystal quality, it is the crystal symmetry that is used to determine the redundancy and completeness characteristics of the collected diffraction pattern. The more symmetric a crystal structure, typically the more symmetric the diffraction pattern and the more equivalent reflections will appear in a given area of reciprocal space. This, combined with Friedel's law, causes redundancy; the same reflection recorded from the same crystal orientation or different orientations. A certain amount, typically 4-5, of redundancy is required for better data correction and error determination. The completeness of a diffraction pattern is determined if all the possible reflections have been collected to determine the structure of the smallest portion of the structure not related by symmetry, called the asymmetric unit. If the Bravais lattice was determined to be of a higher symmetry, like orthorhombic, a smaller portion of reciprocal space is required to determine the structure than from a higher symmetry like monoclinic. A completeness of 100% is desired for all structures, but is acceptable above 99%.

The combination of the desired resolution, redundancy, and completeness all factor into the valuable commodity of time. Where in the past, structures took days to weeks to collect the diffraction images, now can be done in 6-12 hours for similar or better quality data. This is mostly due to hardware advancements, but time is still expensive. Collecting data to a higher resolution takes longer and may be a waste of time if there are no observable reflections at the high scattering angles. Higher redundancy improves the error and accuracy of the data, but requires more of reciprocal space to be sampled. The completeness of the structure is almost never compromised for time, and then, primarily only in instances where the sample is unstable. Weakly diffracting crystals may require exposure to X-rays for a longer period of time to increase their

intensity, and some crystals are susceptible to decomposition when exposed to X-rays. The collection strategy, determined from all these parameters, is the series of instrument angles and rotations necessary to sample the required portion of diffraction space and also which reflections will be measured first.

Actual data collection is straightforward, and the most important features are as follows. Area detectors use an oscillation method for collecting the frames. For any one frame of an  $\omega$ -scan, the angles  $2\theta$ ,  $\phi$ , and  $\chi$  are fixed while the crystal is rotated about  $0.5^\circ$  in  $\omega$ . Alternatively,  $2\theta$ ,  $\phi$ , and  $\omega$  are fixed while the crystal is rotated about  $\phi$  in a  $\phi$ -scan. This is due to the mosaic spread of real crystals ( $\sim 0.1$ - $0.2^\circ$ ) [27 p 315] and the fact that the beam is not perfectly monochromatic, so that the exact diffraction condition is satisfied over a small angular range [16 p 40].

**2.2.3.2. Analyzing the diffraction pattern.** A significant number of parameters are related to the intensity of the reflections in a diffraction pattern, so it is important that integration of the reflections is as accurate as possible. Each pixel on a 2D detector records an intensity, and since one reflection will span multiple frames and a range of  $\omega$  angles, the contribution to the intensity must be summed throughout a 3D box. If the box contains one reflection, the background is determined from the average pixel intensity outside the reflection envelope. The background is suspected to vary linearly throughout the box and thus a background contribution can be subtracted from each pixel within the box. Also, since it takes a finite time to scan  $\omega$ , the intensity is normalized to counts/second by dividing by the time to record the frame [27 p 328]. An extension of this box method assumes that the peak profiles of a subset of reflections in the same region of reciprocal space will be similar except by a scale factor. This profile fitting

method improves the quality of the data set and allows analysis of individual contributions to overlapping reflections, should they exist.

There is much systematic error affecting the accuracy of a diffraction experiment, which typically requires an adjustment of the measured intensities before they can be used to determine the structure. The predominant corrections to each integrated intensity,  $I_{hkl}$ , are the Lorentz-polarization factor,  $L_{phkl}$ , the x-ray absorption factor,  $A_{hkl}$ , the extinction factor,  $y_{hkl}$ , and a scaling factor,  $K_{hkl}$ , expressed in the equation [26 p XII-6]

$$I_{hkl} = L_{phkl} \cdot A_{hkl} \cdot y_{hkl} \cdot K_{hkl} \cdot |F_{hkl}|^2 \quad (2.8)$$

The Lorentz-polarization factor is really two factors combined because they both depend on the angle of scattering. The Lorentz factor accounts for the fact that the number of photons from a given reflection depends on the time the crystal plane causing that reflections remained in the diffracting condition during a measurement. This time is calculated from known constants such as the scan rate of the diffractometer but is dependent on the location of the reflection,  $\sin 2\theta$ . The measured intensity would then be divided by the time, which is directly dependent upon position, such that  $L_{hkl} = 1/(\sin(2\theta_{hkl}))$ . When the incident beam is considered to be unpolarized, (no monochromator used) the interaction with the crystal causes the diffracted beam to be partially or completely polarized, and does not have an equal intensity in each perpendicular direction. The degree of polarization of each reflection is also a function of the position, such that the polarization correction, without mediating constants and in the XY plane, is equal to  $p_{hkl} = (1 + \cos^2 2\theta_{hkl})/2$ . The combined  $L_p$  factor is

$$L_{phkl} = (1 + \cos^2 2\theta_{hkl})/[2(\sin(2\theta_{hkl}))] \quad (2.9)$$

The extinction factor, derived by Charles Darwin, is based on the interference of waves within the crystal. Primary extinction occurs when the reflected beam is in the exact position to be re-diffracted by other lattice planes, thereby causing a loss in intensity of the original reflection [27 p421]. This effect would be largest (50%) in a “perfect” crystal when all lattice planes are simultaneously diffracting. However, if certain mosaic spread is present, then only a fraction of the lattice planes would be in the diffraction condition simultaneously and the effect of extinction is minimized. The exact expression for the extinction factor relates to the size of a mosaic block of the crystal, generally unknown. So the extinction is calculated empirically, but is generally not large enough to be significant for most crystal samples and can be ignored. If warranted, it is now typically applied during refinement [27, p 436].

The absorption correction is arguably the most notable source of error in the intensities. As the X-ray incident passes through a crystal, a certain amount of the energy is initially absorbed by the atoms and some of it is diffracted. The energy absorbed depends on the thickness of the crystal and the types of atoms within the crystal. At different angles of rotation, the crystal thickness within the beam changes, varying the energy absorbed and thus varying the energy available for diffraction. The absorption factor has the general form

$$A_{hkl} = \frac{1}{V} \int_V \exp[-\mu(r_\alpha - r_\beta)] dV \quad (2.10)$$

where  $V$  is the crystal volume,  $\mu$  is the linear absorption coefficient for the crystal and radiation used,  $r_\alpha$  and  $r_\beta$  are the path lengths from the element of the crystal volume  $dV$  to the surface of the crystal along the incident and diffracted rays [26 p XII-9]. There are two main methods for calculating the absorption factor: either numerically or empirically

from the measured intensities. If the crystal has well defined edges and faces, these faces are indexed and measured using an optical microscope with a known orientation to the lab reference frame. Consequently the unique path through the crystal of each scattered ray can be determined. Sometimes, however, a crystal does not form with well-defined angles and faces. In these cases calculation of the absorption factor is done by comparing the measured intensities of equivalent reflections from different orientations of the crystal.

The measured intensities are relative numbers that relate to the experimental conditions. It is not correct to have the experimental conditions dictate the intensity magnitudes used for the structure factors. Therefore, the intensities must be converted from the relative scale of the experiment to the “electron density” scale of the structure [27 p 378]. The scaling factor,  $K_{hkl}$ , is the ratio of the relative intensities to the calculated intensities of the reflections. The calculated intensities based on a finite set of the reflections combines information from the density, unit cell dimensions and the series of known constants from the other correction factors.

After the reflection intensities have been corrected, an analysis of the symmetry is conducted. This is done stepwise starting from the unit cell, merging or combining the reflections based on the lattice type and Friedel’s law. Then the systematic absences are checked to determine the most probable space group of the structure. Armed with the data so far derived from the experiment; unit cell dimensions, corrected intensities, and space group, now it is possible to determine the structure by generating the electron density map. Either the Patterson method or direct methods is used to calculate the phases which are combined with the measured intensities to calculate the structure factor,

F, followed by a Fourier transform to produce an electron density distribution map showing the structure. If the sample contains a heavy atom, the Patterson method is preferred, while light atoms structures are best solved using the phases from Direct methods. Actually, the initial structure solution is a trial structure. A trial structure is a preliminary structure with approximate values to the “true” structure, such that it can be refined to remove the discrepancies [4 p102].

**2.2.3.3. Refining the structure and results.** Refinement of the trial structure is the process of systematically varying the atomic parameters in order to give the best possible agreement between the measured structure factor amplitudes and those calculated from the proposed structure [4 p 151]. The trial structure is usually inaccurate due to the use of estimated phases so that atoms may be the wrong type or missing, the positions of the atoms are not quite accurate and hydrogen atoms are missing. However, the trial structure is then adjusted using geometrical knowledge of bonding to define better positions for the atoms. This allows for better determination of the phases and an improved electron density map. The electron density map is often referred to as the difference map,  $F_o - F_c$ , because it is the difference between two structure factors; the observed structure factors,  $F_o$ , calculated from the observed structure factor amplitudes with the calculated phases from the atomic model, and the calculated structure factors,  $F_c$ , calculated from both the structure factor amplitudes and phases from the atomic model [25]. In order to minimize the difference between the  $F_c$  and  $F_o$ , refinement is done, usually by the process of least squares.

Least squares is a common technique used to determining the best fit of an assumed model to a set of experimental data. Least squares works when there are more

experimental data than parameters to determine. Parameters include, but are not limited to, the scaling factor, the atomic coordinates and displacement parameters for each atom. For good refinement, a data to parameter ratio of 10:1 is needed. The best parameters are assumed for the model by minimizing the sum of the squares (M) of the deviations between the experimental quantities and the model quantities. This is applied to the structure factors with equation:

$$M = \sum w(F_o^2 - F_c^2)^2 \quad (2.11)$$

where w is a weighting factor based on the error ( $\sigma$ ) of the measurement such that the greater the estimated standard deviation for a measurement, the lower the weight assigned to that measurement [4 p158]. When equation 10 is minimized it is seen graphically with a close to zero value over the entire difference map indicating that the experimental observations match what would be calculated from the model structure.

The results of the X-ray diffraction experiment are the positions of the atoms within a structure and their displacement parameters, from which inter and intra-atomic distances and interactions are shown. This information is typically manifested in an ORTEP diagram of the structure. However, since much of the refinement process relies on the researcher's adjustment of the model and subsequent fit of that model, it is desirable to have some quantitative factors from which to judge. Quality is usually based on three final R-factors, the weighted-R, wR,  $R_1$ , and the goodness of fit, S.  $R_1$  is the most common value as it is based on the structure factors F, and not the square of the structure factors,  $F^2$ . Low values of  $R_1$ , preferably below 5%, are considered of good quality. The weighted-R is most closely related to the refinement against  $F^2$  and low values of <12% are good. The goodness of fit contains the data to parameter



consideration and has a value close to 1.0 for a good quality fit. Equations for each are listed below (Figure 2.7).

$$wR = \left[ \frac{\sum w(F_o^2 - F_c^2)^2}{\sum wF_o^2} \right]^{1/2} \quad R = \frac{\sum ||F_o| - |F_c||}{\sum |F_o|} \quad S = \left[ \frac{\sum w(F_o^2 - F_c^2)^2}{(N_R - N_P)} \right]^{1/2}$$

**Figure 2.7.** Equations of residual R-values.  $N_R$  = number of independent reflections;  $N_P$  = number of refined parameters. All other variables are defined in the text [25].

### 3. TEMPERATURE EFFECTS ON X-RAY STRUCTURAL DETERMINATION OF A SPIN CROSS-OVER Fe(III) COMPLEX

#### 3.1. INTRODUCTION

The spin cross-over (SCO) phenomenon was first demonstrated in ferric complexes of tris(N,N-dialkyldithiocarbamate) in 1931 [28]. Since then, many Fe(III) compounds have been shown to exhibit SCO behavior from the LS ( $S=1/2$ ) state to the HS ( $S=5/2$ ) state, both paramagnetic. In contrast to Fe(II) compounds, Fe(III) SCO compounds are air stable. The effects of chemical modifications can be inconsistent between SCO systems and not generally predictable [29]. Therefore, more systematic studies are needed especially for determining the behavior of promising materials.

A class of compounds, in which we are particularly interested, is the Fe(III) SCO compounds containing ligands from the condensation of salicylaldehyde with pyridine. Complexation of both substituted and unsubstituted types of this ligand, N-(pyridin-2-ylmethyl)-salicylideneamine (Hsalpm), with potential SCO metals; Fe<sup>2+/3+</sup> [3,30], Mn<sup>2+/3+</sup> [31,32], Co<sup>1+/3+</sup> [33,34] yields complexes with unknown or absent SCO behavior. However, the coordination of Hsalpm with Fe(III) has become by far the most interesting, as a catalyst for polymerization reactions [35,36], but more particularly for its two-step, two-site, spin transition.

The octahedrally coordinated cation, [Fe(salpm)<sub>2</sub>]<sup>+</sup> has been synthesized with the counter ions Cl<sup>-</sup> [37], NO<sub>3</sub><sup>-</sup> [38,30] ClO<sub>4</sub><sup>-</sup> [3, 39] and now BF<sub>4</sub><sup>-</sup>. However, the magnetic properties have only been explored in the case of a NO<sub>3</sub><sup>-</sup> and ClO<sub>4</sub><sup>-</sup>. The hydrated sample of [Fe(salpm)<sub>2</sub>](NO<sub>3</sub>)<sub>2</sub> showed a gradual, thermal phase transition temperature of ~170 K

[30]. Whereas the  $[\text{Fe}(\text{salpm})_2]\text{ClO}_4 \cdot 0.5\text{EtOH}$  complex showed a two-step thermal transition at  $T_c(\text{S1}) = \sim 180\text{K}$  and  $T_c(\text{S2}) = \sim 100\text{K}$ , determined by x-ray crystallography to be due to two crystallographically independent metal centers [3]. Alternatively, Tang et al. [204] modified salpm by the addition of a H-bond acceptor, methoxy group to the benzene ring to form 2-methoxy-6-(pyridine-2-ylhydrazonomethyl)phenol (mph). The results indicated a sharpening of the two-step thermal transitions with a wide 45 K intermediate state where both Fe1 and Fe2 sites undergo concurrent spin transitions but also a slight increase in the transition temperatures compared to  $[\text{Fe}(\text{salpm})_2]\text{ClO}_4 \cdot 0.5\text{EtOH}$ . The concerted spin transition was attributed to the increased cooperativity from H-bonding in the structure, such that the Fe sites are not magnetically isolated from each other. The comparison of the SCO properties of the salpm vs the mph complexes are complicated by different solvent inclusion, MeOH and H<sub>2</sub>O for mph and EtOH for salpm. The addition of a methoxy group has a profound effect on the SCO properties of the Fe(III)(salpm)<sub>2</sub> system. It would be helpful to note how a more subtle change in the molecular packing and cooperative interactions, *via* replacement of only the counterion, would affect the spin transition curve.

Therefore, the compound,  $[\text{Fe}(\text{salpm})_2]\text{BF}_4 \cdot 0.5\text{EtOH}$ , was synthesized by Dr. Mussa Shongwe's group with which we collaborated to contribute the X-ray structural analysis. The magnetic measurements have not yet been determined. However thorough analysis of the X-ray structure is able to predict the magnetic behavior of the  $\text{BF}_4^-$  complex with analogy to the two-step transition seen in the  $\text{ClO}_4^-$  complex. Therefore, in order to complete the systematic study of this series of  $\text{Fe}(\text{III})(\text{salpm})^{2+}$  SCO

complexes, the single crystal X-ray structure of  $[\text{Fe}(\text{salpm})_2]\text{BF}_4 \cdot 0.5\text{EtOH}$  was measured at four different temperatures from 100K-298K.

### 3.2. BACKGROUND OF SCO

Low spin and high spin metals occur due to the interplay of the pairing energy of d electrons and the ligand field splitting energy in a complex. If pairing of two electrons of opposite spin requires more energy than that which separates the d orbitals in a particular ligand field, a high spin configuration will result. If pairing of spins requires less energy than the splitting energy of the orbitals, a low spin configuration results. The size of the energy gap between the d orbitals is determined by the specific metal and ligand involved. Strong field ligands produce large energy gaps while weak field ligands exhibit small energy gaps. If the ligand field splitting energy is close enough to the mean pairing energy of the electrons, outside stimuli, such as heat, light, or pressure can induce a change from high spin to low spin or vice versa. Such compounds are referred to as spin crossover (SCO) compounds.

**3.2.1. Applications.** It was realized in the 1980s that SCO compounds could be used as active memory devices [41] and have been of interest primarily for their potential in molecular based devices ever since. Memory storage devices require material with good hysteresis and bistability [42]. SCO transformations instigated by light have potential for optics and displays [43, 44]. For example, the Fe(II) compound,  $(\text{Fe}(\text{pyrazine})(\text{Pt}(\text{CN})_4))$  where the switching from LS to HS and HS to LS can be accomplished by the same energy photon [45]. Thermal SCO materials with room temperature transitions and hysteresis are the ideal for devices, but tunable transition

temperatures can be very desirable in magnetic devices as demonstrated with molecular alloys [41].

**3.2.2. Mechanism.** Researchers qualitatively describe and explain a SCO event in terms of cooperativity, molecular bistability, percent completion and conversion rates. The cooperativity effect is a coupling between the molecular and intermolecular movements within a sample [46]. It is also described as the forces between the molecules propagating structural changes to the whole lattice [29]. Bistability refers to the ability of a molecular system to exist in two electronic states within a range of external perturbations [47]. A complete spin transition is characterized by 100% of the molecules within the sample switching to the opposite spin state. The spin transition can also be described using one temperature, pressure or magnetic strength etc. at which 50% of the metal centers are in each spin state and denoted as  $T_{1/2}$  or  $P_{1/2}$  etc. Within the range of the physical measurement the fractions of HS and LS states can be calculated assuming additive properties of the magnetic susceptibilities of the states [2].

**3.2.3. Physical Methods to Study SCO.** The SCO phenomenon in many materials is most commonly a result of temperature changes. Thermal SCO transitions can be abrupt, converting discontinuously from LS to HS within a couple Kelvin; gradual, with conversion over a wider temperature range; or even multi-stepped, where a fraction of the spin sites cross over in a particular temperature range. Gradual conversion, sometimes coined spin equilibrium [2], is characterized by small structural changes due to weak intermolecular cooperativity [48]. Large cooperativity serves as a prerequisite for fast spin transitions. Multi-stepped transitions are usually a result of two different lattice sites that exhibit different SCO transition temperatures [49]. Thermodynamic

experiments in the 1970s by Sorai and Seki [50] indicated that the entropy change of a LS→HS transition was much higher than theoretically calculated for the electronic transition. This can be simply explained by an increase in the number of electrons in the anti-bonding orbitals weakening the M-L bonds and decreasing the vibrational frequencies contributing to a more entropic HS state [51].

Pressure, while not as popular, can dramatically affect SCO as it will change the metal-donor bond lengths or volume thereby favoring the LS state. Pressure changes can be valuable to measure the thermodynamic and mechanistic parameters of a SCO process, for example the cooperativity factor, intermolecular interaction free energy, short and long range interactions, phase transitions and ligand field strength [52]. Mean field theory predicts that as pressure is increased, an increase in the transition temperature along with a decrease in the width of the hysteresis loop and slope of the %HS/T curve occurs. For pressure studies it is important to apply hydrostatic pressure as shearing, milling and crystal defects all deform the SCO transition curve under non-hydrostatic conditions. While adequate quantitative theory has not been developed for 1D, 2D and 3D systems, which are important for their possible practical applications, continued pressure investigations of these SCO systems will develop greater insight into their unique cooperative interactions[52]. Since pressure changes inevitably induce changes in the crystal structure of a material, researchers have used Raman spectroscopy to probe the effects of pressure. In a complex of  $\text{Fe}(\text{pyrazine})[\text{Ni}(\text{CN})_4] \cdot 2\text{H}_2\text{O}$ , a hysteresis effect with  $P_{1/2\uparrow} = 1350$  bar and  $P_{1/2\downarrow} = 650$  bar, was exhibited with the use of pressure instead of temperature [53].

LIESST (Light Induced Excited Spin State Trapping) converts a thermally stable LS state to a metastable HS with light irradiation;  $^5T_2 \leftarrow ^1A_1$  for Fe(II) and  $^6A_1 \leftarrow ^2T_2$  for Fe(III) [54]. Then the HS state is kept at a low temperature, trapping the electron to prevent it from relaxation back to LS. Initially studied in the early 1980s by Descurtins et al. [55], McGarvey et al. [56-58] and then extensively by Hauser et al. [59], the LEISST effect has been displayed by a variety of compounds such as  $[Fe(tmphen)_2]_3[Co(CN)_6]_2$  (tmphen= 3,4,7,8-tetramethyl-1,10-phenanthroline) in which a photoconversion efficiency of 20% of the equatorial HS Fe(II) centers is found [60]. Light has also been used in ligand-driven light induced spin change (LD-LISC) when a potentially photo-isomerizable ligand is incorporated into the compound and affects the SCO transition event. Fe(III) compounds of  $[Fe(salten)(Mepepy)]BPh_4$  (Mepepy = 1-(pyridine-4-yl)-2-(N-methylpyrrol-2-yl)-ethene) show a partial spin conversion to HS upon photo-isomerization of the Mepepy ligand from trans to cis [61].

Most commonly the domain model and regular solution model are used to explain the SCO behavior of molecules. Within the domain model abrupt transitions with hysteresis are caused by the formation of spin state domains within the sample and strong cooperativity [62]. Weak cooperativity results in a more random distribution of spin states throughout [62]. The domain mechanism explains that a domain of one spin state should nucleate and grow to a critical size to overcome some activation barrier in order to exist within a lattice of mixed spin states. Small domain sizes are apparent in gradual spin conversions [63] compared to large domains in fast spin transitions [64,65]. The regular solution model proposed by Slichter and Drickamer [66] provides thermodynamic quantities for SCO events, specifically with a cooperativity strength factor, entropy, and

enthalpy using fractions of HS and LS species. The model treats a SCO sample as a mixed regular solution of two randomly distributed spin states [66].

**3.2.4. Chemical Changes that Affect SCO Behavior.** Even with the expanded study of SCO compounds in recent years and progress in determining the conditions that affect SCO behavior, design of compounds exhibiting an adequate balance of properties important for wide applications remains difficult. A change in the counter ion[67-70], solvate molecules[71,72], sample preparation [73,74], protonation state[67,75] or configurational isomer[76] of the ligand, substituents [77-79] and hydrogen bonding[40] can all drastically affect the characteristics of the SCO. For example simple movement of the NO<sub>2</sub> substituent from the 3 to 5 position in [Fe(NO<sub>2</sub>-Salztrien)](PF<sub>6</sub>) results in a decrease in the HS isomer from 49% to 19% at room temp[77]. The complex of [FeL<sub>2</sub>]<sub>2</sub>NCS (L<sub>2</sub> = tridentate Schiff base formed by 1:1 condensation of 8-aminoquinoline and salicylaldehyde) shows a conversion from LS to HS after 15 days when crystallized below 280 K, or in 30 min at 315 K [74].

Other types of transitions can occur during or in conjunction with a spin transition. A change in spin state can, as in the case of Fe<sup>2+</sup>, convert a diamagnetic LS complex to paramagnetic HS. In the solid state, crystallographic phase changes can accompany LS↔HS transitions as the change in ground state can significantly change the molecular geometry [46, 80]. As in the example of [Fe(L<sub>2</sub>)]ClO<sub>4</sub> (L<sub>2</sub>= N,N'-bis(2-aminoethyl)-1,3-propanediamine + 4,6-dimethoxysalicylaldehyde) which converts from a HS phase where all the molecules possess C<sub>2</sub> symmetry, to an intermediate phase where one of the two crystallographically independent molecules has C<sub>2</sub> symmetry and an increase in the unit cell volume by 1.5 times [81]. Color changes can also be attributed to



the structural changes brought on by the spin crossover transition [82-85]. A chemical with good cooperativity,  $[\text{Fe}(\text{brrz})_2(\text{NCS})_2] \cdot \text{H}_2\text{O}$  (brrz = 4, 4'-bis-1,2,4-triazole) undergoes a spin allowed d-d transition at 520nm in the LS state and converts with a transition in the near IR region, causing a color change from violet to white [44].

### 3.3. EXPERIMENTAL

Single, black crystals of  $[\text{Fe}(\text{salpm})_2]\text{BF}_4 \cdot 0.5\text{EtOH}$  were formed by solvent evaporation from ethanol. Single crystal X-ray diffraction data collection and analysis were performed on a Bruker SMART APEXII diffractometer with a sealed tube,  $\text{K}_\alpha$  Mo source ( $\lambda=0.71073 \text{ \AA}$ ), graphite monochromator and CCD detector. An Oxford 700 Cryostream N2 open-flow temperature system was used. Measurements were taken on a crystal of  $[\text{Fe}(\text{salpm})_2]\text{BF}_4 \cdot 0.5\text{EtOH}$  that was flash-cooled to 100K and progressively increased at a rate of 5 K/min sequentially to 175 K and 225K. Another, but separate, crystal from another synthesis was run at 296K. The unit cell refinement and the integration of the diffraction frames were done with Bruker SAINT. Intensity data were corrected for Lorentz and polarization effects. Absorption corrections were applied using SADABS and the structures were solved by direct methods and refined using least squares with the SHELXL-97 software program. Calculation of geometrical parameters was conducted using Mercury and figures were made using ORTEP, Mercury, PLATON, or SHELXTL. Hydrogens were placed in calculated positions and isotropically refined using a riding model.

**3.3.1. LS-LS 100K Structure Solution and Refinement.** A black crystal fragment of dimensions 0.14 x 0.28 x 0.62 mm was centered on the diffractometer with a

0.5mm collimator. Unfortunately, the large third dimension caused some of the crystal to extend outside the x-ray beam at some angles. At 100K, an empirical multi-scan absorption correction was applied as the absorption coefficient,  $\mu = 0.66 \text{ mm}^{-1}$ , was high enough for absorption to have a significant effect on the intensities. The data collection strategy sampled diffraction space out to an angle  $\theta_{\text{max}} = 27.1^\circ$  measuring 59019 reflections. Reflections related by symmetry or repeatedly measured were combined to generate 11159 independent reflections, of which, 8783 reflections were of an intensity greater than two times the standard deviation in intensity ( $>2\sigma(I)$ ). The error associated with the intensity of the equivalent reflections is expressed by a  $R_{\text{int}}$  value of 0.043, and provides a good measure of the overall error in the experimental data. All this data is tabulated along with the other temperature structures in Table 3.1.

**Table 3.1.** Crystal data and structure refinement for  $[\text{Fe}(\text{salpm})_2]\text{BF}_4 \cdot 0.5\text{EtOH}$ .

	100K	175K	225K	296K
<u>Crystal Data</u>				
Chemical Formula	$(\text{C}_{26}\text{H}_{22}\text{FeN}_4\text{O}_2)(\text{BF}_4) \cdot 1/2(\text{C}_2\text{H}_6\text{O})$	$(\text{C}_{26}\text{H}_{22}\text{FeN}_4\text{O}_2)(\text{BF}_4) \cdot 1/2(\text{C}_2\text{H}_6\text{O})$	$(\text{C}_{26}\text{H}_{22}\text{FeN}_4\text{O}_2)(\text{BF}_4) \cdot 1/2(\text{C}_2\text{H}_6\text{O})$	$(\text{C}_{26}\text{H}_{22}\text{FeN}_4\text{O}_2)(\text{BF}_4) \cdot 1/2(\text{C}_2\text{H}_6\text{O})$
$M_r$	1176.34	1176.34	1176.34	1176.34
Crystal System, space group	Monoclinic, $P2_1/n$	Monoclinic, $P2_1/n$	Monoclinic, $P2_1/n$	Monoclinic, $P2_1/n$
$a, b, c$ (Å)	15.2232(13), 18.7470(16), 17.7838(15)	15.4618(5), 19.2516(7), 17.4008(7)	15.7991(5), 19.2895(7), 17.2767(7)	15.9080(7), 19.3177(9), 17.4294(8)
$\beta$ (°)	93.1280(10)	92.9640(10)	93.0420(10)	93.252(3)
$V$ (Å <sup>3</sup> )	5067.7(7)	5172.7(3)	5257.8(3)	5347.5(4)
$Z, Z'$	4, 2	4, 2	4, 2	4, 2
Radiation Type	Mo/ $K_\alpha$	Mo/ $K_\alpha$	Mo/ $K_\alpha$	Mo/ $K_\alpha$
$\mu$ (mm <sup>-1</sup> )	0.661	0.648	0.637	0.627
Crystal form, size (mm)	fragment, 0.14x0.28x0.62	fragment, 0.14x0.28x0.62	fragment, 0.14x0.28x0.62	chip, 0.15x0.3x0.7

**Table 3.1.** Crystal data and structure refinement for [Fe(salpm)<sub>2</sub>]BF<sub>4</sub>•0.5EtOH. (cont.)Data Collection

Diffractometer	SMART APEX II	SMART APEX II	SMART APEX II	SMART APEX II
Absorption correction	multi-scan	multi-scan	multi-scan	multi-scan
No. of measured, independent and observed reflections	59019, 11159, 8783	60722, 10979, 7920	51477, 9433, 7058	150774, 13255, 8116
Criterion for observed reflections	$I > 2\sigma(I)$	$I > 2\sigma(I)$	$I > 2\sigma(I)$	$I > 2\sigma(I)$
$R_{int}$	0.043	0.045	0.044	0.049
$\theta_{max}$ (°)	27.1	26.7	25.1	28.3

Refinement

Refinement on $R[F^2 > 2\sigma(F^2)]$ , $wR(F^2)$ , S	$F^2$ 0.047, 0.121, 1.02	$F^2$ 0.054, 0.145, 1.021	$F^2$ 0.051, 0.142, 1.05	$F^2$ 0.058, 0.182, 0.79
Data/ restraints/ parameters	11159/51/732	10979/0/712	9433/80/754	147621/44/685
H-atom treatment	constrained	constrained	constrained	constrained
Weighting scheme (w), $P=(F_o^2+2F_c^2)/3$	$1/[\sigma^2(F_o^2)+(0.0649P)^2+6.6122P]$	$1/[\sigma^2(F_o^2)+(0.0872P)^2+5.0243P]$	$1/[\sigma^2(F_o^2)+(0.0834P)^2+4.2829P]$	$1/[\sigma^2(F_o^2)+(0.1673P)^2+2.3838P]$
$(\Delta/\sigma)_{max}$	0.001	0.001	0.001	0.013
$\Delta\rho_{max}$ , $\Delta\rho_{min}$ (e Å <sup>-3</sup> )	1.250, -0.688	0.945, -0.672	0.872, -0.521	0.682, -0.438

After integration and scaling of reflections, the phases of the reflections were determined by Direct Methods to produce a trial structure. Initial refinement allowed for easy determinations of both the cation and anion positions in the difference electron density map. Along with the position data, (x,y,z) for each atom, an isotropic displacement value, U, is also given.

The isotropic displacement value is related to the volume of a sphere in which the electrons are found using the assumption that atoms and bonds oscillate equally in all

directions. This motion of atoms is included as a correction to the atomic scattering factor in the equation:

$$f = f_0 \exp(-(B_{\text{iso}} \sin^2 \theta) / \lambda) \quad (3.1)$$

where  $f_0$  is the original atomic scattering factor, and  $f$  is the atomic scattering factor corrected for the motion of the atom.  $B_{\text{iso}}$ , the isotropic parameter, is related to the mean amplitude of the atom's vibration,  $\bar{u}^2$ , in the equation,  $B_{\text{iso}} = 8\pi^2 \bar{u}^2$ , and  $U = \bar{u}^2$ . A typical value of  $U$  is  $0.050 \text{ \AA}^2$  for a room temperature structure.

However, the assumption that atoms vibrate equally in all directions is intrinsically invalid, and given high quality diffraction data, it is possible to more accurately describe the vibration separately in three different directions in the form of an ellipse. This is done using six parameters, wherein the isotropic  $U$  value is replaced with  $U_{ij}$  values in the scattering factor equation (equation 3.1); three describing the radii of the ellipse and three describing the orientation of the ellipse [16]. The motion of the atom is then described anisotropically and the value of these anisotropic displacement parameters (ADP) can vary widely but are similar in magnitude to the isotropic  $U$ -value.

Atomic motion is greatly influenced by temperature, thus the ADPs for each structure reflects not only how precisely the positions of atoms can be determined by the measured data, but also if specific motion is occurring by the presence of different conformations in the crystal lattice. Less motion and thus smaller ADPs are present for atoms near the center and conformationally rigid portions of molecules. It is not unusual to find larger ADP for atoms on the periphery of a molecule or for atoms with a large degree of rotational freedom. Table 3.2 shows both isotropic and anisotropic parameters for a sample of the atoms in the  $[\text{Fe}(\text{salpm})_2]\text{BF}_4 \cdot 0.5\text{EtOH}$  complex at different

temperatures. It is very apparent that the low temperature, 100K, significantly reduces the average ADP by 50-60% from room temperature, 296K. The anisotropic values of F2 indicate that the atom moves or is displaced twice as much in one direction ( $U_{33}$ ) as in any other, irrespective of temperature.

**Table 3.2.** Atomic displacement parameters of  $[\text{Fe}(\text{salpm})_2]\text{BF}_4 \cdot 0.5\text{EtOH}$ . Isotropic/Equivalent ( $U_{\text{eq}}$ ) and Anisotropic ( $U_{ij}$ ) values in square angstroms ( $\text{\AA}^2$ ) for a sample of atoms at each temperature.

		<b>Fe1</b>	<b>O101</b>	<b>C9</b>	<b>F2</b>	<b>O1S</b>
<b>100K</b>	$U_{\text{eq}}$	0.01951(10)	0.0261(4)	0.0252(6)	0.0757(8)	0.0968(12)
	$U_{11}$	0.01455(18)	0.0221(9)	0.0257(14)	0.0486(13)	0.107(3)
	$U_{22}$	0.02342(2)	0.0332(11)	0.0230(13)	0.0650(15)	0.105(3)
	$U_{33}$	0.02088(19)	0.0233(10)	0.0269(14)	0.119(2)	0.079(2)
<b>175K</b>	$U_{\text{eq}}$	0.03733(14)	0.0421(5)	0.0596(12)	0.1136(13)	0.156(2)
	$U_{11}$	0.0252(2)	0.0469(13)	0.084(3)	0.0684(18)	0.220(6)
	$U_{22}$	0.0539(3)	0.0453(13)	0.054(2)	0.086(2)	0.133(4)
	$U_{33}$	0.0332(2)	0.0342(12)	0.039(2)	0.192(4)	0.118(4)
<b>225K</b>	$U_{\text{eq}}$	0.03932(15)	0.0488(6)	0.0515(9)	0.142(5)	0.302(5)
	$U_{11}$	0.0281(3)	0.0498(15)	0.055(2)	0.107(6)	--
	$U_{22}$	0.0457(3)	0.0544(15)	0.049(2)	0.114(6)	--
	$U_{33}$	0.0448(3)	0.0424(14)	0.050(2)	0.215(12)	--
<b>296K</b>	$U_{\text{eq}}$	0.04884(15)	0.0619(6)	0.0625(8)	0.281(4)	--
	$U_{11}$	0.0359(2)	0.0611(14)	0.061(2)	0.138(4)	--
	$U_{22}$	0.0527(3)	0.0676(15)	0.059(2)	0.177(4)	--
	$U_{33}$	0.0590(3)	0.0572(12)	0.068(2)	0.544(12)	--

After a couple more cycles of Least Squares refinement, the ethanol molecule showed larger isotropic ADPs than the rest of the structure by at least a factor of 10. This can be attributed to the large amount of thermal motion of the solvent that is trapped in a void within the lattice produced by the complex. Outstandingly large ADPs can also be a clue to partial occupancy of the solvent. Specifically in the case of spin crossovers, the way the ADPs change with temperature can also indicate an asymmetry in the way the central atom shrinks as it moves into the lower spin state.

Most atoms within the asymmetric unit are present in the same conformation in every asymmetric unit of the crystal. However, when an atom is present in only about half the asymmetric units of the crystal, it is a case of structural disorder where the atom sites are said to be half occupied. This is often the case concerning solvent molecules, as some of the solvent may be lost over time through evaporation. Another case in which the occupancy of an atom is not unity, is when it resides on a symmetry element. For example, when an atom lies on a mirror plane, only half of the atom will reside in the asymmetric unit. The other half is generated by the mirror operation. Such an atom would have 0.5 occupancy. An atom on a 4-fold axis would have 0.25 occupancy.

In the case of the 100K ethanol molecule, the abnormally large ADPs were a result of conformational disorder and not partial occupancy. Partial occupancy is better characterized by negative electron density around the atom positions [86]. Two different conformations of the ethanol molecule were determined. The ethanol molecule resides in one conformation/position in 73% of the asymmetric units of the crystal while in the other 27% of the asymmetric units, it is in the other conformation. This ratio was initially arbitrarily set at a random value, but then refined during least squares. Additional

constraints and restraints were applied to the ethanol, followed by anisotropic refinement of the entire structure. The resulting  $R_1$ -values decreased significantly from ~10% to 6%. Addition of constrained hydrogen atoms further improved the model, and with a couple extra cycles of least squares, the model converged to an overall  $R_1 = 4.67\%$ .

**3.3.2. LS-HS 175K Structure Solution and Refinement.** The data collection strategy was somewhat different for the 175K structure, but reduction and solution methods were the same as the 100K structure. Refer to Table 2.1 for the data. Refinement proceeded quite similarly to the 100K structure. The ethanol solvent exhibited large isotropic ADPs, however, any discernable alternate conformations could not be found. Any alternate positions suggested, combined with geometrical constraints and restraints only resulted in greater deviation of the model structure from the observed structure factors. This can also be a result of a conglomeration of multiple disorder positions, each contributing amounts small compared to the accuracy the data can resolve them. Deviation of the model is typically displayed in an increase in both  $R_1$  and  $wR_2$ . Reduced occupancy, while not probable, was also attempted, without success. The large isotropic ADP of the ethanol, persisted after anisotropic refinement of the entire structure, but was concluded as the best representation of the electron density given the measured data. In such cases when there isn't strong force like good H-bonding to hold a solvent atom in place, there's a risk of multiple positions as well as some loss of solvent, leading to lower occupancy.

After anisotropic refinement, it is many times possible to locate hydrogen atom density in the difference map. However, the positions must remain consistent and of practical geometry throughout refinements. Many times this is not the case due to the

low scattering ability of hydrogen and displacement of the electron relative to the nucleus. Therefore, the hydrogens are calculated. One method frequently used is the riding model constraint, called thus because the hydrogen is said to “ride” on the atom to which it is bonded (X). Initially, the hydrogen atoms are placed at geometrically ideal positions based on their bonded atoms and the temperature. The isotropic parameter of the hydrogen is also constrained to be 1.2-fold in value of its bonded atom, 1.5-fold if the atom is terminal. During least squares refinement, if the bonded atom alters position or changes ADP value, the hydrogen will also maintain the geometry. The hydrogen positions for all the  $\text{Fe}(\text{salpm})_2\text{]BF}_4 \cdot 0.5\text{EtOH}$  structures were calculated using a riding model. The riding model does not add any more parameters than defining the electron density peaks, but it does improve convergence of the model.

For the 175K structure, addition of the hydrogens, indeed decreased the R-values. The  $\text{BF}_4$  anions did show some dispersion in electron density expected from the increased temperature and rotational freedom of the molecule. However, again, alternative positions were tried but only to the demise of the model fit. The  $\text{BF}_4$  anions were anisotropically refined with large ellipsoids. The model was able to converge to a final  $R_1 = 5.40\%$ .

**3.3.3. HS-HS 225K Structure Solution and Refinement.** At the next temperature, 225 K, the data collection strategy was again different, hence the differences in the  $\theta_{\text{max}}$  and number of measured reflections for each temperature (Table 3.1). Data reduction and scaling remained the same as the previous temperatures. However, for refinement the increase in temperature, caused the ADPs of the atoms to increase in size



and distort in shape. The effect was strong enough to incorporate significant positional disorder in both the ethanol and  $\text{BF}_4$  ions.

Disorder is the presence of different orientations of the molecules in different unit cells. The structure determined from the diffraction pattern is the spatial average of the entire crystal. Deconvoluting this spatial average can sometimes be very difficult. Positional disorder, frequently present, is where one atom occupies two or more positions within the unit cell. Large ADPs relative to others in the structure and oblong ellipsoids are sure signs of this type of disorder. It is possible to define the model structure differently, so that this disorder of the electron density can be mapped out or separated rationally in order to produce a better fit to the observed data.

Disorder requires the use of constraints and restraints. A constraint is an exact mathematical condition that removes variables from the Least squares refinement. An example would be the riding model constraint. The use of constraints is avoided if possible in favor of restraints. Restraints are added conditions that are not exact but subject to a probability distribution. During refinement, restraints are treated like additional experimental data with refinable error and weight relative to the X-ray data. Restricting two bond lengths, known to be chemically equivalent, to be equal within a certain standard deviation is one example of a restraint and was used for the disorder in the  $\text{BF}_4$  anions at 275K.

Chemically both  $\text{BF}_4$  anions in the asymmetric unit should have equal bond lengths and angles. This is the basis of the SAME instruction that was used to restrict the 1,2- and 1,3-bond distances of one  $\text{BF}_4$  to be the same as the other  $\text{BF}_4$  within an effective standard deviation of 0.02 Å. The disorder of both  $\text{BF}_4$  showed a rotation of

three of the fluorine atoms into two major positions. This type of continuous rotational disorder is hard to model and is most often modeled by two or three components generally accepting elongated ellipsoids. So the ADPs of the fluorine atoms were also restrained to be approximately equal but still showed the elongated ellipsoids. Since two positions were modeled for each  $\text{BF}_4$ , the occupancy of the disordered fluorines was set to one, but such that the ratio of one position to the other could be varied during refinement.

Given the increased rotational freedom of the  $\text{BF}_4$  anions, the electron density of the ethanol molecule showed even greater dispersion. The positions of the carbon atoms shifted considerably during refinement cycles so that the bond lengths were restrained to 1.3 Å for the O-C bond and 1.5 Å for the C-C bond each within a standard deviation of 0.02 Å. The ethanol molecule was only isotropically refined, as anisotropic determination retained the spherical shape of the ellipsoids and reduced agreement of the model. As such, the model of the complete structure converged with 80 total restraints to an  $R_1 = 5.07\%$ .

**3.3.4. HS-HS 296K Structure Solution and Refinement.** The first chronologically in the series of structures, the 298K structure data was collected from a different sample from an independent reaction. While the crystal habit remained similar, the quality of the crystal and data collection shortcomings produced a lesser quality data set and final structure. While the Patterson method of phase determination, regarded admirably for heavy-atom structures, did locate the iron positions, the locations of the organic portion of the molecule were not easily resolvable. Direct methods produced the most discernable bonded structure in the electron density map. Within a few least

squares refinement cycles, the difference electron density map exhibited most of the atom positions. However, the electron density distribution around the tetrafluoroborates was strongly dispersed and residual electron density was apparent from the ethanol solvate.

The disorder in the  $\text{BF}_4^-$  anions was handled differently than in the 225K structure, as alternate conformations were not consistent, caused mostly due to the differing data set. Using a combination of three commands, 44 restraints were added to the model structure. The distances and angles of the bonds in both  $\text{BF}_4^-$  anions were restrained to be equal within a 0.02 Å standard deviation. Also the ADPs of each of the fluorine atoms were restrained in the direction of the bond using the DELU command with 0.01 Å standard deviation. DELU restrains the component of the displacement parameters in the direction of the bond to be equal within a standard deviation. This restraint has been shown to be accurate for almost all structures. However, atomic displacement is greater in the two directions perpendicular to the bond so a SIMU command was used. Specifically, the SIMU command restrains the U-values of atoms within a distance of 1.7 Å (esd=0.04) to be the same. SIMU is not as accurate and is thus given a much larger esd than DELU restraints.

The ethanol molecule showed considerable disorder such that the electron density could not be refined to reproducible positions, but only a general location within the asymmetric unit as evidenced by the much larger  $(\Delta/\sigma)_{\text{max}}$  value for the 298K structure. At this point, the model fit was described by  $R_1=6.4\%$ ,  $wR_2=11.55\%$  and  $S=0.909$  but was not converging due to the fluctuating solvent positions. Convergence of the model was finally achieved by defining and eliminating the electron density contribution of the solvent from the reflections with a procedure known as SQUEEZE [87]. In SQUEEZE

the structure is separated into discrete and disordered parts. The contribution of the disordered part to the structure factor is calculated by a Fourier transform and included into the least squares refinement. The model containing both discrete-atom data and continuous solvent-area is refined to convergence [88]. SQUEEZE determined two void volumes about the positions  $(0, 0, \frac{1}{2})$  and  $(\frac{1}{2}, \frac{1}{2}, 0)$ , each with a volume of  $272 \text{ \AA}^3$  and electron count of 56. This approximately corresponds to two ethanol molecules at each position for a total of 4 in the unit cell. Only modest improvement of the R-values resulted, but the goodness-of-fit value (S) decreased even further to 0.794 (ideally around 1.0). This indicates that our model is better than the data warrants, however convergence was finally achieved.

According to the equation for S (Figure 2.7) the weighting scheme and absorption correction strongly affect this number. The absorption coefficient was not significantly different from the other crystal but the weighting scheme showed significant differences. This can be traced back to the error in intensity of the high resolution reflections. Compared to the other temperature data sets, the 298K structure exhibited a  $R_{\text{int}}=0.44$  at  $0.84 \text{ \AA}$  resolution, while 225K, 175K, and 100K structures showed values for  $R_{\text{int}}$  of 0.27, 0.27 and 0.14, respectively. The intensity of the low angle reflections (high resolution) was also lower for the 298K structure. Not only do the low angle reflections affect the weighting scheme, the number of recovered electrons calculated with SQUEEZE is also strongly dependent on their quality [87]. A summary of the disorder is found in Table 3.3.

**Table 3.3.** Summary of the treatment of disorder.

	100K	175K	225K	296K
Ethanol	2-positional disorder	single position	single position	Diffuse
Occupancy (%)	73:27	100	100	SQUEEZE
Restraints	SAME, SIMU	none	DFIX	Void vol = 545 Å <sup>3</sup>
ADPs	isotropic	anisotropic (large ellipsoids)	isotropic	Void e- = 112 e-
U <sub>(eq)</sub> (C1SA)	0.084(3)	0.150(3)	0.293(8)	4 EtOH/cell
BF <sub>4</sub> <sup>-</sup>	single position	single position	2-positional disorder	single position
Occupancy (%)	100	100	67:33 ; 73:27	100
Restraints	none	none	ISOR	SIMU, DELU, SAME
ADPs	anisotropic (large ellipsoids)	anisotropic (large ellipsoids)	anisotropic	anisotropic
U <sub>(eq)</sub> (F8)	0.0490(5)	0.1002(11)	0.111(3)	0.1738(18)

### 3.4. DISCUSSION

[Fe(salpm)<sub>2</sub>]BF<sub>4</sub>•0.5EtOH is isostructural to its precedent [Fe(salpm)<sub>2</sub>]ClO<sub>4</sub>•0.5EtOH [3]. However the BF<sub>4</sub> analog offers some distinct differences to the ClO<sub>4</sub> analog that emerge in the magnetic interactions. So, a comparison of not only the structural changes with temperature, but also between the two compounds is beneficial to understanding the SCO event in the series of complexes.

At all temperatures, [Fe(salpm)<sub>2</sub>]BF<sub>4</sub>•0.5EtOH crystallizes in the monoclinic space group, P2<sub>1</sub>/n, indicating that no phase transition occurs, and, as is typical, the space group is not affected by a spin state change. The tridentate salpm ligands easily induce a hexacoordinated octahedron by coordinating meridionally to iron(III) in a cis, trans, cis

arrangement of the phenolate O, imine N and pyridyl N, respectively, as seen in the ORTEP diagram (Figure 3.1). Due to the orthogonal nature of the cation, ideally C2

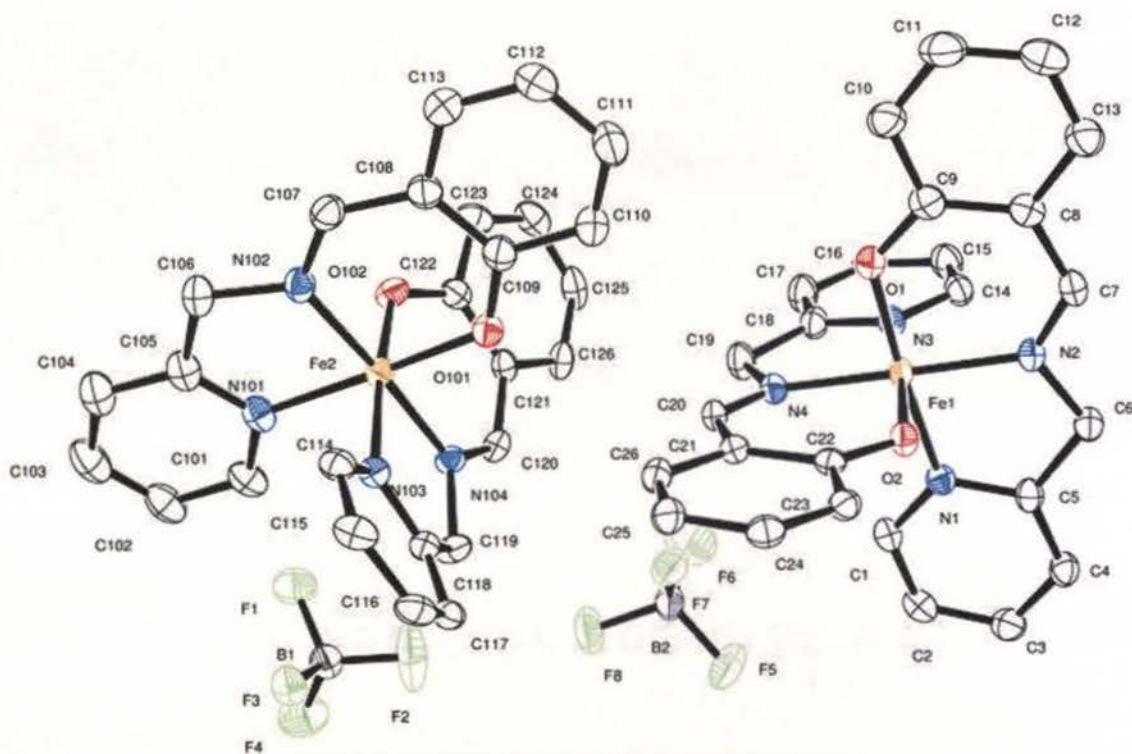


**Figure 3.1.** ORTEP diagram of of  $[\text{Fe}(\text{salpm})_2]\text{BF}_4 \cdot 0.5\text{EtOH}$ . Asymmetric unit at 100K with 50% thermal ellipsoids. Hydrogens and solvent ethanol removed for clarity.

symmetry, the asymmetric unit contains large spaces between two distinct Fe complexes, which are easily filled by two tetrfluoroborate anions and a solvent ethanol. The salpm ligands coordinated about the iron atoms, Fe1 and Fe2 are planer to different degrees. Most notably the benzene rings of the salpm ligand (O102-N103) angle towards each other by about  $30^\circ$  with a maximum deviation from the ligand plane occurring at C116.

The average angle between the ligand planes for Fe1 and Fe2 complexes is  $\sim 85^\circ$  and  $\sim 82^\circ$ , respectively, for all temperatures.

Similar to the SCO characteristics of the  $[\text{Fe}(\text{salpm})_2]\text{ClO}_4 \cdot 0.5\text{EtOH}$  complex, a SCO process was expected to occur for the  $\text{BF}_4$  analog. Determination of the spin state of an atom can frequently be derived from the coordination bond lengths of the metal. In an octahedral ligand field, the HS state ( $S=5/2$ ) in  $\text{Fe}^{3+}$  requires occupation of the  $d_{\sigma^*}$  anti-bonding orbitals compared to the LS state ( $S=1/2$ ) where the HOMO  $d_{\pi}$  is nonbonding. Thus, weakening and lengthening of the Fe-L bonds results during the SCO from LS $\rightarrow$ HS. The average bond lengths of iron(III) to the phenolate oxygen ( $\text{O}_{\text{ph}}$ ), pyridyl nitrogen ( $\text{N}_{\text{py}}$ ) and imine nitrogen ( $\text{N}_{\text{im}}$ ) for purely HS, related six-coordinate complexes are in the ranges 1.985-1.938, 2.168-2.224, and 2.051-2.155Å, respectively. Also for related purely LS complexes the bonds are in the ranges  $\text{Fe}^{\text{III}}-\text{O}_{\text{ph}} = 1.850$ -1.885Å,  $\text{Fe}^{\text{III}}-\text{N}_{\text{py}} = 1.993$ -2.024Å, and  $\text{Fe}^{\text{III}}-\text{N}_{\text{im}} = 1.905$ -1.961Å as determined by Shongwe et al. [3]. The average bond lengths of  $[\text{Fe}(\text{salpm})_2]^+$  are shown in Table 3.4 and indicate that the spin state of Fe1 is HS at 296K and 225K. At 175K, Fe1-L bonds fall somewhat into the gap of the above ranges, but have values closer to the LS state and are well within the ranges to be completely LS at 100K. The Fe2-L bond lengths are easily within the expected ranges for HS at 296K and 225K. At 175K, the bonds are shorter but can still be considered HS, while a significant decrease allows for values corresponding to pure LS at 100K.

In addition to the bond lengths, the entire octahedron around the iron is expected to distort further during a LS $\rightarrow$ HS spin transition. The geometric parameter,  $\Sigma$ , shown

to be heavily spin-state dependent, was introduced by Marchivie et al. [89] for Fe<sup>2+</sup> complexes. However, it has been shown to be accurate for other octahedral ions such as

**Table 3.4.** Average coordination bond lengths for [Fe(salpm)<sub>2</sub>]BF<sub>4</sub>•0.5EtOH.

	100K	175K	225K	296K
Fe1-N <sub>py</sub>	1.983(2)	2.051(3)	2.147(3)	2.159(3)
Fe1-N <sub>im</sub>	1.932(2)	1.994(3)	2.087(3)	2.099(2)
Fe1-O <sub>ph</sub>	1.874(2)	1.871(3)	1.908(3)	1.908(3)
Fe2-N <sub>py</sub>	2.023(2)	2.162(3)	2.172(3)	2.170(3)
Fe2-N <sub>im</sub>	1.955(2)	2.096(3)	2.098(3)	2.094(3)
Fe2-O <sub>ph</sub>	1.882(2)	1.918(3)	1.914(2)	1.911(2)
Σ (Fe1) (°)	53.3	51.9	79	81.0
Σ (Fe2) (°)	48.2	76.0	77	78.2

Fe<sup>3+</sup> as well [90]. Sigma, Σ, is taken to be the sum of the deviations from 90° for each of the 12 cis-coordination angles, with higher values being expected for HS complexes. This is indeed the case for [Fe(salpm)<sub>2</sub>]BF<sub>4</sub>•0.5EtOH as shown in Table 3.4. The Fe2 cation is shown to be HS down to 175K where Σ changes from ~76° to ~48°. Fe1 shows a spin transition between 225K and 175K shown by a similar change in Σ by 27°. This supports the suspected spin states deduced from the bond distances alone.

Based on a thermal expansion coefficient calculated from the contraction of the unit cell from 298 to 225K, the subsequent volume of the unit cell at 100K would be ~5099 Å<sup>3</sup>, whereas the actual volume is 5067.7(7) Å<sup>3</sup> due to the HS→LS transition. The overall contraction in volume from 296K-100K is 5.2%, shown graphically in Figure 3.2



along with the unit cell dimensions. In determining the types of structural changes that may be occurring during a spin transition, the anisotropic contraction of the unit cell is helpful. Upon cooling from 296K to 225K, the  $\beta$ -angle exhibits its largest change by increasing  $0.210(3)^\circ$ . Between 225K and 175K, where Fe1 exhibits a SCO, of any one dimension, axis a contracts the most by  $2.13(3)\%$ . In the same temperature range, a slight contraction along the b axis is mirrored by the necessary expansion along the c axis. Cooling from 175K to 100K, where Fe2 converts to LS, exhibits the most dramatic decrease of the b axis by  $0.504(1)\text{\AA}$  ( $2.62\%$ ) and corresponding increase in the c axis by  $0.383(3)\text{\AA}$ .

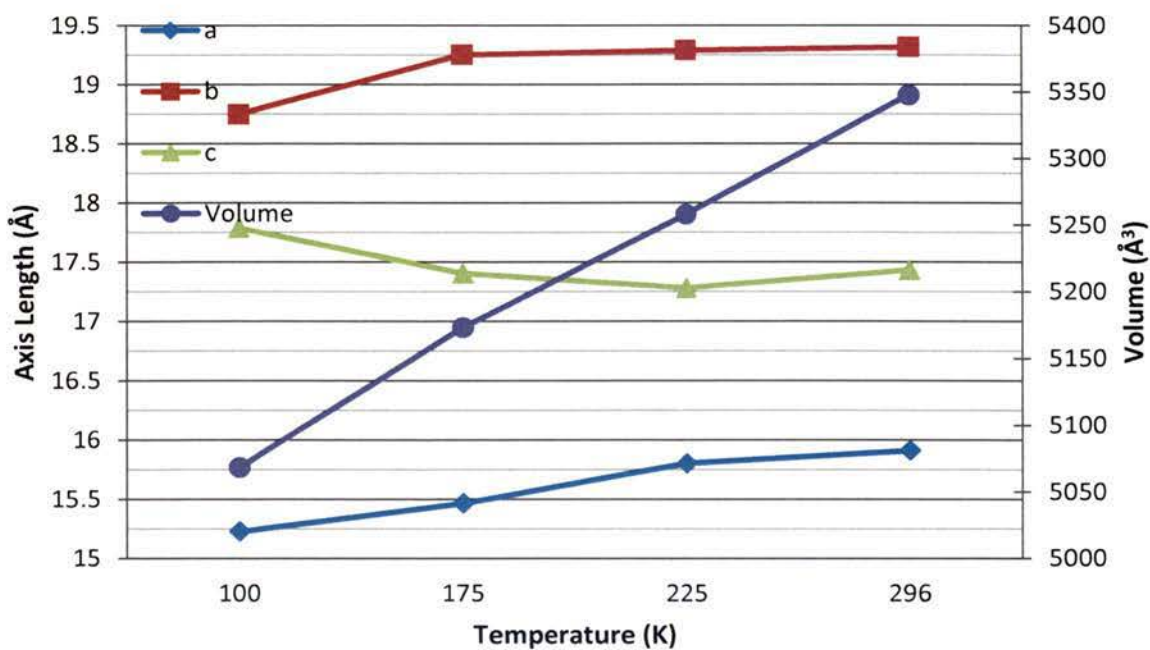


**Figure 3.2.** Unit cell dimensions and volume of  $[\text{Fe}(\text{salpm})_2]\text{BF}_4 \cdot 0.5\text{EtOH}$ .

More than just the intramolecular changes occur in SCO compounds, the intermolecular interactions affecting the cooperativity and thereby the characteristic features of a spin transition, are also dramatically important. The environment around each iron site shows considerable differences compared to the other. Centered on an inversion center, the planar salpm ligand of Fe1 stacks with another ligand from Fe1 to form a pair showing the shortest distance between two Fe1 sites to be 6.635Å at 100K. Fe2 also forms a pair with itself at a distance of 7.248Å at 100K.

It is apparent from the coordination environments that each iron site's SCO character is independent of the other, perhaps precluded by an absence of long range interactions. In fact, a purposeful addition of a methoxy group to the salpm ligand caused such an improved cooperativity in the system that both iron sites within the crystal undergo a concurrent spin transition [40]. For  $[\text{Fe}(\text{salpm})_2]\text{BF}_4 \cdot 0.5\text{EtOH}$ , long-range interactions between like iron sites (Fe1-Fe1 pairs) are interrupted by the alternate iron sites, Fe2-Fe2 pairs. Both Fe1 and Fe2 pairs are bridged by both  $\text{BF}_4^-$  anions, but each in a different manner. Fe2 pairs share short contacts with the B1 anion and also the B2 anion in between each Fe2 pairs. The Fe1 pairs bridge through the B2 anion while the B1 anion interacts with the benzene ends of the ligands within an Fe1 pair. The solvent ethanol is closely associated with B1 but still enjoys rotational and some translational freedom around the special positions.

A few more packing characteristics are necessary to note. The Fe1 complex is arranged such that all the  $\text{N}_{\text{im}}\text{-Fe1}\text{-N}_{\text{im}}$  axes of each complex is aligned within 172-180° of each other and parallel with the a-c, [101], plane and thus so are the ligands. Half the  $\text{N}_{\text{im}}\text{-Fe2}\text{-N}_{\text{im}}$  axes are rotated  $\sim 128^\circ$  with respect to each other while the other half are

aligned  $180^\circ$  to each other. This packing difference between Fe1 and Fe2 might suggest that along the most compressible imine bond axis direction, the periphery of the ligands enjoy more space, as the ligand planes overlap, in which to compensate for a change in the coordination geometry. This relationship is supported by the greater decrease of unit cell length,  $a$ , during the SCO of Fe1, attributed to the fact that the  $N_{im}$ -Fe1- $N_{im}$  axis most closely follows that unit cell edge.

As the temperature decreases from 296K, the thermal contraction exhibits a closer Fe1-Fe2 distance. In the range 225-175K, Fe1 transitions to LS, distorts and contracts its coordination sphere and the distance between Fe1 and Fe2 decreases more. From 175-100K, Fe2 transitions to LS and a further decrease would be expected for this direction, however, the distance increases suggesting prohibition by the sterics of the ligand. The Fe1-Fe1 and Fe2-Fe2 distances increase as temperature decreases and as expected increase more sharply during their respective SCO events. Decrease in the distances between all the molecules in general are seen with the decrease in temperature; i.e. the distance between the  $BF_4^-$  anions and the distances from each iron complex to the  $BF_4^-$  anions.

X-ray crystallographic measurements show the average positions of the atoms over the entire structure. Therefore, the spin state, as it is communicated through the bond lengths and distortions, of each crystallographically unique iron is an average of the spin states of each individual iron of that type within the crystal. An iron site with 90% HS and 10% LS would show the bond lengths in the range of HS iron. It is not, however, impossible to get a clue to the purity of the spin state from the structure. Pseudo-octahedral iron(III) complexes have shown a 0.12-0.15Å difference in the average Fe-L

bond lengths between pure HS and pure LS forms [91-93]. For comparison, the average bond distance change for SCO Fe(II) complexes is 0.18Å [2]. The difference between the overall averages,  $\Delta R[\text{FeO}_2\text{N}_4]$ , for  $[\text{Fe}(\text{salpm})_2]\text{BF}_4 \cdot 0.5\text{EtOH}$  lies below that range for the two iron sites at every temperature (Table 3.5). The values of  $\Delta R$  suggest that at 296K, both iron sites, Fe1 and Fe2, are 100% high spin and very nearly at 225K. At 175K, where the bond lengths for Fe1 are in the LS range and Fe2 bond lengths are in the HS range, a  $\Delta R$  value of 0.09 indicates that neither iron site is purely HS or LS. A  $\Delta R = 0.02$  at 100K, indicates that while on average, both iron sites are LS, there is still a portion of HS remaining. The values for the perchlorate complex are included for comparison. As described [3] the  $[\text{Fe}(\text{salpm})_2]\text{ClO}_4 \cdot 0.5\text{EtOH}$  complex does exhibit pure HS and LS at 100K corresponding to the magnetic  $T_C(\text{S}2)$  temperature.

**Table 3.5.** Difference between the average Fe-L bond lengths. Both iron sites averaged at each temperature.

	$\Delta R([\text{FeO}_2\text{N}_4]) (\text{Å})$	
	$[\text{Fe}(\text{salpm})_2]\text{BF}_4 \cdot 0.5\text{EtOH}$	$[\text{Fe}(\text{salpm})_2]\text{ClO}_4 \cdot 0.5\text{EtOH}$
100K	0.02	0.12
150K	--	0.10
175K	0.09	--
225K	0.01	--
294K	--	0.00
296K	0.00	--

### 3.5. SUMMARY/CONCLUSION

Since its first use to study the structural changes in the SCO compound, x-ray crystallography has been a valuable, additional technique to inspect the geometrical relationships exhibited by these compounds. The structure of  $[\text{Fe}(\text{salpm})_2]\text{BF}_4 \cdot 0.5\text{EtOH}$ , a suspected SCO material, was determined and compared at 4 different temperatures.

The data manipulation and refinement proceeded differently for each temperature due to a change in the thermal motion of the atoms and quality of the reflection data collected. Due to such, different methods (restraints, constrains, SQUEEZE) of treating the disorder and anisotropic nature of each structure were used. Convergence of the overall model with the observed structure factors resulted in R1 values of 0.047, 0.054, 0.051, and 0.058, respectively, for 100, 175, 225 and 296K

$[\text{Fe}(\text{salpm})_2]\text{BF}_4 \cdot 0.5\text{EtOH}$  is isostructural with its precedent  $[\text{Fe}(\text{salpm})_2]\text{ClO}_4 \cdot 0.5\text{EtOH}$ , crystallizes with the same molecular packing in the  $P2_1/n$  space group and exhibits two crystallographic unique iron atoms, Fe1 and Fe2. Structures of all three combinations of spin, HS:HS, HS:LS, LS:LS, were collected. From the x-ray crystal structures alone, it is possible to infer the following magnetic characteristics of  $[\text{Fe}(\text{salpm})_2]\text{BF}_4 \cdot 0.5\text{EtOH}$ .  $[\text{Fe}(\text{salpm})_2]\text{BF}_4 \cdot 0.5\text{EtOH}$  does undergo a two-stepped spin transition, but at higher temperatures than the  $\text{ClO}_4$  analog. The changes in the coordination bond lengths and angles indicate that the first SCO of Fe1 occurs between 225K and 175K, followed by the SCO transition of Fe2 between 175K and 100K. The change in the overall Fe-L bond lengths indicate that the HS:LS structure at 175K is a structural average of impure Fe sites, i.e. not having the 100%HS:100%LS ratio. The packing of the complex precludes any strong long-range interactions and therefore weak

cooperativity is expected and thereby a gradual spin transition. The Fe1 cations align throughout the crystal along their most SCO compressible  $N_{im}$ -Fe1- $N_{im}$  axis, whereas only half of the Fe2 cations align in this same direction. The bridging of Fe1 and Fe2 by solvent and anions also differs, but no strong interactions (significantly within VDW radii) are present.

## 4. APPLIED X-RAY STRUCTURE ELUCIDATION

### 4.1. INTRODUCTION

Given today's automation extent and sophisticated hardware, for many users the crystal structure determination is akin to casting bait into the water and either pulling out a fish or an empty hook. Not all data collected from crystals is of high enough quality for the default protocols of a computer to solve easily, but the solutions are frequently a small step away for the informed user, saving the expense of time and money. The practical skills necessary to address not-so-well-behaved data sets include a greater understanding of symmetry relationships and the data collection process.

### 4.2. ABSOLUTE STRUCTURE

**4.2.1. X-ray Dispersion.** As stated in Section 1, all diffraction patterns are inherently centrosymmetric and obey Friedel's law,  $I_{hkl} = I_{\bar{h}\bar{k}\bar{l}}$ . The absolute configuration of a molecule is hidden in X-ray data save for the observation that the absorption coefficient of an atom has large deviations at certain wavelengths of radiation. Therefore, when the wavelength is near the absorption edge of an element, the energy is sufficient to excite a core electron to a higher state or eject it completely. When the electron relaxes back to the core state it will emit an X-ray that has an equal probability for emission in any direction, therefore, the intensity is not a function of  $\theta$ . Absorption only occurs at typical X-ray wavelengths for atoms heavier than sulfur. The energy required to excite the electrons of C, N and O are out of the X-ray range[94]. If an atom absorbs some of the radiation, it results in a phase change of the X-rays scattered by that

atom relative to the X-rays scattered by other atoms in the structure[95 p141]. The phase change effect is synonymous to changing the path length of the radiation through the crystal. A change in the effective path lengths causes a breakdown of Friedel's law for non-centrosymmetric structures, as the intensities of the reflection  $I_{hkl}$  is not equal to  $I_{\bar{h}\bar{k}\bar{l}}$ . This effect, known as X-ray or anomalous dispersion, is small comprising only about 1-3% of the measured intensity[94]. It is possible to calculate the expected differences between  $F(hkl)^2$  and  $F(\bar{h}\bar{k}\bar{l})^2$  for a given configuration and thus correlate the observed difference between these and the configuration used to compute them[95 p143]. In other words if all the atoms at  $x,y,z$  are inverted to  $-x,-y,-z$  and the resulting  $I_{hkl}$  and  $I_{\bar{h}\bar{k}\bar{l}}$  agrees more with the observed  $I_{hkl}$  and  $I_{\bar{h}\bar{k}\bar{l}}$ , then the inverted structure is more likely the correct one. Because the anomalous scattering does not fall off with theta but the normal scattering does, the high angle reflections will have the biggest changes when anomalous scattering is included.

**4.2.2. Absolute Structure Parameters.** The most common absolute structure parameter is known as the Flack parameter,  $x$  [96]. It is added to the refinement, calculated from the final structure factors and is the fractional contribution of the inverted component of a racemic twin (*vide infra*). When this fraction is close to zero, the absolute structure is correct and when it is closer to 1.0, the structure should be inverted. Other values generally mean little or suggest true racemic twinning. The estimated standard deviation (esd) for  $x$  is extremely important as a large value (e.g. 0.6) indicates that the Flack parameter is inconclusive. The Flack parameter gives a quantitative indication of the absolute configuration, however it is correlated with other parameters when not enough Friedel pair data is available, affecting its validity[97].



Another approach absolute structure parameter frequently compared to the Flack parameter was developed by Rob Hooft et al. [98] as the Hooft parameter,  $y$ . This statistical method calculates the probability that the difference between the observed intensities of a Friedel pair of reflections will occur for each enantiomeric configuration. The probability ratios for each pair are added together for an overall structure probability ratio[99]. The Hooft parameter requires good coverage of Friedel pairs, but does not add any parameters to the refinement and typically has lower error than the Flack parameter.

**4.2.3. Example: 5,6-Dihydro-1,10-Phenanthroline Compounds.** Aromatic 1,10-phenanthroline compounds can be functionalized with an epoxide in the 5,6 position and then opened via a nucleophile to produce one or two stereogenic centers. For the projected research of some 5,6-dihydro-1,10-phenanthrolines, it was important to characterize conclusively the absolute configuration of carbons 5 and 6 after reaction with vinyl acetate and a lipase enzyme PSCI [4]. X-ray crystal diffraction provided one method for the confirmation.

Initially, only single crystals of the pure organic enantiomers could be formed. The X-ray structure was solved for the compound 5,6-Dihydro-5,6-acetoxy-1,10-phenanthroline(DAP). The crystal was routinely solved in  $P2_1$ ,  $Z=4$ ,  $a=7.2608(4)$ ,  $b=10.0928(5)$ ,  $c=19.9871(10)$ ,  $\beta=99.474(3)$  with a final  $R_1 = 0.0426$ ,  $S=0.926$ . Space group  $P2_1$  is a chiral space group and did contain only the diaxial enantiomer. The Flack parameter refined to a value of  $0.4(7)$ . The uncertainty is certainly too high to be a reliable measure. Thereby, a similarly synthesized compound, 5-hydroxy-6-acetoxy-1,10-phenanthroline (HAP) was reacted a variety of metals only to produce single crystals from reaction with  $\text{Cu}(\text{SO}_3\text{CF}_3)_2$ . The Cu K absorption edge is at

8.978KeV (1.38Å) which would work well for dispersion effects from Cu radiation, however, Mo radiation was used for the sample measurement, which also should give a large enough separation of anomalous scattering for the enantiomes. At 0.71703Å, Cu absorbs many times less than at 1.38 KeV. Still, the coordination compound  $[\text{Cu}(\text{HAP})_2 \text{CNCH}_3]\text{CF}_3\text{SO}_3$ , was solved in C2,  $a=19.3707(9)$ ,  $b=8.9932(4)$ ,  $c=9.5721(4)$ ,  $\beta=97.709(3)^\circ$ ,  $R_1=0.0401$ ,  $S=0.939$  (Figure 4.1). The Flack parameter refined to a value of 0.013(13) indicated a correct absolute configuration of the trans groups of 5S,6S. The Hooft parameter was also calculated,  $y=0.054(6)$ , and confirmed the configuration with an excellent esd. Even though the Friedel coverage was low, 94%, the average ratio (0.917) is very close to 1.00 and leaves little doubt that the absolute structure is correct.

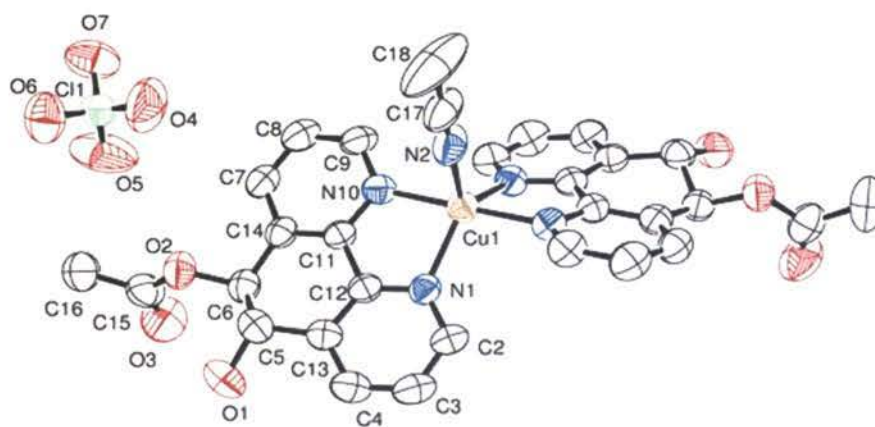


**Figure 4.1.** Structure of  $[\text{Cu}(\text{HAP})_2 \text{CNCH}_3]\text{CF}_3\text{SO}_3$ . Hydrogens removed. Thermal ellipsoids at 50%.

### 4.3. TWINNING

**4.3.1. Types and Indications.** The classic definition of crystal twins was given by Giacovazzo; "Twins are regular aggregates consisting of crystals of the same species joined together in some definite mutual orientation" [100]. Twinned crystals are described using a twin law to relate the orientations of the 2 or more component crystals and a ratio of each component, sometimes called domains. Twinning occurs when the unit cells of each twin component relate by a metric symmetry element (mirror, glide etc.) that does not coincide with the contents of the unit cell or the symmetry implied by the space group. When two different orientations of a crystal are placed in an X-ray beam, the patterns of each domain are overlapped resulting in a diffraction image of higher symmetry than the expected Laue symmetry of an un-twinned crystal. The diffraction intensity distribution also becomes more even as reflections of one domain are combined with reflections of the other domain. Figure 4.2 shows diffraction patterns of two orientations of an identical crystals separately and when combined.

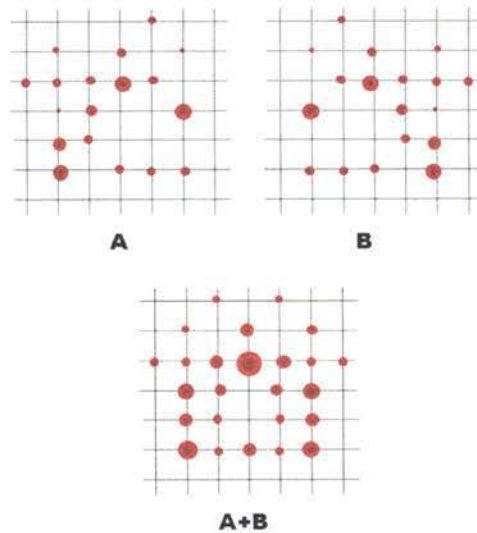


**Figure 4.2.** Example diffraction patterns of a twinned crystal. Two orientations (A and B) related by a vertical mirror are shown and then combined as a twinned crystal (A+B).

Twinned crystals can be classified into four different types. If the lattices of the domains completely coincide, the twinning is merohedral. The twin operator is a symmetry operation of the crystal system but not of the point group/Laue group of the crystal. When the twin operator is an inversion center, it is often called a racemic twin where the crystal is made of cells that are enantiomorphs of each other. Merohedral twinning is possible only for trigonal, tetragonal, hexagonal and cubic crystal systems [101]. For example, in an orthorhombic crystal where  $a$  and  $b$  are about equal the axes may exchange orientations and make the crystal appear tetragonal. Pseudo-merohedral twins also have coincident lattices, but the twin operator, which relates the domains, belongs to a higher crystal system than the true system. For example, when a monoclinic structure has  $\beta \sim 90^\circ$ , the overall structure will appear orthorhombic. All merohedral twins have coincident lattices and in the previous cases, both domains of the crystal

contribute to all the reflections. However, in reticular merohedral twins, each reflection may contain contributions from one domain, the other domain, or both[102]. The remainder of twins are described as non-merohedral, where the lattices do not necessarily coincide and only some of the reflections will have contributions from both twin domains. The twin operator is arbitrary and does not belong to the crystal system or metric symmetry. Non-merohedral twins often show split, close or partially overlapping reflections which must be identified and separated according to the correct twin domain. This requires identification of different orientation matrices for integration and subsequent data workup[103, 104]].

Often the presence of twinning is not apparent by visual inspection of the crystal or preliminary diffraction images. Also, the symptoms present in the data work-up process can be very subtle and therefore can sometimes remain hidden until the later stages of structure refinement. The common warning signs of twinning are listed in Table 4.1. One, but usually more than one indication is evident if twinning is present, so it is good measure to check the X-ray data for each.

**Table 4.1.** Common warning signs for twinning [102].

<ul style="list-style-type: none"> <li>-- The metric symmetry is higher than the Laue symmetry.</li> <li>-- The <math>R_{\text{int}}</math> value for the higher symmetry Laue group is only slightly higher than for the lower symmetry Laue group.</li> <li>-- The <math> E^2-1 </math> value is lower than expected.</li> <li>-- The space group appears to be trigonal or hexagonal.</li> <li>-- The systematic absences are inconsistent with any space group.</li> <li>-- No solution can be found and refinement gets stuck at high R-values.</li> </ul>
<p><u>Specifically for non-merohedral twins</u></p> <ul style="list-style-type: none"> <li>-- There appear to be one or more unusually long axes, but also many absent reflections.</li> <li>-- There is difficulty finding and refining the unit cell.</li> <li>-- <math>K = \text{mean}(F_o^2)/\text{mean}(F_c^2)</math> is systematically high for the reflections with low intensity.</li> <li>-- For all the ‘most disagreeable’ reflections, <math>F_o \gg F_c</math></li> </ul>

**4.3.2. Tools and Methods.** The practice of recognizing a twinned crystal and then adjusting the data is not very straight-forward as each situation can be drastically different. In some cases, as in the SHEXL program, a warning message will appear in the least squares output during refinement. However, once twinning is suspected, the first task is to identify the twin operator that relates the different domains of the twin and takes on the form of a 3x3 matrix that transforms the hkl indices from one form to another. It is beneficial to look at the unit cell and see if common twinning relationships could exist, such as exchange of two cell lengths that are almost equal. However, the automated routines such as Rotax[105] and TwinRotMatanalyze the reflection list by searching for the largest values of  $(|F_o^2| - |F_c^2|)/u(|F_o^2|)$ [105]. The indices of these reflections are then

transformed by rotations or roto-inversions about different possible lattice directions.

The matrix that transforms the indices of the poorly fitting data to integers are the possible twin laws. Twin laws with figures of merit closer to zero are more likely and should be tried first.

Once the twin law is known, SHELXL provides two easy instructions to facilitate refinement merohedral and pseudo-merohedral twins where the lattices of the twin domains are superimposable. The TWIN instruction following by the 9 matrix elements of the twin law and the number of twin components, allows for generation of sets of indices for the twin components from the input indices. The batch scale factor, BASF instruction is needed also to refine the fractional contributions of the twin components. The simple operation of inversion about the origin for a racemic twin with 2 domains and would be given as TWIN 1 0 0 0 1 0 0 0 1 2.

Non-merohedral twinning can also be detected by TwinRotMat, but requires complete reanalysis of the data by separating reflections from the twin domains, determining the corresponding orientation matrix and unit cell for each. The program Cell Now[106] has been commonly used in the past and searches for sets of reflection planes with the maximum number of intersecting reflections. It then uses least squares to refine the real-space vectors, downweights reflections that do not fit well and concentrates the refinement on the better-fitting reflections which should come from the same twin domain [103]. More and more common again is the graphical determination of twin domains using reciprocal lattice viewers like RLATT where inconsistent reflections arrays can be individually chosen and designated to other domains.

**4.3.3. Example: Hydrazinecarbothioamide Nickel Complex.** An interesting structure of a square planar nickel(II) complex of hydrazinecarbothioamide analog and 4,4'-bipyridine was solved in the Cc space group with an  $R_1=0.0616$ ,  $S=0.958$ . The unit cell has the dimensions of  $18.213(8)\text{\AA}$ ,  $45.930(2)\text{\AA}$ ,  $c=11.8265(5)\text{\AA}$ ,  $\beta=114.44^\circ$ . Refinement proceeded adequately until anisotropic refinement of the carbon atoms within the structure. The results displayed a warning "possible racemic twin or wrong absolute structure-- try twin refinement." 71 of the carbon atoms became non-positive definite (NPD) indicating a major problem with the model. Also the atom structure seemed to contain inversion, but 4 molecules of DMSO were also in the lattice. Sometimes disordered solvent molecules will reduce the expected symmetry of the unit cell. So, exploration of the data for any of the warning signs for twinning found that axis b may be considered long, the combined figure of merit for the suggested space groups from XPREP were very high at 13.05 for C2/c and 32.47 for C2. C2/c was already tried and failed to produce even distinguishable locations for the sulfur atoms. The Flack parameter was inconclusive at a value of 0.36(4). So, exploration into possible twinning was conducted first.

Because it is so facile, a basic racemic twin law and BASF value were used for refinement. The model did not improve. Next the use of Rotax produced a file output where the figure of merit for both  $180^\circ$  rotations was 0.000, indicating that the rotations were simply part of the crystal symmetry and not a twin. Just in case, the Platon executable, TwinRotMat confirmed the lack of twinning by not detecting any twin law.

Having eliminated simple twinning, the absolute structure must be wrong. The space group was checked by using the ADDSYM function with the PLATON toolbox.



Here again, no higher symmetry was detected. Inspection of the systematic absences seemed like the next logical step to determine if there was any missed symmetry. It was realized upon looking at the values of the most disagreeable reflections, that they all had even integer  $h$  and  $k$  values. The systematic absences for C-centering obey the expression  $h+k = 2n+1$ , odd. It is unusual that no systematic reflections for the C-centering, disagree. In fact, the only centering possible is primitive having no restriction on the systematic absences.

This meant that the unit cell dimensions were probably wrong and needed to be recalculated. By decreasing the tolerances for acceptable reflections used in determination of the unit cell, the monoclinic option dominated and a new unit cell was calculated. Reintegration and space group determination using XPREP yielded only one option of  $P2_1/n$  with a CFOM = 2.01 (Figure 4.3). The rest of the structure solution was routine.

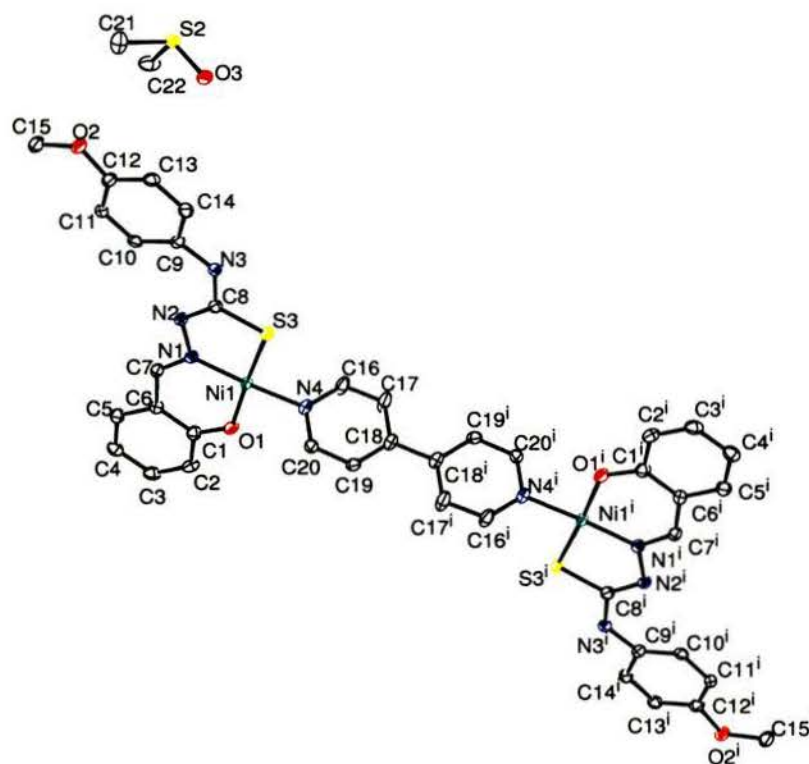


**Figure 4.3.** ORTEP diagram of  $\text{Ni}_2\text{L}_2(\text{py})\cdot\text{DMSO}$ . 50% displacement parameters. Hydrogens removed for clarity. Symmetry code: (i)  $-1-x, -y, -1-z$ .

#### 4.4. SYMMETRY AMBIGUITY

The same symmetry can be described in different ways with respect to orientation and unit cell definition. Therefore, while a completely correct solution can be detailed using other particulars, it is beneficial to others to describe structures using standard protocols listed in the International Tables of Crystallography. This is the case with the structure of a copper hydrazone complex  $\text{Cu}(\text{C}_{26}\text{H}_{20}\text{N}_6\text{O}_4)_2$  solved in the orthorhombic space group  $\text{Aba2}$ . Only 629 of the 592,938 structures reported in the Cambridge Structural Database (CSD) occur in this space group[107]. Considering the standard setting of  $\text{Aba2}$ , the space group symmetry elements include a b-glide

perpendicular to the a axis, an a-glide perpendicular to the b-axis and a 2-fold rotation parallel to the c axis.

Confusion can easily be created when trying to describe different motifs and long range bonding interactions with the context of the defined unit cell. The copper atom of the complex was found at the special position coordinates (1.0, 0.5, 0.4197). Special positions lie on symmetry elements of the space group and atoms or molecules on those positions exhibit the exact point symmetry of the symmetry element. For example, if an atom lies on an inversion center at the origin, inverting the structure will not change the position of that atom while the other atoms of the structure will invert from  $x,y,z$  to  $-x,-y,-z$ . In our present example, the copper atom is on a 2-fold rotation axis and bonded to half of the molecule to form the asymmetric unit. Execution of the 2-fold rotation will generate the other half of the molecule. The overall geographic position of the second half of the molecule is at the position  $(2-x,1-y,z)$  relative to the complete crystal lattice.

When the relationship between the two ligands is determined using a geometry software package, PLATON, it is found to be  $(-x, 1-y, z)$ . Both relationships,  $(2-x, 1-y, z)$  and  $(-x, 1-y, z)$  that describe the relationship between both ligands, are correct, but only with respect to different molecules within the unit cell. PLATON shifted the molecule to  $(0, 0.5, 0.4197)$ , on the other side of the unit cell and defined the opposite ligand at the coordinates  $(x,y,z)$ . Then when the 2-fold axis is applied, it generates the ligand at  $(-x,1-y,z)$ . However to conform as much as possible to the standard setting, the copper atom should be placed on the special position  $(0,0,z)$ . This further requires a translation of  $-0.5$  in  $y$  and  $0.5$  in  $z$  so that the copper atom would lie on the 2-fold rotation axis that intersects the origin. Figure 4.4 shows the different positions where the

Cu atom originally defined at (1,0.5,0.4197) is translated to (0,0.5,0.4197) by the PLATON program and translated again to (0,0,0.9179) to conform to the special position (0,0,z).

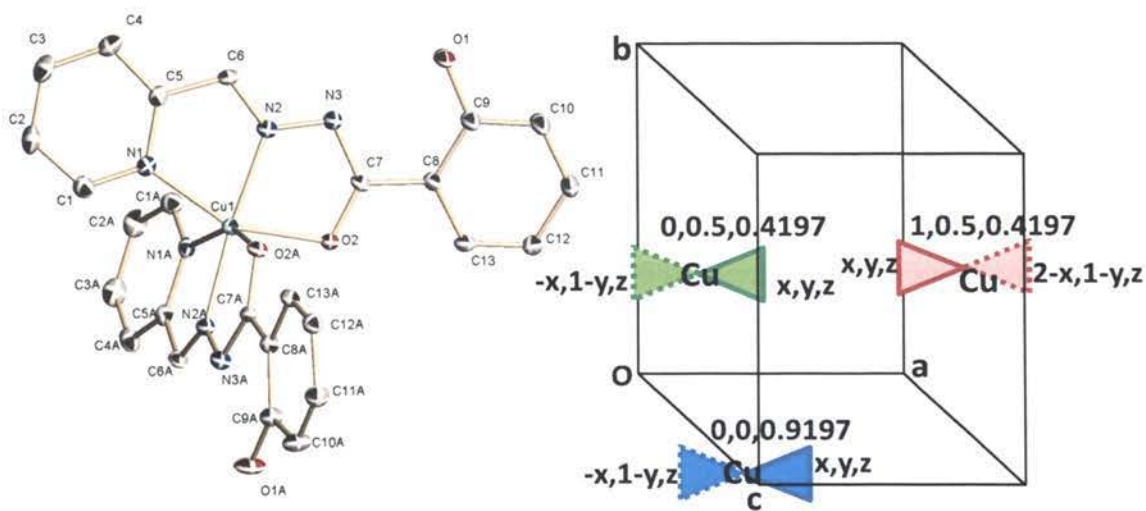


**Figure 4.4.** ORTEP diagram  $\text{Cu}(\text{C}_{26}\text{H}_{20}\text{N}_6\text{O}_4)_2$ . 50% ellipsoids, hydrogens removed for clarity and schematic of the orthorhombic unit cell showing translations to place the Cu on the standard special position (0,0,z) as described in the text.

## 5. NICKEL SALICYLALDIMINES

### 5.1. INTRODUCTION

The study of small metal compounds remains an active area of research due to the spectroscopic, structural and magnetic properties unique to these clusters. Our interest resides in the nickel salicylaldimine (sal) clusters of two or three metal centers. In a previous article [9], binuclear complexes of the formula,  $[\text{Ni}(\text{iprsal})\text{NO}_3\text{R}]_2$  where iprsal = N-isopropylsalicylaldimine and R = solvent ethanol or DMF, were synthesized and magnetically characterized. It was determined that a ferromagnetic interaction was present when the sal ligands were coordinated  $90^\circ$  to the  $\text{Ni}_2\text{O}_2$  bridge and antiferromagnetic when coordinated parallel. The identity of the solvent used to complete an  $\text{O}_h$  paramagnetic, coordination sphere also determined the relative orientation of the sal ligands and whether hydrogen bonding would exist between the dinickel units. During the formation of these binuclear nickel complexes, the formation of a trinuclear product was also detected. It was suggested that the steric constraints of the N-imine substituent on salicylaldehyde dictated the trinuclear formation; however, no further results concerning the formation or characterization of the trinuclear product were published. The following research was initiated in order to determine the synthetic conditions necessary to produce the trinuclear product and the steric restrictions that govern its formation by modifying the N-imine substituents. In addition, any structural conditions that may affect the magnetic interactions between the nickel atoms, were also explored.

Besides the fundamental interest in the properties of the Ni trinuclear complexes, there is potential for a trinuclear core motif made of three interacting paramagnetic atoms with simple Schiff base ligands to produce interesting magnetic properties, especially in the realm of single-molecule magnets (SMMs). It has been shown that bridging angles in homonuclear compounds close to  $90^\circ$  encourages orthogonality of the magnetic orbitals and a resultant non-zero spin ground state required for SMMs [108]. Within the array of Ni SMMs [109, 110], bridging angles close to  $90^\circ$  [111, 112] are not uncommon and phenoxo-bridging ligands have also been used successfully to transmit magnetic interactions in heteronuclear SMMs as in the case of 3d-Gd complexes (3d =  $\text{Cu}^{2+}$ ,  $\text{Ni}^{2+}$ ,  $\text{Co}^{2+}$ ,  $\text{Fe}^{2+}$ , VO) [113].

Trinuclear and larger SMMs [114-116] continue to be studied as a way to develop multi-functional materials. By keeping to clusters of a few metal centers many of the problems involved with study of large systems, such as dilution of magnetic anisotropy, crystallization solvent effects, complicated nuclear quantum dynamics and lack of synthetic control, are avoided [117]. A triangular structure can produce SMMs along with other unique magnetic properties as seen in a  $[\text{Dy}^{\text{III}}_3 (\mu\text{-OH})_2 (\text{o-vanillin})_3 \text{Cl}(\text{H}_2\text{O})_5]^{5+}$  [118] and the  $[\text{Mn}^{\text{II}}_6 \text{O}_2 (\text{Rsao})_6 (\text{O}_2 \text{CR}')_2 (\text{solvent})_4]$  family, a combination of two triangular units [119]. This  $\text{Mn}^{\text{II}}$  family of complexes represents one of the very few studies that investigates the ligand constituents' effect on magnetic properties [120].

## 5.2. MAGNETISM

The electronic structure of complexes is frequently studied by looking at the magnetic interactions of paramagnetic metals. Paramagnetism occurs when there are one or more unpaired electrons in a complex and is evident by the attraction of a sample to an external magnetic field. In contrast, diamagnetism, when all the electrons are paired, repels slightly an external magnetic field. Magnetic measurements are used to determine the number of unpaired spins in a complex and determine the ground state configuration [121] by initially measuring the magnetic susceptibility ( $\chi$ ). The magnetic susceptibility is the proportionality constant that relates the magnetic moment ( $\mu$ ) to the externally applied magnetic field. Equation 5.1 gives the most convenient spin-only formula:

$$\chi = \frac{N\beta\mu_{\text{eff}}^2}{3kT} \quad (5.1)$$

where  $N$  = Avogadro's constant,  $\beta$  = Bohr magneton,  $k$  = Boltzman's constant and  $\mu_{\text{eff}}$  is the effective magnetic moment. Thereby substitution of the above constants gives the equation for calculating the magnetic moment from the measured susceptibility:

$$\mu_{\text{eff}} = 2.828\sqrt{\chi T} \quad (5.2)$$

All paramagnetic compounds, however, have a small component of diamagnetism resulting from the paired electrons in the inner shells counteracting the overall attraction of the paramagnetic material in the external magnetic field. Thus, the measured paramagnetic susceptibility deviates from the true magnetic susceptibility by the diamagnetic affects of the paired electrons. The measured magnetic susceptibility requires correction by subtracting the susceptibility of the diamagnetic groups within the sample:

$$\chi_{corr.} = \chi_{obs.} - \sum \chi_L \quad (5.3)$$

The values of  $\chi_L$  are tabulated values for various bonding combinations usually found in ligands and known as Pascal's constants [122].

The calculated magnetic moment can be directly related to the quantum numbers used to describe the energy states of atoms, in this case, of the free atom or ion by the equation,

$$\mu_{S+L} = g \sqrt{S(S+1) + \frac{1}{4}L(L+1)} \quad (5.4)$$

where S = total spin angular momentum, L = total orbital angular momentum, and g = 2.00023 known as the gyromagnetic ratio [115]. For an atom that is part of a complex, the orbital angular momentum is normally heavily suppressed by the interaction with a non-spherical external field of a ligand, while the spin angular momentum is usually retained by any unpaired electrons to generate a spin-only paramagnetism:

$$\mu_S = g \sqrt{S(S+1)} \quad (5.5)$$

Specifically for A (or B) and E ground states, the moment will be close the spin-only value or at least fairly independent of temperature with a g-value that may deviate from 2.0 on slightly the low side or somewhat more on the high side depending on whether the d-shell is less or more than half-filled (e.g. in Ni<sup>II</sup> O<sub>h</sub> g may be around 2.2). In T ground states, the moment tends to be temperature dependent and doesn't conform to spin-only. Since S is the sum of the s for the unpaired electrons, the spin-only magnetic moment can be theoretically calculated for any given number of unpaired electrons, n, with

$$\mu_S = \sqrt{n(n+2)} \quad (5.6)$$



The spin-only formulas are usually sufficient to match the measured magnetic moment and determine the electronic configurations of 3d and some 4d configurations. However, for some complexes, such as  $[\text{Fe}(\text{CN})_6]^{3+}$ , the measured magnetic moment leads to ambiguity as it is between spin-only values for one and two unpaired electrons [121 p 479]. This is an example of a T ground state case,  ${}^2T_{2g}$ , and the Hamiltonian includes the coupling of the magnetic field with the electron spin moment  $s$  and with the orbital angular momentum  $l$ , as well as the spin-orbit coupling  $\lambda l.s$ . In such cases and cases of most 4d-5d complexes, the spin-only assumption breaks down and an orbital angular momentum becomes significant and must be considered.

Qualitatively,  $\chi$  is a measure of how easy it is to align electron spins within an applied magnetic field. The value of  $\chi$  is different for each sample and is commonly in units of  $\text{cm}^3/\text{mol}$ . The measured magnetic susceptibility of any substance can be compared to the theoretical susceptibility calculated from the Van Vleck equation. The Van Vleck equation uses the energy levels to calculate the susceptibility making three major assumptions; that there is no magnetic field dependence of the susceptibility, the energy of the  $i^{\text{th}}$  level of an atom can be expressed as a power series, and that the splitting of levels due to the 1<sup>st</sup> order Zeeman effect is small compared to  $kT$ .  $kT$  is the thermal energy available to the system according to a Boltzman distribution.  $E_i^0$  is the energy of the  $i^{\text{th}}$  level without an external magnetic field.  $E_i^{(1)}$  and  $E_i^{(2)}$  are the 1<sup>st</sup> and 2<sup>nd</sup> Zeeman coefficients. With  $N$  equal to Avogadro's number, the Van Vleck equation for susceptibility is

$$\chi = \frac{N \sum_i \left( (E_i^{(1)})^2 / kT - 2 E_i^{(2)} \right) \exp(E_i^0 / kT)}{\sum_i \left( \exp(E_i^0 / kT) \right)} \quad (5.7)$$

This equation can be simplified and applied in many different ways to calculate the expected variation of  $\chi$  with T. As the temperature changes, the thermal population of the energy levels will change. The magnitude of the energy gaps between the levels, particularly of the ground state, will dictate the occupation distribution of the atoms and thereby the magnetic properties of the material. Determination of the theoretical ground state energy levels of a material requires starting with the quantum numbers of individual electrons and applying ligand field theory. Nickel(II) is used in the following as the primary example for the determination.

**5.2.1. Mononuclear Complexes.** Nickel(II) has eight d electrons and depending on the ligand electronic field, can be found in the three major coordination geometries, square planer, tetrahedral and octahedral. A square planer ligand field has the effect of splitting the metal d orbital energies into the configuration shown in Figure 5.1 where the large difference between the  $d_{xy}$  and  $d_{x^2-y^2}$  orbitals is defined as  $\Delta_3$ . This large gap,

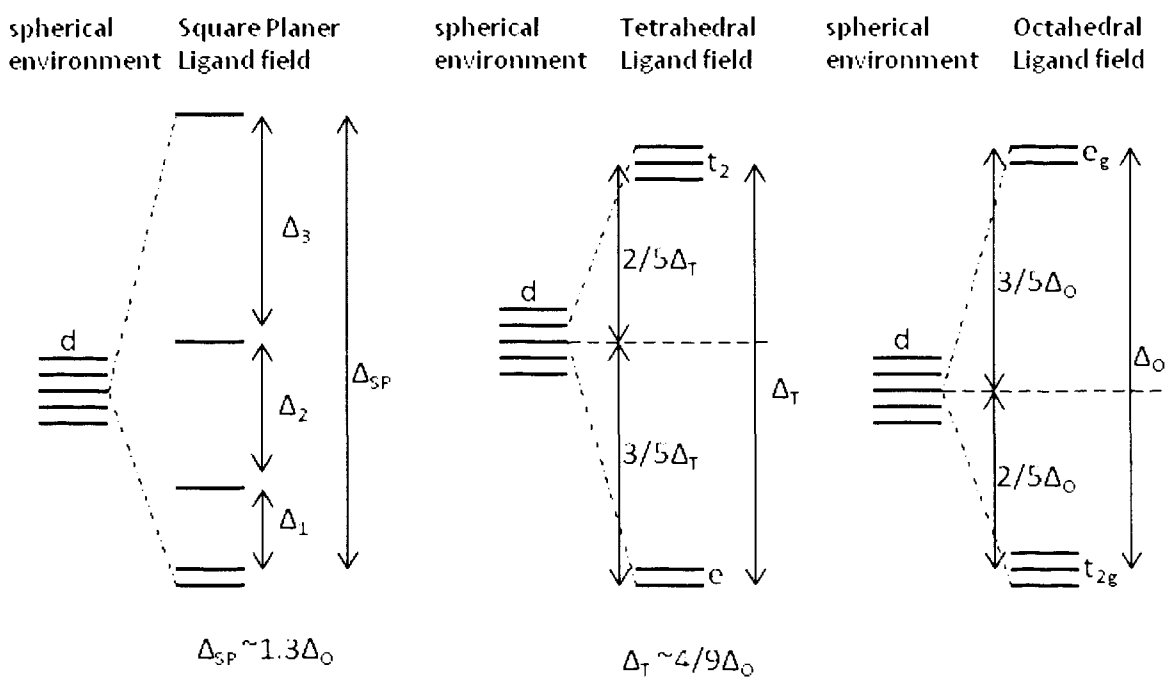


**Figure 5.1.** d orbital splitting in different ligand fields.

on the order of  $20\text{-}30000\text{ cm}^{-1}$  [123] is responsible for the stability and diamagnetic configuration of  $d^8$  complexes of  $\text{Ni}^{2+}$  and  $\text{Pt}^{2+}$ . Compared to tetrahedral, a square planer geometry requires greater steric interaction on the part of the ligands and thus a higher energy state if the ligands are bulky enough for steric effects to be significant. Charge repulsion of the ligands may also be a factor.  $\text{NiCl}_4^{2-}$  is a flattened tetrahedral but tetrahedral enough to be paramagnetic due to relatively small ligands, weak crystal field, and charge repulsion. On the other hand  $\text{Ni}(\text{CN})_4^{2-}$  is planar because of the small ligands and strong crystal field such that charge repulsion overwhelmed. However, with strong enough ligand fields, the crystal field stabilization energy of especially  $d^8$  configurations more than compensates for the steric constraints[121 p 481].

The tetrahedral ligand field produces splitting of the d orbitals such that the  $d_{xy}$ ,  $d_{yz}$  and  $d_{xz}$  orbitals directed somewhat more closely at the ligands are higher in energy than the  $d_{z^2}$  and  $d_{x^2-y^2}$  orbitals by an energy gap of  $\Delta_t$ . The value of  $\Delta_t$  is often of comparable or smaller magnitude than the pairing energy of the electrons, so when possible, high spin complexes result. For nickel(II), the ligand field stabilization energy is considerably lower for a tetrahedral ligand field compared to an octahedral field and there are relatively few tetrahedral Ni(II) complexes due to their lower stability. This is why tetrahedral nickel(II) complexes predominately occur with very weak-field ligands in which the steric constraints will not allow a square planer geometry. In a tetrahedral geometry, a  $d^8$  configuration yields two unpaired electrons, producing a paramagnetic complex.

An octahedral ligand field causes the d orbitals of the metal to split in energy such that the  $d_{z^2}$  and  $d_{x^2-y^2}$  orbitals directed at the ligands increase in energy and the  $d_{xy}$ ,  $d_{yz}$  and  $d_{xz}$  orbitals stabilize relative to a spherical field. Here the  $t_{2g}$  orbitals are lower than the  $e_g$  orbitals by an energy gap of  $\Delta_o$ ; the  $e_g$  orbitals are  $3/5\Delta_o$  above the energy in a spherical field and the  $t_{2g}$  are  $2/5\Delta_o$  below. Eight electrons in this configuration give a low spin, paramagnetic metal with two unpaired electrons and a ligand field stabilization energy of  $6/5\Delta_o$ .

Ligand field theory describes what happens to the d orbitals when the electrons interact with the electrons of a ligand. However, the d-orbitals are not truly degenerate in the absence of a ligand field. An electron within a metal interacts with other electrons within the metal causing differing possible energy states for the electrons. These

interactions can be described using different schemes such as Russel-Saunders coupling (a.k.a. LS coupling) and spin-orbit coupling.

LS coupling is the process of combining the electron angular momenta by first summing the spin angular momenta ( $m_s$ ) of each electron and then the orbital angular momenta ( $m_l$ ) of each electron and then combining the two resultants [121 p 489]. This type of coupling scheme is used to identify the terms, or collection of energy states, from quantum numbers. Then we apply Hund's rules, to determine which is the ground term. It is most applicable to the lighter 3d metals while heavier atoms are more influenced by spin-orbit coupling. The spectroscopic terms for the nickel ion with two unpaired electrons are  $^1S$ ,  $^1D$ ,  $^1G$ ,  $^3P$  and  $^3F$ .  $^3F$  is the ground state term as it has the highest multiplicity and the largest L-value.

LS coupling describes the vector sum of the electron spins  $S$  with the vector sum of orbital angular momenta  $L$  of the electrons in the same atom. Then the orbital angular momentum of one electron is related to the orbital angular momentum of the other electron. However, an additional interaction can heavily influence the energy states of a free ion and that is the interaction of the spin angular momentum of one electron with its own orbital angular momentum. This is known as spin-orbit coupling and requires the definition of a new quantum number,  $J$ , the total angular momentum for an atom where  $J=(L+S), (L+S-1)\dots|(L-S)|$ . Spin-orbit coupling strongly influences the terms of heavier atoms, and is commonly too small of an effect in the 3d elements compared to LS coupling or ligand field interactions and is thus neglected. However, for first-row transition metals, the spin-orbit coupling has important consequences for the magnetic properties [124 p 22] and affects a  $3d^n$  atom's deviation of the magnetic moment from the

spin-only value. Spin-orbit coupling causes the ground term of nickel,  ${}^3F$ , ( $L=3, S=1$ ) split further into 3 levels,  $J = 4, 3, 2$ . The  $d^8$  configuration has more than a 1/2-full subshell and therefore, according to Hund's third rule, the term with the highest  $J$ -value is the lowest in energy. For nickel that would be  ${}^3F_4$ . And if that wasn't enough, each energy term is further split when the atom is placed within an external magnetic field into  $2J+1$  terms. The overall splitting scheme for a  $d^8$  ion is shown in Figure 5.2. Of course, there are significant deviations of the energy term distribution depending on the atom.

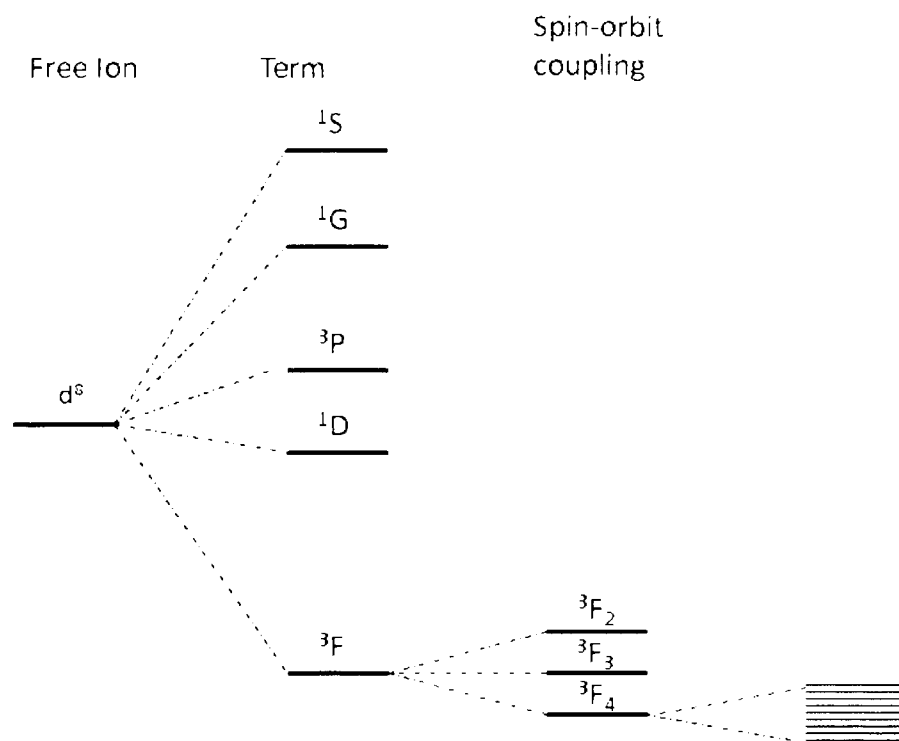


**Figure 5.2.** Splitting of energy terms of a  $d^8$  ion. Splitting as a result of electron-electron interactions.

When the free ion energy terms combine with the ligand energy levels, the magnitude of the different couplings, LS, spin-orbit and ligand-field, and their symmetry relative to each other determines the distribution of the energy levels. When the ligand field magnitude is larger than spin-orbit coupling, but smaller than LS coupling, it is said to be weak. In a weak ligand field, the ground state determined from the free ion, is split according to the symmetry of the ligand (e.g.  $O_h$ ,  $T_d$ ) to generate molecular energy terms, e.g.  ${}^3A_{2g}$ . When the ligand field magnitude is larger than spin-orbit and LS coupling, it is said to be strong. The result of a strong field ligand is that the ground term splitting can be expressed solely based on the ligand-field splitting parameters,  $\Delta_O$ ,  $\Delta_t$ . The two extremes of a weak field and a strong field are correlated in Orgel and Tanabe-Sugano diagrams. For  $Ni^{2+}$ , the  ${}^3F$  ground term would be split inversely, yielding  ${}^3T_1$  and  ${}^3A_{2g}$  molecular terms for tetrahedral and octahedral ligand-fields, respectively. Molecular terms are similar to free ion terms in the multiplicity, superscript, only. The rest of the symbol corresponds to the symmetry of the molecular term.

Once identification of the ground term is made, explanation of the magnetic behavior becomes clearer. The spin-only magnetic moment for 2 unpaired electrons present in both tetrahedral and octahedral nickel(II) is 2.8 B.M. (equation 5.5). However, the observed magnetic moment for tetrahedral nickel in  $(Et_4N)_2NiCl_4$  is 3.8 B.M at room temperature. Deviations like this are a result of spin-orbit coupling (along with small ligand field splitting) and can be predicted by the ground state term. If the ground state term is of T-symmetry and rotation of the orbital bearing an electron, converts into an identical, degenerate orbital which has a vacancy for the spin concerned, that electron displays orbital angular momentum[125]. When this is true, a magnetic field can force

the electron to circulate around the metal ion by using the low-lying orbitals and generate an orbital angular momentum and contribution to the total magnetic moment. 3d metal ions that have a ground term of A or E symmetry will not deviate as significantly from the spin-only magnetic moment [121, p 479].

**5.2.2. Binuclear Complexes.** A single paramagnetic metal of a complex surrounded by ligands is normally magnetically isolated from the metal of the neighboring complex. However, when paramagnetic atoms are close to each other, their electrons can interact and display cooperative magnetic characteristics. Normal paramagnetic substances have spins that partially align in a magnetic field and then as the thermal motion is reduced with temperature, more spins align and the magnetic susceptibility increases. Sometimes, due to the close nature of the paramagnetic centers, the unpaired electrons in nearby orbitals will interact strongly enough for entire domains of parallel spins to exist such that the magnetic moment will be much larger due to the spins adding together. This type of behavior is indicative of ferromagnetic substances. As long as the thermal motion of the electrons remains low enough, below the Curie temperature, the coupling of the spins is strong enough to remain in the absence of the magnetic field which first induced the alignment. Antiferromagnetism is another cooperative interaction that can occur with paramagnetic substances. As temperature decreases in a magnetic field, the spins align in an antiparallel arrangement, where the electron spins are alternating throughout the material. This alternating arrangement throughout an infinite array causes the magnetic moments of each atom to cancel and thereby produce a decrease in the magnetic susceptibility at the Neel temperature. Above



the Neel temperature, a normal paramagnetic increase of susceptibility with decreasing temperature is typical of antiferromagnetic materials.

Two metals, which are not bonded directly, can interact magnetically through the intervening diamagnetic atoms in what is known as superexchange interactions. In superexchange, the d orbital of the metal overlaps with the s or p orbitals of a bridging atom which overlaps the d orbital of the other metal. Exchange interactions between paramagnetic centers and their variation of  $\chi$  with T can be calculated using the vector coupling method with the spin-only Hamiltonian, assuming an isotropic magnetic interaction where the orbital magnetic moments are neglected, as in

$$H = -2 \sum_{ij} J_{ij} \hat{S}_i \cdot \hat{S}_j \quad (5.8)$$

where  $J_{ij}$  is the exchange coupling constant between the atoms i and j with spins  $\hat{S}_i$  and  $\hat{S}_j$ . When the spins are paired in the ground state,  $J_{ij}$  is negative (antiferromagnetic) and when parallel, positive (ferromagnetic). This Hamiltonian operates on the wavefunctions of spins to generate new states for the coupled system described by  $S_T$  where  $S_T$  has the values  $S_T = S_1+S_2, S_1+S_2-1, \dots, |S_1-S_2|$ . In a magnetic field the energy level,  $E(S_T)$  is split into  $2S_T+1$  levels separated by  $g\beta H$ . If  $g\beta H$  is small compared to  $kT$  in the temperature range of interest, all the energy levels are populated to an equal extent and the molar susceptibility equation takes the form,

$$\chi_M = \frac{Ng^2\beta^2}{3kT} \frac{\sum_{S_T} S_T(S_T+1)(2S_T+1) \exp\left(\frac{-E_{S_T}}{kT}\right)}{\sum_{S_T} (2S_T+1) \exp\left(\frac{E_{S_T}}{kT}\right)} \quad (5.9)$$

Which new state,  $S_T$ , is the ground state is determined by the sign of J. If J is positive,

the highest value of  $S_T$  is the ground state. If  $J$  is negative, the lowest value of  $S_T$  is the ground state.

For a nickel(II) binuclear complex with interacting spins  $S_1 = 1$  and  $S_2 = 1$ , the corresponding values of  $S_T$  are 2, 1, 0 with degeneracies of 5, 3, 1, respectively, which leads to splittings in a magnetic field of 5,3,1. The energy of the coupled states, calculated from the Hamiltonian (equation 5.8). Evaluation of equation 5.10 with all the

$$E(S_T) = -J_{12}[S_T(S_T+1) - S_1(S_1+1) - S_2(S_2+1)] \quad (5.10)$$

possible values of  $S_T$  yields the energy level scheme depicted in Figure 5.3. Substitution of the corresponding values of  $S_T$  and  $E(S_T)$  into equation 5.9 gives the theoretical molar

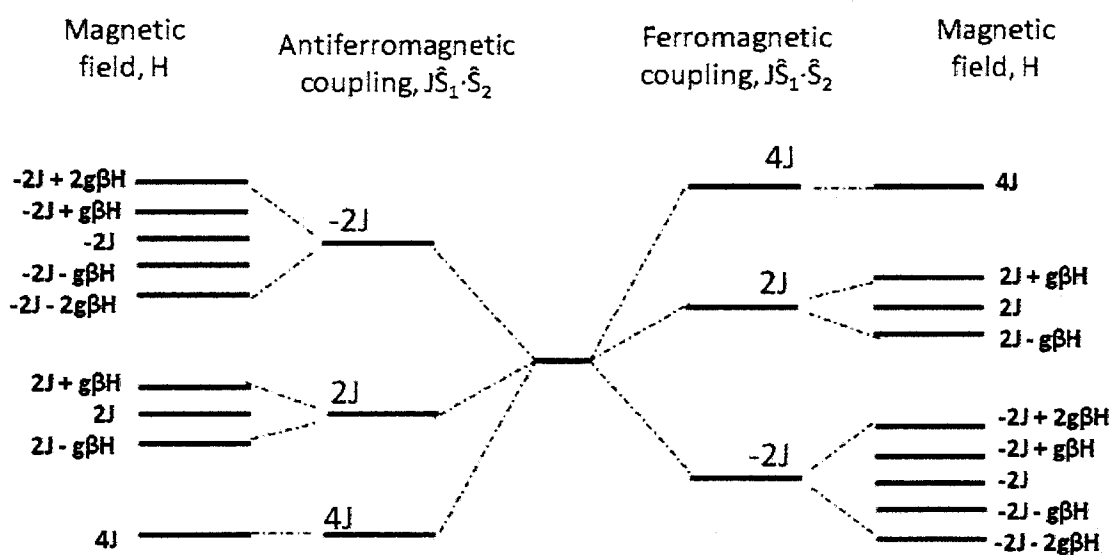


**Figure 5.3.** Energy level splitting of a  $S_1=S_2=1$  binuclear complex.

susceptibility for two interacting metals with  $S_1=S_2=1$  (e.g.  $Ni^{2+}$ ) in terms of the coupling constant,  $J$  :

$$\chi_M = \frac{Ng^2\beta^2}{3kT} \frac{6 \exp\left(\frac{-2J}{kT}\right) + 30 \exp\left(\frac{2J}{kT}\right)}{1 \exp\left(\frac{-4J}{kT}\right) + 3 \exp\left(\frac{-2J}{kT}\right) + 5 \exp\left(\frac{2J}{kT}\right)} \quad (5.11)$$

The value of J is experimentally calculated by fitting the measured susceptibility to the appropriate theoretical equation derived from equation 5.9.

**5.2.3. Trinuclear Complexes.** When three paramagnetic centers,  $S_1$ ,  $S_2$  and  $S_3$  are close enough to couple through overlapping orbitals, the Hamiltonian takes the form

$$H = -2J_{12}\widehat{S}_1 \cdot \widehat{S}_2 + -2J_{13}\widehat{S}_1 \cdot \widehat{S}_3 + -2J_{23}\widehat{S}_2 \cdot \widehat{S}_3 \quad (5.12)$$

such that the energy of the coupled states determined from this Hamiltonian is

$$E(S_T) = -J_{13}S_T(S_T+1) + S_{12}(S_{12}+1)[J_{13}-J_{12}] + S_{23}(S_{23}+1)[J_{13}-J_{23}] + J_{12}S_1(S_1+1) + S_2(S_2+1)[J_{12}+J_{23}-J_{13}] + J_{23}S_3(S_3+1) \quad (5.13)$$

The values of  $S_T = S_{12} + S_3, S_{12}+S_3-1, S_{12}+S_3-2, \dots, |S_{12}-S_3|$  and the values of  $S_{12} = S_1+S_2, S_1+S_2-1, \dots, |S_1-S_2|$ . Likewise substitution of all relevant values of  $S_T$  and  $E(S_T)$  into equation 5.9 will give the molar susceptibility. As the number of paramagnetic centers increases, the equations get more complicated. If the symmetry of the multinuclear complex is considered, the equations for the Hamiltonian and  $\chi_M$  can be simplified. Trinuclear complexes are typically linear or triangular. In linear complexes, assuming symmetrical ligand bridges, the magnetic coupling from the central atom to each terminal atom can be considered equal. An equilateral triangular complex could be expressed as having one coupling J value while an isosceles triangle arrangement would have two. A scalene triangle would warrant three values of J and no simplification of the above equations 5.12-5.13.

### 5.3. LIGAND STERIC MEASUREMENT

The importance of steric effects in chemical transformations has long been studied in terms of the kinetics and thermodynamics of systems. However, the shape and spatial orientation of molecular fragments are commonly described only qualitatively. The first quantitative attempt to measure sterics was in 1894 [126]. The idea developed over the next 70 years into the Taft-Dubois steric parameter ( $E'_s$ ) which is the rate of acid catalyzed esterification of carboxylic acids in methanol at 40°C [126]. This along with the free energy differences ( $A$ -values) have become standard measures of the steric effects in organic molecules[126].

In metallic chemistry, the steric effects of ligands developed predominantly geometrically with the major onset in 1970 with definition of the Tolman cone angle,  $\theta$ . [126]. The Tolman cone angle was defined as the internal angle of a cone that enveloped the  $PR_3$  ligand 2.28Å from the nickel metal ion. Since then, the concept of a cone angle has been widely used in inorganic chemistry. In general, cone angles assume completely free rotation of the ligand and therefore a maximum estimation of the sterics. Also many newer defined steric parameters are normalized to the original 2.28Å distance to compare with previously calculated Tolman cone angles. A drawback of the cone angle parameter is that it does not consider the spatial overlapping or meshing of multiple ligands to reduce the steric strain around a metal[126].

In order to combat this issue, the solid angle approach was developed to quantify steric effects [126]. The solid angle is described by the area of the shadow a ligand would cast upon the surface of a sphere by a light source at the center of the sphere where the central metal is placed. This is then divided by the square of the radius of the sphere

to give the numerical measure of the solid angle( $\Omega$ ) in unitless steradians, where a value of  $4\pi$  would indicate the entire sphere was covered in shadow (Figure 5.4). Hence the solid angle not only considers the size of a ligand, but also the shape and conformation

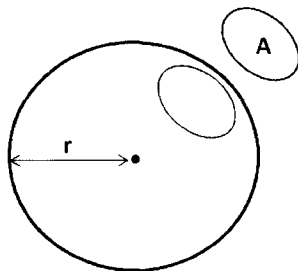


**Figure 5.4.** Geometric definition of a solid angle,  $\Omega = A/r^2$ .

that depend on the coordination center and other ligands present. Solid angles have been applied not only to ligands in coordination and organometallic compounds, but also to functional groups of organic compounds [127]. A fractional solid angle expressed as a percentage is intuitively more meaningful and has been defined as the G-parameter in the equation [128]

$$G = 100(\Omega/4\pi) \quad (5.14)$$

G-values expressed as percentages can be calculated from either single crystal X-ray data or theoretical molecular mechanics calculations. Qualitatively, the G-parameter is the percentage of the coordination sphere blocked by a particular ligand. Solid angles (and G-parameters) have a non-linear relationship to Tolman cone angles according to the relationship,  $\Omega = 2\pi(1-\cos(\theta/2))$ . In consideration of the G-values for a given ligand, it must be stated that G-values are calculated using radii ( $r_z$ ) of the zero-energy point of the

potential energy curve, where the repulsive interactions between two atoms becomes predominant, rather than Van-der-Waals radii[128]. Multidentate ligands are normalized by placing the centroid of the coordinated atoms 2.28Å from the central metal and then calculating the solid angle. The advantage of the G-parameter is that it is independent of the ligand size, shape, symmetry and hapticity. The major disadvantage of the calculated G-parameter is that it does not allow direct comparison of multidentate and monodentate ligand steric sizes[127].

Cone angles, solid angles and G-parameters depend on physical measurements and are necessarily predominantly geometric and apart from specific electronic environments. Overall ligand effects may also be described with other parameters specifically defined to describe both steric and electronic effects, such as ligand repulsive energies  $E_R$ [126], and the QALE method [129]. We are interested primarily in how the steric bulk of the R-substituent on N-Rsalicylaldimine affects the formation of a trinuclear nickel complex and evaluated our results using the solid angle/G-parameter approach.

#### **5.4. EXPERIMENTAL**

All reagent grade solvents were used as purchased. Elemental analysis of C, H, and N were carried out on a Perkin Elmer Series II-2400 CHNS analyzer. IR absorption spectra were measured using a Beckman-Coulter Spectrometer as solid KBr discs. UV-Vis data were measured on a Shimadzu UV-2101PC. Mass spectrometry data were measured using 75  $\mu$ M solutions in 80:20 CH<sub>3</sub>OH/CH<sub>3</sub>CN on a Shimadzu LCMS-2010 in positive ionization mode.

**5.4.1. Synthesis.** Bis(N-alkylsalicylaldimine) nickel(II) complexes, Ni(N-alkylsal)<sub>2</sub>, were synthesized from nickel(II) acetate monohydrate and the corresponding alkylamine according to the literature [130]. Trimethylorthoformate (TMOF) and triethylorthoformate (TEOF) were used to as solvents and to reduce the presence of water in the reaction.

Binuclear Compounds:

[Ni(iprsal)(NO<sub>3</sub>)(MeOH)]<sub>2</sub> : 0.25 mmol of Ni(iprsal)<sub>2</sub> was suspended in 3 mL of TMOF under N<sub>2</sub> to form a dark green solution. 5M Ni(NO<sub>3</sub>)<sub>2</sub>·6H<sub>2</sub>O was added dropwise (1 drop/minute) with stirring until the solution changed to a light green (6 drops). After one day, crystals suitable for single crystal X-ray analysis were removed where upon disturbance of the supersaturated solution caused precipitation. The precipitate was gravity filtered, washed with TMOF and dried in a desiccator over CaCl<sub>2</sub>. (0.12 g (75.9%). Ni<sub>2</sub>C<sub>22</sub>H<sub>30</sub>N<sub>4</sub>O<sub>10</sub>(C<sub>3</sub>H<sub>6</sub>O) Elemental Analysis (calc:found) C(43.76: 45.28), H(5.29:5.00), N(8.17:8.16). IR: (KBr, cm<sup>-1</sup>) 3432 (br,s), 2978(w), 1625 (s), 1600(m), 1384(m). ESI-MS (+ve) (m/z) 602 [complex-(MeOH)]<sup>+</sup>, 383 [Ni(iprsal)<sub>2</sub>]<sup>+</sup>, 164 (iprsal)<sup>+</sup>. X-ray crystallography: Ni<sub>2</sub>(iprsal)<sub>2</sub>(NO<sub>3</sub>)<sub>2</sub>(MeOH)<sub>2</sub>, P-1, R<sub>1</sub>=0.0337, wR<sub>2</sub>(all)= 0.1018, a=9.0997(4), b=9.3285(4), c=9.6045(4), α= 88.865(2), β=70.044(2), γ=69.396(2).

[Ni(benzylsal)(NO<sub>3</sub>)(MeOH)]<sub>2</sub> : 0.25 mmol of Ni(benzylsal)<sub>2</sub> was suspended in 3 mL of TMOF under N<sub>2</sub> to form a dark green solution. 5M Ni(NO<sub>3</sub>)<sub>2</sub>·6H<sub>2</sub>O was added dropwise (1 drop/minute) with stirring until the solution changed to a light green (17 drops). After one day, crystals suitable for single crystal X-ray crystallography were removed where upon disturbance of the supersaturated solution caused precipitation. The precipitate was gravity filtered, washed with TMOF and dried in a desiccator over CaCl<sub>2</sub>.

(0.07 g (24.6%).  $\text{Ni}_2\text{C}_{30}\text{H}_{30}\text{N}_4\text{O}_{10}$  Elemental Analysis: (calc:found) C(49.77: 48.19), H(4.18:4.03), N(7.74:8.00). ESI-MS (+ve) (m/z): 746 (complex+Na)<sup>+</sup>; 479 [Ni(benzylsal)<sub>2</sub>]<sup>+</sup>. X-ray crystallography:  $\text{Ni}_2(\text{benzylsal})_2(\text{NO}_3)_2(\text{MeOH})_2$ ,  $P2_1/c$ ,  $R_1=0.0297$ ,  $wR2$  all =0.1109,  $a=10.73(2)$ ,  $b=17.42(3)$ ,  $c=8.880(17)$ ,  $\beta=96.439(16)$ .

Trinuclear Compounds:

$\text{Ni}_3(\text{mesal})_4(\text{NO}_3)_2$  : In a closed vessel purged with  $\text{N}_2$  gas, 22 drops of a 5M solution of  $\text{Ni}(\text{NO}_3)_2 \cdot 6\text{H}_2\text{O}$  in TMOF were added dropwise to a  $\text{Ni}(\text{mesal})_2$  (0.5mmol) solution in TMOF (6mL) until the  $\text{Ni}(\text{mesal})_2$  just dissolved. The supernatant changed from a dark green to light green upon first drop of nickel nitrate with precipitation of a light green product within a couple seconds. The precipitate was gravity filtered, washed with TMOF and dried in a vacuum desiccator over  $\text{CaCl}_2$  (0.22 mg (91%). The filtrate evaporated slowly over 4 days to form small light green X-ray quality crystals.

$\text{Ni}_3\text{C}_{32}\text{H}_{32}\text{N}_6\text{O}_{10}$  Elemental Analysis (calc:found) C(45.93: 44.99), H(3.85:3.71), N(10.04:9.82). IR: (KBr,  $\text{cm}^{-1}$ ) 3407(br,m), 2926(w), 1639(s), 1600(m), 1562(m), 1476(w), 1444(w), 1385(m), 1275(m), 754(w). X-ray crystallography:  $\text{Ni}_3(\text{mesal})_4(\text{NO}_3)_2 \cdot 2\text{TMOF}$ , 100 K,  $P2_1/n$ ,  $R_1=0.0487$ ,  $wR2=0.0853$ ,  $a=14.479(4)$ ,  $b=17.322(4)$ ,  $c=18.659(5)$ ,  $\beta=112.83(3)$ .

$\text{Ni}_3(\text{etsal})_4(\text{NO}_3)_2$  : In a closed vessel purged with  $\text{N}_2$  gas, a 5M solution of  $\text{Ni}(\text{NO}_3)_2 \cdot 6\text{H}_2\text{O}$  in TMOF was added dropwise to  $\text{Ni}(\text{etsal})_2$  (0.5mmol) solution in 6 mL TMOF until  $\text{Ni}(\text{etsal})_2$  just dissolved. The solution changed to a lighter green and mixture let sit at room temp. After 2 days, X-ray quality crystals formed. Crystals were gravity filtered, washed with TMOF and dried in a vacuum desiccator over  $\text{CaCl}_2$  (0.22 mg (49%).  $\text{Ni}_3\text{C}_{36}\text{H}_{40}\text{N}_6\text{O}_{10}$  Elemental Analysis (calc:found) C(48.43: 48.32),



H(4.52:4.90), N(9.41:9.44). IR: (KBr,  $\text{cm}^{-1}$ ) 3433(br, m), 2933(w), 2893(w), 1631(s), 1599(m), 1558(m), 1476(w), 1448(w), 1384(m), 1275(m), 764(w). X-ray crystallography:  $\text{Ni}_3(\text{etsal})_4(\text{NO}_3)_2$ , 296 K, capillary,  $P2_1$ ,  $R_1=0.0283$ ,  $wR2 = 0.0428$ ,  $a = 10.611(6)$ ,  $b = 17.40(3)$ ,  $c = 11.94(2)$ ,  $\beta = 114.794(14)$ .

$\text{Ni}_3(\text{nprsal})_4(\text{NO}_3)_2$  : In a closed vessel purged with  $\text{N}_2$  gas,  $\text{Ni}(\text{nprsal})_2$  (0.5mmol) was dissolved in 9 mL TMOF to form a transparent dark green solution. A 5M solution of  $\text{Ni}(\text{NO}_3)_2 \cdot 6\text{H}_2\text{O}$  in TMOF was added dropwise to until  $\text{Ni}(\text{nprsal})_2$  just dissolved and the solution turned a lighter green (11 drops) and let sit at room temp. After 1 day, a polycrystalline precipitate formed. The precipitate was gravity filtered, washed with TMOF and recrystallized from TMOF, from which an X-ray quality crystal was chosen (0.16g, 24%).  $\text{Ni}_3\text{C}_{40}\text{H}_{48}\text{N}_6\text{O}_{10}$  Elemental Analysis (calc:found) C(50.63: 50.29), H(5.10:4.84), N(8.86:8.76). IR: (KBr,  $\text{cm}^{-1}$ ) 3412(br,m), 2927(w), 2872(w), 1630(s), 1599(m), 1478(w), 1447(w), 1384(m), 1275(m), 754(w). X-ray crystallography:  $\text{Ni}_3(\text{nprsal})_4(\text{NO}_3)_2$ , 296 K,  $C2/c$ ,  $R_1=0.040$ ,  $wR2$  all = 0.0697,  $a = 22.6401(10)$ ,  $b = 10.4168(5)$ ,  $c = 19.5336(9)$ ,  $\beta = 111.913(2)$ .

$\text{Ni}_3(\text{iprsal})_4(\text{NO}_3)_2$  : In a closed vessel purged with  $\text{N}_2$  gas,  $\text{Ni}(\text{nprsal})_2$  (0.5mmol) was mixed in 6 mL acetone to form a transparent dark green-black solution. 24 drops of 1.67 M solution of  $\text{Ni}(\text{NO}_3)_2 \cdot 6\text{H}_2\text{O}$  in acetone were added dropwise to the solution of  $\text{Ni}(\text{iprsal})_2$  until just dissolved and the solution turned a lighter green. After 12 days, a fine powdered precipitate formed. The precipitate was gravity filtered, washed with acetone and dried in a vacuum desiccator over  $\text{CaCl}_2$ . The decantate was left to slowly evaporate, from which x-ray quality crystals formed. (0.05g, 10%). IR: (KBr,  $\text{cm}^{-1}$ ) 3438(br,m), 2932(w), 2870(w), 1636(s), 1598(m), 1477(w), 1448(w), 1384(m), 1277(m),

760(w). X-ray crystallography:  $\text{Ni}_3(\text{iprsal})_4(\text{NO}_3)_2 \cdot 1/2 \text{C}_3\text{H}_6\text{O}$ , 296 K, C2/c,  $R_1=0.0360$ ,  $wR2 = 0.1205$ ,  $a=19.6674(2)$ ,  $b=22.8128(2)$ ,  $c=20.3191(2)$ ,  $\alpha=\beta=\gamma=90^\circ$ .

$\text{Ni}_3(\text{nbutsal})_4(\text{NO}_3)_2$  : In a closed vessel purged with  $\text{N}_2$  gas, 8 drops of a 5M solution of  $\text{Ni}(\text{NO}_3)_2 \cdot 6\text{H}_2\text{O}$  in TMOF were added dropwise to  $\text{Ni}(\text{nbutsal})_2$  (0.5mmol) in 6 mL TMOF until all solids just dissolved and a color change to light green appeared. A polycrystalline precipitate formed after 2 days, from which an X-ray quality crystal was chosen. The precipitate was washed with TMOF and dried in a desiccator over  $\text{CaCl}_2$ . 0.219g (43.7%).  $\text{Ni}_3\text{C}_{44}\text{H}_{56}\text{N}_6\text{O}_{10}$  Elemental Analysis (calc:found) C(52.56: 52.22), H(5.62:6.00), N(8.36:8.33). IR: (KBr,  $\text{cm}^{-1}$ ) 3400(br m), 2957(w), 2867(w), 1711(w), 1643(w), 1627(s), 1598(m), 1561(m), 1474(w), 1448(w), 1384(m), 1281(m), 756(w). X-ray crystallography:  $\text{Ni}_3(\text{nbutsal})_4(\text{NO}_3)_2$ , 296 K, Pccn,  $R_1=0.0601$ ,  $wR2$  all =0.0986,  $a=14.1839(10)$ ,  $b=15.6164(11)$ ,  $c=20.9135(15)$ ,  $\alpha=\beta=\gamma=90^\circ$ .

$\text{Ni}_3(\text{ibutsal})_4(\text{NO}_3)_2$  : In a closed vessel purged with  $\text{N}_2$  gas, 12 drops of a 5M solution of  $\text{Ni}(\text{NO}_3)_2 \cdot 6\text{H}_2\text{O}$  in TEOF were added dropwise to  $\text{Ni}(\text{ibutsal})_2$  (0.5mmol) in 6 mL TEOF until all solids just dissolved. A polycrystalline precipitate formed after 1 day, from which an X-ray quality crystal was chosen. The precipitate was washed with TEOF and dried in a desiccator over  $\text{CaCl}_2$ . 0.19g (76.7%).  $\text{Ni}_3\text{C}_{44}\text{H}_{56}\text{N}_6\text{O}_{10}$  Elemental Analysis (calc:found) C(52.56: 52.56), H(5.62:5.41), N(8.36:8.37). IR: (KBr,  $\text{cm}^{-1}$ ) 3428(br,m), 2959(w), 2869(w), 1626(s), 1600(m), 1471(w), 1447(w), 1385(m), 1277(m), 758(w). X-ray crystallography:  $\text{Ni}_3(\text{ibutsal})_4(\text{NO}_3)_2$ , 296 K,  $P2_1/n$ ,  $R_1=0.0640$ ,  $wR2$  all =0.1025,  $a=14.6104(7)$ ,  $b=22.1610(11)$ ,  $c=14.7873(7)$ ,  $\beta=97.421(2)^\circ$ .

$\text{Ni}_3(\text{benzylsal})_4(\text{NO}_3)_2$  : In a closed vessel purged with  $\text{N}_2$  gas, a 5M solution of  $\text{Ni}(\text{NO}_3)_2 \cdot 6\text{H}_2\text{O}$  in TMOF was added dropwise to  $\text{Ni}(\text{benzylbutsal})_2$  (0.5mmol) in 6 mL

TEOF until all solids just dissolved (16 drops). A dark green polycrystalline precipitate formed after 1 day, from which an X-ray quality crystal was chosen. The precipitate was washed with TMOF and dried in a desiccator over  $\text{CaCl}_2$ . 0.06g (21.4%) X-ray crystallography:  $\text{Ni}_3(\text{benzylbutsal})_4(\text{NO}_3)_2 \cdot 2\text{TMOF} \cdot \text{CH}_3\text{OH}$ , 296K, capillary,  $P2_1/n$ ,  $R_1=0.057$ ,  $wR2$  all = 0.0946,  $a=14.1379(7)$ ,  $b=31.8768(15)$ ,  $c=14.5100(7)$ ,  $\beta=94.05^\circ$ .

**5.4.2. X-ray Structure Determination.** Single crystal X-ray diffraction data collection and analysis were performed on a Bruker SMART APEXII diffractometer with a sealed tube,  $K_\alpha$  Mo source ( $\lambda=0.71073$  Å), graphite monochromator and CCD detector. An Oxford 700 Cryostream N2 open-flow temperature system was used for low temperature data collection where indicated. Alternatively, many crystals were measured at room temperature in sealed glass capillaries (noted where applicable). The unit cell refinement and the integration of the diffraction frames were done with Bruker SAINT. Intensity data were corrected for Lorentz and polarization effects. Absorption corrections were applied using SADABS and the structures were solved by direct methods and refined using least squares with the SHELXL-97 software program. Calculation of geometrical parameters was conducted using Mercury and figures were made using ORTEP, Mercury, PLATON, or SHELXTL. Hydrogens were either placed from the difference map with their positions freely refined, or placed in calculated positions and isotropically refined using a riding model.

**5.4.3. Magnetic Measurements.** Variable temperature susceptibility measurements were carried out in the temperature range of 2-300K with an applied field of 0.5 T on polycrystalline samples of  $\text{Ni}_2(\text{iprsal})_2(\text{NO}_3)_2(\text{CH}_3\text{OH})_2$  and  $\text{Ni}_3(\text{iprsal})_4(\text{NO}_3)_2$  (masses 66 and 18.5 mg, respectively) on a Quantum Design SQUID

magnetometer in the temperature range of 2-300K with an applied field of 5000 Oe. The susceptibility data were corrected for the sample holder previously measured using the same conditions and diamagnetic corrections as deduced from Pascal's constants ( $\chi_{\text{dia}} = -306.6 \times 10^{-6} \text{ emu.mol}^{-1}$  and  $-473.88 \times 10^{-6} \text{ emu.mol}^{-1}$  for  $\text{Ni}_2(\text{iprsal})_2(\text{NO}_3)_2(\text{CH}_3\text{OH})_2$  and  $\text{Ni}_3(\text{iprsal})_4(\text{NO}_3)_2$ , respectively. The experimental magnetic susceptibility data were fitted using the program package julX version 1.4.1 [131].

## 5.5. RESULTS AND DISCUSSION

**5.5.1. Synthesis and General Characterization.** The nickel complexes were prepared in three steps from nickel acetate, salicylaldehyde, a primary amine and nickel nitrate (Figure 5.5).

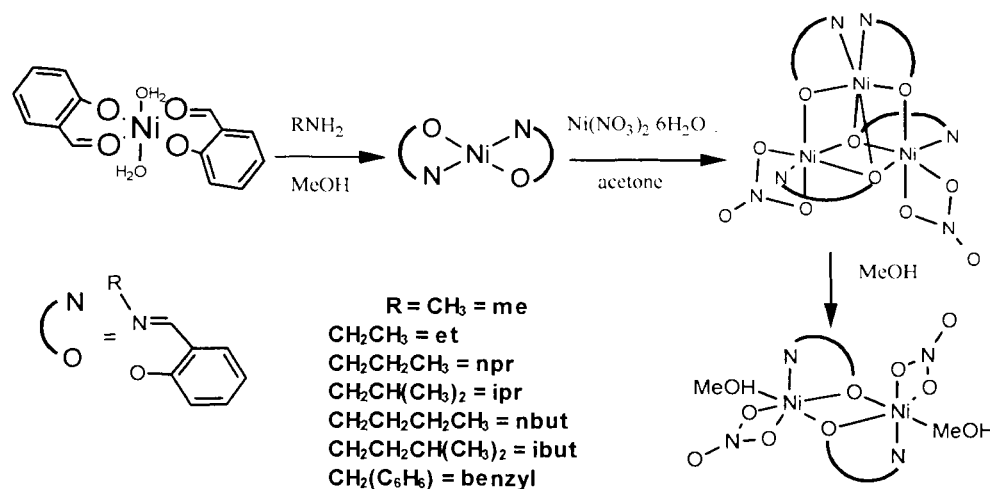


**Figure 5.5.** Formation of binuclear and trinuclear complexes.

The specific reaction conditions necessary to form the trinuclear compounds were investigated first with regards to molar ratio of the reactants,  $\text{Ni}(\text{N-Rsal})_2$  to  $\text{Ni}(\text{NO}_3)_2 \cdot 6\text{H}_2\text{O}$ . The expected reactant molar ratio of 2:1 for the trinuclear product and ratios from 1:5 to 5:1 were unable to produce reasonably pure precipitates when added together in bulk, refluxed or at alternate pH. In another case it was shown that formation of a tri- and binuclear nickel complexes were counter to the intuitive stoichiometric ratios [8]. Precipitation was determined the best way to isolate the compounds, as chromatography from the reaction mixture was extremely unsuccessful yielding only the nickel(II) nitrate, salicylaldehyde and the free amine. The possibility of the imine bond reacting with water from  $\text{Ni}(\text{NO}_3)_2 \cdot 6\text{H}_2\text{O}$  and splitting back into the amine and carbonyl compounds, was then mitigated by adding trimethylorthoformate (TMOF) to the reaction mixture and afterwards as the solvent. TMOF reacts with water to form methanol and methyl formate.

The predominant difference between the synthesis of the binuclear versus the trinuclear is the rate at which the nickel(II) nitrate was added and the presence of a solvent to fulfill the coordination sphere. Reactions of  $\text{Ni}(\text{N-benzylsal})_2$  with  $\text{Ni}(\text{NO}_3)_2 \cdot 6\text{H}_2\text{O}$  in TMOF that were left to react for longer periods of time, would initially produce the trinuclear product and then days later precipitate a binuclear product with methanol, originally from TMOF. The isopropyl analog produced synonymous results. Consequently, the reactions were repeated with acetone, having a lower coordination power than methanol[132]. The trinuclear product formation occurred for all but  $\text{R}=\text{isobutyl}$ . No binuclear product was recovered from the acetone reactions even after slow evaporation of the reaction mixture. These results indicate that while the necessity

of TMOF to remove water is not completely warranted, the presence of coordinating solvents, like methanol or ethanol increase the formation of the binuclear product. The solvent TEOF was also used for the reactions and displayed the same results as the TMOF reactions.

The IR spectra indicate significant differences between the mononuclear and bi-/tri-nuclear products. The imine stretch (C=N) shifts from 1608-1620  $\text{cm}^{-1}$  in the mononuclear complexes to a higher energy, 1625-1639  $\text{cm}^{-1}$  in the multinuclear products. The phenolic C-O stretch also increases from  $\sim 1540 \text{ cm}^{-1}$  to  $\sim 1560 \text{ cm}^{-1}$ , a shift characteristic of multinuclear complexes with phenolic bridges [133]. The appearance of a  $\text{NO}_2$  stretch at  $1277 \text{ cm}^{-1}$  indicates coordinated  $\text{NO}_3^-$ . Unfortunately, the spectra were taken in KBr slightly wet and so the broad peak around  $\sim 3400 \text{ cm}^{-1}$  was present but did not obscure the peaks of interest within the compounds. Although the elemental analysis agrees with the complexes, residual free  $\text{NO}_3^-$  persisted in the IR spectra exhibiting a peak at  $1384 \text{ cm}^{-1}$ .

Mass spectra were taken of all compounds, however, there was no presence of any of the trinuclear products in the solutions, but the spectra rather displayed the characteristic  $m/z$  ratios of the binuclear products. The lack of any trinuclear product presence in a liquid solvent corresponds to UV-VIS spectra taken that show no change in the absorption bands of  $\text{Ni}[\text{N-Rsal}]_2$  ( $\text{R}=\text{ipr}$ ,  $\lambda = 375, 316, 259 \text{ nm}$ ) compared to the bi or trinuclear products. It should be mentioned that  $\text{Ni}[\text{N-Rsal}]_2$  complexes tend to associate with solvent in solution to form octahedral complexes, hence the three absorption bands of the transitions,  ${}^3\text{T}_{2g}(\text{F}) \leftarrow {}^3\text{A}_{2g}$ ,  ${}^3\text{T}_{2g}(\text{F}) \leftarrow {}^3\text{A}_{2g}$  and  ${}^3\text{T}_{1g}(\text{P}) \leftarrow {}^3\text{A}_{2g}$ .

**5.5.2. Binuclear Structures.** Binuclear nickel(II) complexes with phenolate bridges are common [9, 5, 134-136] and have been studied for their potential as mimetic small molecular models of enzymes[137-139], , of which only the closely related  $[\text{Ni}(\text{iprsal})(\text{NO}_3)(\text{solvent})]_2$  has been previously reported [9]. The binuclear complexes contain two slightly distorted octahedral nickels separated by 3.008Å and 3.051Å in the isopropyl and benzyl analogs, respectively. In both complexes R= ipr and benzyl, the coordination of the Rsal ligands is  $\sim 63\text{-}65^\circ$  to the  $\mu_2\text{-O}$ -bridging plane with average Ni-O-Ni angles of  $96.56(4)^\circ$  and  $98.20(15)^\circ$ , respectively. The nitrate and methanol coordination allows for 4 hydrogen bonds to exist between dimer molecules forming 1D chains in the crystal. No uncoordinated solvent was present in either of the crystal lattices and the binuclear complexes arrange around the inversion centers of their centrosymmetric space groups. The ORTEP diagram of a binuclear is shown in Figure 5.6. The specific G-values[128] of the steric crowding of the synthesized nickel complexes are listed in Table 5.1 along with literature values. The steric bulk of the R-substituents on N-R-salicylaldimines was measured by subtraction of the G-value with and without the substituent. This allows a measure of the sterics imposed by the R-group on the coordination sphere of the nickel. There is little correlation of the solid angle values and G-values calculated with the literature values besides an increase from methyl to propyl. This is mainly due to the conformation of the R-groups in the crystal structures. In fact the conformation of the nbutyl group is extended back over the salicylaldimine portion of the ligand and accounts for the smaller G-value of 4.7% compared to n-propyl (5.0%). The G-value of isopropyl and benzyl R-groups in the binuclears are larger than in the trinuclears, indicating less overlap with other

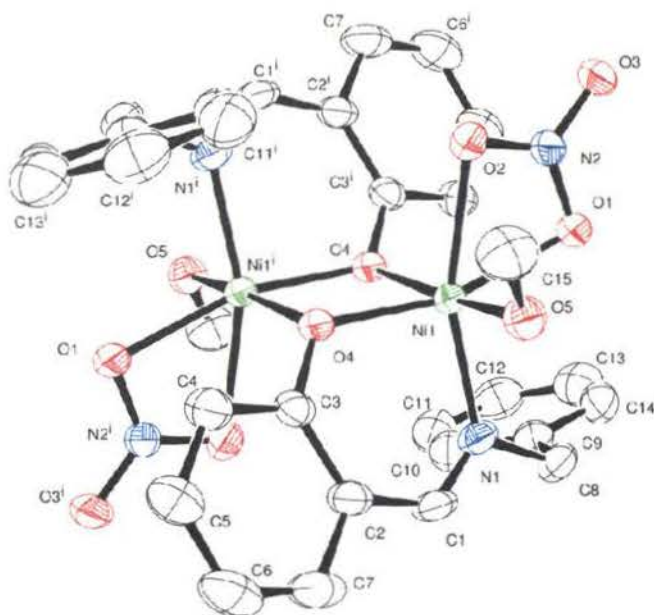


**Figure 5.6.** ORTEP diagram of  $[\text{Ni}(\text{benzylsal})(\text{NO}_3)(\text{MeOH})]_2$ . 30% displacement ellipsoids and hydrogens removed for clarity. Symmetry code:(i) 1-x, 2-y, 2-z.



ligands of the coordination sphere. Also listed in Table 5.1 is the amount of the coordination sphere occupied by the ligands around each of the nickel atoms. That leaves the remainder of the coordination sphere available for the bridging ligand of another nickel complex(es). The % shielded in the binuclear nickel complexes is similar for both the isopropyl and benzyl analogs at 77-78% per nickel atom.

**Table 5.1.** Steric Parameters for bi- and tri-nuclear nickel(II) N-alkylsalicylaldimines.

	$\theta$ (°)†	$\Omega$ (CO <sub>2</sub> H)‡	Change in Steric Values due to R-group			% Ni coord. sphere shielded by Ligands* (experimental M-L distance)		
			$\Omega$ (sr)	G (%)	$\theta_G$ (°)	Ni1	Ni2	Ni3
Methyl	112	0.211	0.35	2.8	8.1	70.5	59.7	59.4
ethyl	--	0.259	0.48	3.8	11.0	72.7	58.9	59.8
npropyl	143	0.274	0.62	5.0	14.2	72.9	60.9	--
isopropyl	135	0.306	0.56	4.4	13.0	71.7	61.1	60.3
nbutyl	143	0.276	0.41	4.7	13.5	75.0	59.7	--
isobutyl	--	0.305	0.65	5.2	14.8	74.1	61.1	60.3
benzyl	--	--	0.64	5.1	14.8	73.5	60.8	60.6
isopropyl (binuclear)			0.65	5.2	14.8	77.3		
benzyl (binuclear)			1.00	8.0	22.4	78.8		

† - cone angle from reference [118]

‡ - solid angle for substituent attached to the CO<sub>2</sub>H fragment [118]

\* - coordination spheres defined as Ni<sub>1</sub>(Rsal)<sub>2</sub>, Ni<sub>2</sub>(Rsal)(NO<sub>3</sub>) and Ni<sub>1</sub>(Rsal)(NO<sub>3</sub>)(MeOH) for Ni(apex trinuclear), Ni(basal, trinuclear) and Ni(binuclear), respectively. See Figure 5.6 for atom numbering scheme.

The effective magnetic moment per nickel ion of [Ni(iprsal)(NO<sub>3</sub>)(MeOH)]<sub>2</sub> versus temperature is shown in Figure 5.7. The  $\mu_{\text{eff}}$  is equal to 2.85  $\mu_B$  at 280 K, corresponding to the spin only value of an S=1 ion, and then increases to a maximum

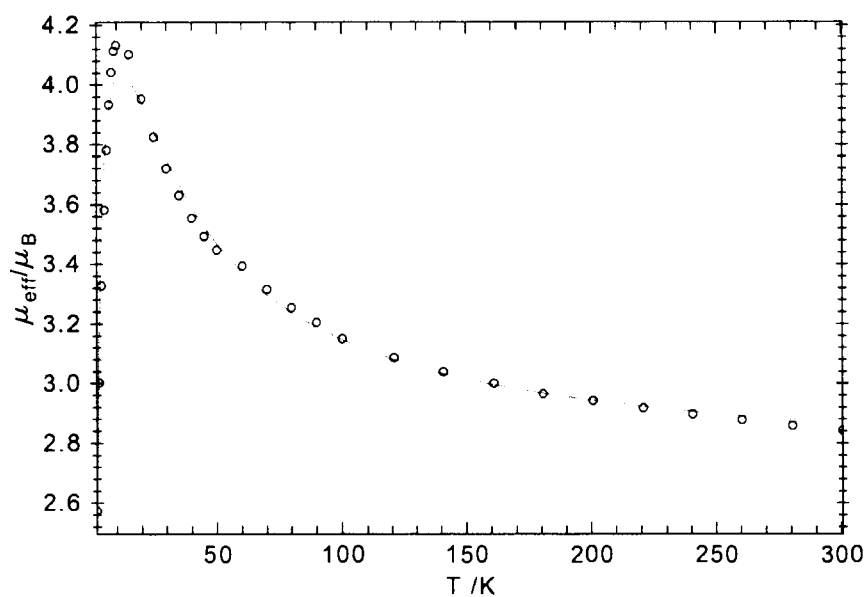


**Figure 5.7.** Effective magnetic moment per Ni atom of  $[\text{Ni}(\text{iprsal})(\text{NO}_3)(\text{MeOH})]_2$ . Open circles are the experimental data and the red line is the best fit using parameters stated in text.

value of  $4.13 \mu_{\text{B}}$  at 9.9 K corresponding more closely to an  $S=2$  ground state for the binuclear complex. Following this temperature,  $\mu_{\text{eff}}$  decreases rapidly to a value of  $2.57 \mu_{\text{B}}$  at 2 K attributed to either zero-field splitting or intermolecular antiferromagnetic interactions. The intermolecular hydrogen bonds of the binuclear  $[\text{Ni}(\text{Rsal})(\text{NO}_3)(\text{solvent})]_2$  complexes suggests enhanced cooperativity; however, addition of the interdimer exchange parameter  $zJ'$ , into the Hamiltonian equation, has been shown to have almost no effect on the fit of the theoretical model for this type of complex[9].

The experimental data were fitted using Equation 5.11 derived from the van Vleck equation (equation 5.9) for two  $S=1$  ions and the spin Hamiltonian:

$$H = -2 \sum_{ij} J_{ij} \hat{S}_i \cdot \hat{S}_j + \sum_{i=1}^{ns} D_i \left[ S_{z,i}^2 - \frac{1}{3} S_i(S_i + 1) \right] + \sum_{i=1}^{ns} g\beta \hat{S}_i \cdot \hat{H} \quad (5.15)$$

where the second summation term accounts for zero-field splitting and the third summation for the Zeeman interaction[131]. A moderate fit was obtained with the parameters  $g = 2.036$ ,  $J = 6.724 \text{ cm}^{-1}$ ,  $D_1 = 7.5 \text{ cm}^{-1}$ , however, there is still a significant disagreement between 5-20 K possibly due to the impurities from the trinuclear product or the reactant nickel compounds.

A linear correlation of the bridging angle in diphenoxo-bridged nickel(II) compounds and the coupling constant  $J$  has been proposed[5] suggesting that Ni-O-Ni angles less than  $\sim 97^\circ$  suggest ferromagnetic coupling and angles above  $97^\circ$  increasingly antiferromagnetic. This correlation was refuted [5] suggesting ferromagnetic coupling could occur in angles down to  $93.5^\circ$ . In a survey of symmetric bisoxo-bridged nickel compounds, Fondo et al. supported a lack of a simple linear relationship of the bridging angle with  $J$  value[5] as the superexchange pathway depends on other factors such as the Ni-O distance and the angle between the bridging plane and the rest of the coordination sphere. However, an exchange pathway between the two nickel atoms and the phenolate ligands  $\sim 65^\circ$  rotated from the bridging plane leading to a ferromagnetic interaction can be described  $\langle (\text{Ni})3d_{x^2-y^2} || (\text{O})sp^2 \perp (\text{O})p_z || (\text{Ni})3d_{z^2} \rangle$  indicating both compatible and orthogonal overlap of the orbitals[9].

**5.5.3. Trinuclear Complexes.** The neutral trinuclear nickel complexes consist of four bidentate uninegative Rsal ligands and two bidentate  $\text{NO}_3^-$  anionic ligands around three nickel(II) atoms. Each of the nickel atoms is octahedrally coordinated and slightly distorted with the trans angles around nickel ranging from  $153^\circ$  to  $163^\circ$  while the coordination bond lengths are within the expected range (Table 5.2). There are two  $\mu_2$ -O(Phenolate) bridges between the apical nickel atom (Ni1) and each basal nickel (Ni2

and Ni3). Two  $\mu_3$ -O(Phenolate) ligands, O3 and O4, bridge all three nickel centers (Figure 5.8). While the different complexes of the  $\text{Ni}_3(\text{R-sal})_4(\text{NO}_3)_2$  exhibit significantly

**Table 5.2.** Geometric parameters of  $\text{Ni}_3(\text{iprsal})_4(\text{NO}_3)_2$ . Selected bond lengths, interatomic distances(Å), and Ni-O-Ni bridging angles( $^\circ$ ) are shown.

Ni-O-Ni bridging angles			
Ni1—O1—Ni2	92.76(7)	Ni2—O4—Ni1	81.53(5)
Ni1—O2—Ni3	93.13(7)	Ni3—O3—Ni1	79.18(5)
Ni2—O3—Ni3	101.90(7)	Ni3—O4—Ni2	100.94(7)
Ni2—O3—Ni1	82.46(7)	Ni3—O4—Ni1	84.16(6)
Distances			
O1—Ni1	1.9690(17)	O4—Ni3	2.0177(16)
O1—Ni2	2.0474(17)	O4—Ni2	2.1616(16)
O2—Ni1	1.9604(17)	O4—Ni1	2.2898(17)
O2—Ni3	2.0245(16)	O5—Ni2	2.0857(19)
O3—Ni2	2.0050(17)	O6—Ni2	2.152(2)
O3—Ni3	2.1460(15)	O9—Ni3	2.1117(19)
O3—Ni1	2.3857(17)	O8—Ni3	2.0876(19)
N1—Ni1	2.026(2)	N3—Ni2	2.020(2)
N2—Ni1	2.010(2)	N4—Ni3	2.023(2)
Ni1...Ni2	2.9081(4)	Ni2...Ni3	3.2249(4)
Ni1...Ni3	2.8939(4)		

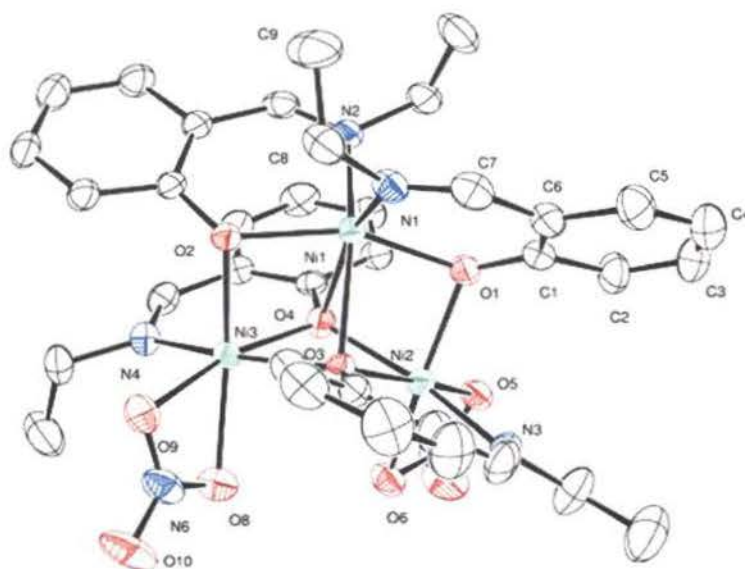


**Figure 5.8.** Molecular structure of  $\text{Ni}_3(\text{etsal})_4(\text{NO}_3)_2$ . Hydrogens removed and displacement ellipsoids at 30% probability.

different distances and angles from one another, they do not show any structural trends with R-group size. However, the definite increase in the steric parameters from methyl to ethyl seem to be visible also in the increased distance of Ni1 from the basal Ni atoms (Table 5.3). The same trinuclear bridging motif has only been reported in three other nickel complexes; one having phenolate bridges [140], one with a carbohydrate ligand [141] and a hexanuclear complex with amino alcohol ligands[142].

**Table 5.3.** Ni...Ni distances (Å) for  $\text{Ni}_3(\text{Rsal})_4(\text{NO}_3)_2$ .

R =	methyl	ethyl	npropyl	ipropyl	nbutyl	ibutyl	benzyl
Ni1...Ni2	2.8414 (9)	2.940 (3)	2.9064(5)	2.9081(4)	2.8984 (5)	2.9314 (7)	2.8764 (7)
Ni1...Ni3	2.8664 (9)	2.936 (4)	2.9065(5)	2.8939(4)	2.8983 (5)	2.9305 (7)	2.8777 (7)
Ni2...Ni3	3.1479(8)	3.185(5)	3.1175(4)	3.2249(4)	3.1709(5)	3.1805(7)	3.1420(8)

The report by Burkhardt et.al. [141] of a trinuclear carbohydrate complex interestingly showed an overall ferromagnetic interaction, so it is interesting to compare in more detail their structure with the ones synthesized here and specifically the isopropyl analog. The Ni1—O3, Ni1—O4 and Ni2···Ni3 distances for the carbohydrate complex (2.222(3), 2.182(3) and 3.1636(7) Å, respectively) exhibit the greatest difference from the N-isopropylsalicylaldimine complex distances (2.3857(17), 2.2898(17) and 3.2249(4)). The  $\mu_3$ -O bridging atoms are approximately 1.24 Å above and below the Ni<sub>3</sub> plane. The basal Ni2—O—Ni3 bridging angles are also smaller for the carbohydrate complex with angles of 96.83(10)° and 98.48(10)° compared to 100.94(7)° and 101.90(7)° for the N-isopropylsalicylaldimine complex. The polygon made by the bonds of the Ni2-O4-Ni3-O3 is more regular as the bite angles of the carbohydrate ligand are ~10° smaller than the salicylaldimines. Overall, the trinuclear core of the carbohydrate complex has a more regular shape and is more closely spaced than the salicylaldimines. The closer proximity may also be influenced by intramolecular hydrogen bonds of the ligands present in the carbohydrate complex.

Since the orthogonality versus planarity of the sal ligand exhibits opposite magnetic coupling effects in the binuclear complexes, the relationship of the sal ligand orientations may suggest the type of coupling present. The trinuclear complexes have three very roughly planar bridging planes each composed of two nickel atoms, two oxygen bridging atoms and the sal ligand combining them. The planes Ni1-O1-Ni2-O3 and Ni1-O2-Ni3-O4 have both R-salicylaldimine ligands at an average angle of 67° while the Ni2-O3-Ni3-O4 plane contains the Rsal ligands rotated only 15° from the plane. The exchange pathway described for the binuclear complexes assumes the  $p_z$  orbital of

oxygen is involved in the  $\pi$  overlap with the aromatic ring[99] and oriented to participate in  $\pi$ -bonding with the  $d_{z^2}$  orbitals of both nickel atoms along with  $\sigma$ -bonding between the  $sp^2$  orbitals of O and the  $d_{x^2-y^2}$  orbitals of the nickels. The exchange pathway of the trinuclears is much harder to describe. The Ni-O-C angles deviate more for the trinuclear complexes ( $\sim 127^\circ$ ) but the orbital configuration around the oxygen is still best described as  $sp^2$ . Taking the assumption that the p-orbital on O3 and O4 is oriented to be involved in the aromatic ring, it is then oriented to partially overlap the  $d_{z^2}$  orbital of Ni1 while the  $sp^2$   $\sigma$ -bonds interact with the  $d_{x^2-y^2}$  orbitals of Ni2 and Ni3. The p-orbitals of O1 and O2 are poised to overlap the  $d_{z^2}$  orbitals of Ni2 and Ni3.

On the basis of the crystal structure, the 2-fold symmetry of the trinuclear complexes allows for a simplification of the Hamiltonian for 3 spins (Equation 5.12). According to an isosceles triangle, the magnetic coupling between Ni1 and Ni2 is equivalent to the coupling from Ni1 to Ni3,  $J_{12}=J_{13}=J$ . A different type of interaction will occur between Ni2 and Ni3 described by a separate exchange parameter  $J_{23}$  (Figure 5.9).

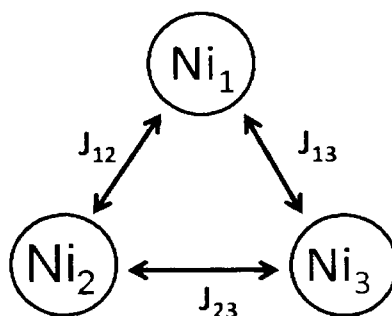


**Figure 5.9.** Coupling scheme applied to the trinuclear complexes.

Considering three  $\text{Ni}^{2+}$   $S=1$  paramagnetic centers, the energy states of the coupled system derived from Equation 5.12 when  $J_{12}=J_{13}=J$  can be expressed as

$$E(S_T) = -JS_T(S_T+1) + [J-J_{23}]S_{23}(S_{23}+1) + 2[J+2J_{23}] \quad (5.16)$$

where  $S_T = S_{23} + S_1, S_{23}+S_1-1, S_{23}+S_1-2, \dots, |S_{23}-S_1|$  and  $S_{23} = S_2+S_3, S_2+S_3-1, \dots, |S_2-S_3|$ .

This equation indicates that the energies of the states are dependent on the values of  $J$  and  $J_{23}$  relative to each other. As such, taking the relevant values of  $S_T$  and  $S_{23}$  and the range of possible  $J$  values, an energy level scheme can be developed for the system as shown in Figure 5.10. Substitution of all applicable combinations of the values of  $S_T$  (3,2,1) and

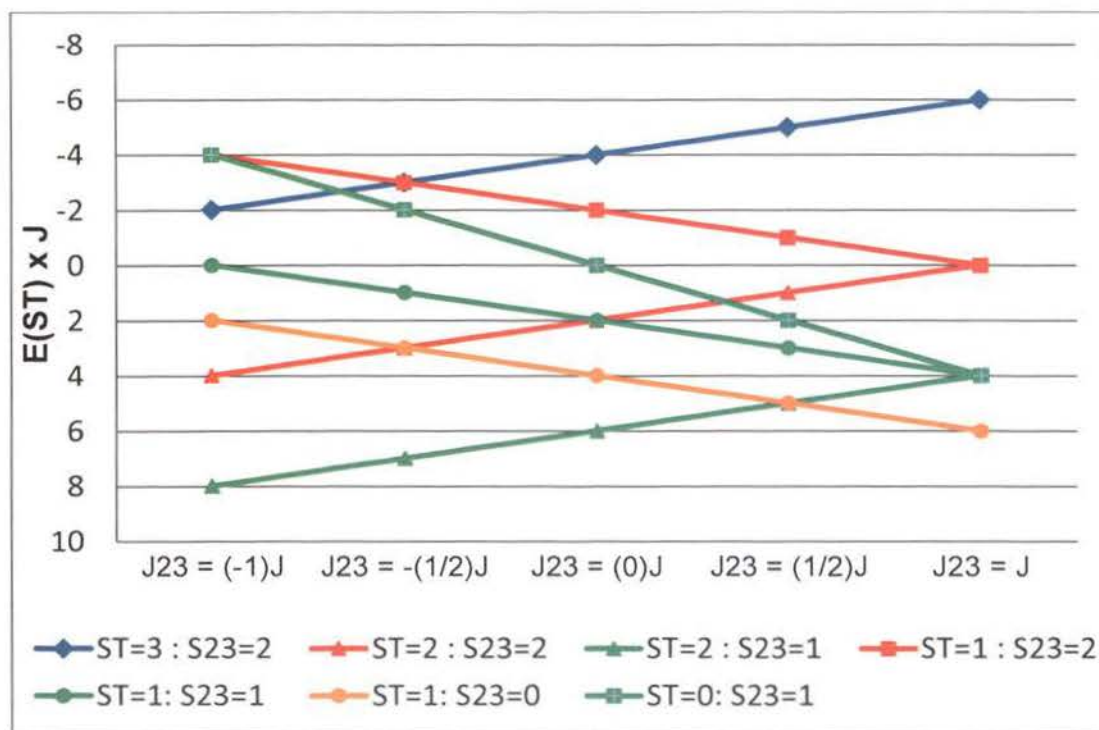


**Figure 5.10.** Energy level for isosceles triangle arrangement of 3  $S=1$  spin centers. Expressed a function of relative values of exchange constants  $J$  and  $J_{23}$ .



$S_{23}$  (2,1,0) evaluated by equation 5.16 into equation 5.9 yields the following susceptibility equation:

$$\chi_M = \frac{Ng^2\beta^2}{3kT} \times \frac{\text{Numerator}}{\text{Denominator}} \quad (5.17)$$

$$\begin{aligned} \text{Numerator} &= 84\exp\{(4J+2J_{23})/kT\} + 30\exp\{(-2J+2J_{23})/kT\} + 6\exp\{(-6J+2J_{23})/kT\} + \\ &30\exp\{(2J-2J_{23})/kT\} + 6\exp\{(-2J-2J_{23})/kT\} + 0\exp\{(-4J-2J_{23})/kT\} + 6\exp\{-4J_{23}/kT\} \\ \text{Denominator} &= 7\exp\{(4J+2J_{23})/kT\} + 5\exp\{(-2J+2J_{23})/kT\} + 3\exp\{(-6J+2J_{23})/kT\} + \\ &5\exp\{(2J-2J_{23})/kT\} + 3\exp\{(-2J-2J_{23})/kT\} + 1\exp\{(-4J-2J_{23})/kT\} + 3\exp\{-4J_{23}/kT\} \end{aligned}$$

Equation 5.17 modified for the zero-field splitting parameter as in equation 5.15, was used to fit the experimental data for  $\text{Ni}_3(\text{iprsal})_4(\text{NO}_3)_2$  (Figure 5.11). The best fit is

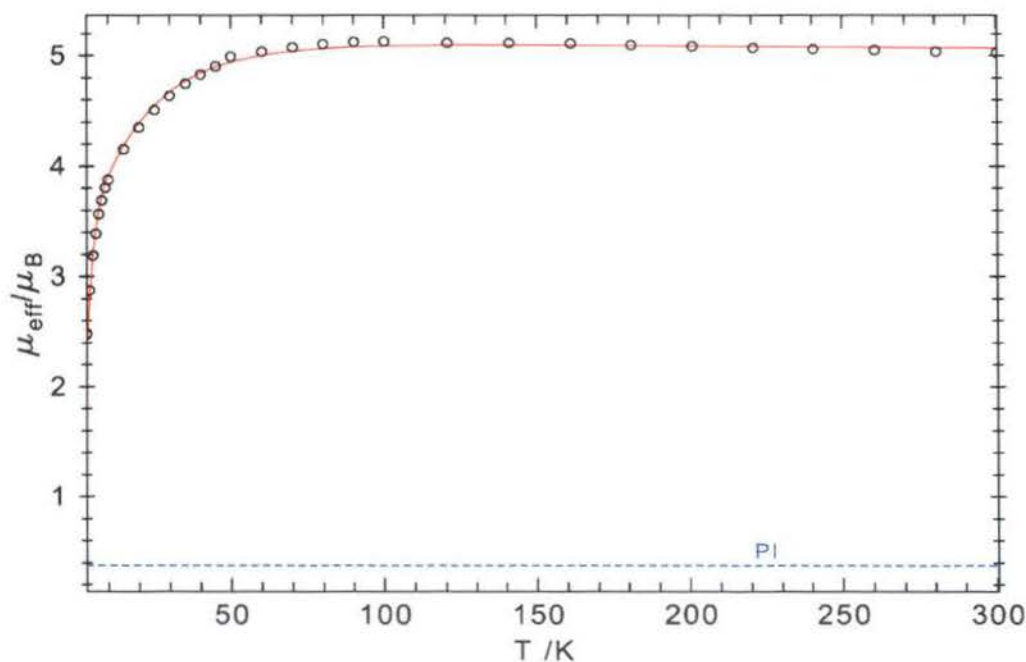


**Figure 5.11.** Effective magnetic moment of  $\text{Ni}_3(\text{iprsal})_4(\text{NO}_3)_2$ . Open circles are the experimental data and the red line is the best fit using parameters stated in text.

obtained with the parameters  $g_{1,2}=2.069$ ,  $g_3=2.019$ ,  $J_{12}=J_{13}=+11.386 \text{ cm}^{-1}$  and  $J_{23}=-13.891 \text{ cm}^{-1}$ .  $D_{1,2}=7.529$ ,  $D_3=2.834$ . An antiferromagnetic coupling between Ni2 and Ni3 agrees with the fact that two of the four sal ligands are parallel to that bridging plane. A ferromagnetic interaction between the Ni1 and Ni2/ Ni3 also agrees with the sal ligands arranging more orthogonally to the bridging planes along the Ni1-Ni2 and Ni1-Ni3 lengths of the triangle. It is not possible in an isosceles triangular arrangement for the spins to be aligned antiparallel to each other, so the energies of the states depend on the values of the exchange constants,  $J$  and  $J'$ . The experimental  $J$ -values correspond to the far left portion of the energy level scheme (Figure 5.10) and indicate a ground state of  $S_T=2$ ,  $S_{23}=1$ .

## 5.6. CONCLUSIONS

Reaction of mononuclear  $\text{Ni}(\text{N-alkyl-sal})_2$  complexes with  $\text{Ni}(\text{NO}_3)_2$  can form either nickel dimers or trinuclear complexes. Trinuclear nickel complexes are common in the literature, but are predominately synthesized serendipitously from set reaction conditions. This was the case with each of the three reported compounds exhibiting the exact bridging  $\mu_3\text{O}-\mu_2\text{O}-\text{Ni}_3$  core as  $\text{Ni}_3(\text{Rsal})_4(\text{NO}_3)_2$  [140-142]. Also in a previous study[9], the  $\text{Ni}_3(\text{Rsal})_4(\text{NO}_3)_2$  was unexpectedly formed and thought to have resulted due to low steric restrictions of the R-imine group. Rather than by chance, we were able to synthesize reproducibly a series of this core motif using a variety of sterically encumbered ligands, controlling the solvent coordination power and rate of reactant mixing. Trinuclear products form quickly in the reaction of mononuclear  $\text{Ni}(\text{N-R-sal})_2$  with  $\text{Ni}(\text{NO}_3)_2$  and will convert to binuclear products with the presence of an alcohol

coordinating solvent. Systematic control of the nuclearity of the complexes being synthesized has not been previously available.

Study of the trinuclear salicylaldimine system was predominantly of interest based on the realization that the magnetic exchange between nickel atoms could be rationalized by separate consideration of the magnetic exchange characteristics of the component binuclear structure fragments. Therefore, not only the synthetic conditions which generate the binuclear compounds, but also the structure and magnetic interactions that result are important. By looking at the X-ray structural information, the binuclear complexes,  $[\text{Ni}(\text{Rsal})(\text{NO}_3)(\text{MeOH})]_2$ , having orthogonal bridging sal ligands ( $\sim 67^\circ$ ), show overall ferromagnetic interactions with an exchange value of  $J = +6.724 \text{ cm}^{-1}$ . Antiferromagnetic interactions occur with sal bridging angles close to planer ( $< 20^\circ$ )[9]. These sal ligand geometric conditions provide a base from which to judge the trinuclear magnetic exchange couplings.

The triangular trinuclear crystal structures for  $\text{Ni}_3(\text{Rsal})_4(\text{NO}_3)_2$  from methyl to benzyl were solved and indicate the lack of steric restriction on formation for the series. The nickel trinuclear compounds form an isosceles triangle of metal atoms with four bidentate N-R-salicylaldimine ligands and two bidentate nitrate anions. The trinuclear complexes show slightly larger  $\text{Ni}_3\text{O}_4$  core distances and angles than other similar cores [140-142], and yield an overall antiferromagnetic interaction common of other  $\text{Ni}_3$  triangular complexes. However, the individual exchange interactions of the trinuclear correlate with to the sal ligand bridging angles initially demonstrated in the binuclear fragments; small angles ( $< 20^\circ$ ) between the bridging plane and the sal ligand planes

generate antiferromagnetic interactions (e.g.  $J = -13.891 \text{ cm}^{-1}$ ) while large ( $\sim 65^\circ$ ) angles generate ferromagnetic coupling (e.g.  $J = +11.386 \text{ cm}^{-1}$ ).

The relationship of the angle between the sal and bridging planes with the sign of the coupling constant between two nickel atoms can also tentatively explain results in other similar trinuclear nickel systems in the literature. For example, a similar trinuclear oximate bridged nickel complex [12] exhibited an overall antiferromagnetic interaction and coupling constants of  $J_{12} = -32.7 \text{ cm}^{-1}$ ,  $J_{13} = +12.5 \text{ cm}^{-1}$ , and  $J_{23} = +25.0 \text{ cm}^{-1}$  which upon inspection of the crystal structure agrees well with the general relationship found in our trinuclear nickel salicylaldimines. The angle between their basal  $\text{Ni}_2\text{O}_2\text{N}_2$  plane and the oximate ligands is  $\sim 30^\circ$  (antiferromagnetic interaction) while the angle between the other sides of the  $\text{Ni}_3$  triangle and the oximate ligands is an average of  $\sim 60^\circ$  corresponding to the ferromagnetic couplings. This explanation for the relative signs of the magnetic interactions was not available prior to our work.

The triangular arrangement of paramagnetic centers does not allow for a completely antiferromagnetic arrangement of the spins, so while it is not typical, it is not impossible to find individual coupling interactions of both ferro and antiferromagnetism within one molecule. Correlation of the individual, magnetic exchange constants and geometric parameters have also been found for Mn [6] and Cu [143] systems.

## 6. XANTHENE SPIROCYCLIC DETECTORS

### 6.1. INTRODUCTION

Optical sensing, in particular fluorescent sensing is an important mechanism by which to study environmental, biological and industrial samples. Several methods are used including atomic absorption spectroscopy [144], colorimetry [145], spectrophotometry [146-148], and voltammetry[149] techniques, which generally require sophisticated equipment, tedious sample preparation procedures, and trained operators. Fluorimetry has the advantage of speed, sensitivity, quantification, and is suitable for high-throughput screening and is non-destructive [150-156]. Of the great variety of fluorophores developed for sensing, xanthenes, including rhodamine and fluorescein, are ideal due to their excellent spectroscopic properties, such as long absorption and emission wavelength, high fluorescence quantum yield, large extinction coefficient, and high stability to light [157, 158, 159]. Fluorescence is of great use for specific applications when it can be generated in real time, or enhanced rather than quenched. In 1997, Czarnik et al. generated a considerable amount of interest with a rhodamine B hydrazine ring-opening reaction that exhibited a turn-on fluorescence change from colorless to pink [160]. The spirocyclic structure responsible for the fluorescence enhancement effect has been explored for the detection of a wide variety of metal ions, thiols, oxygen and nitrogen species [161]. We were able to contribute to this work with derivatives selective for the detection of  $\text{Fe}^{3+}$ ,  $\text{Cr}^{3+}$ ,  $\text{Co}^{2+}$ ,  $\text{Ni}^{2+}$ , and dichlorophosphate (DCP), a common mimic for the nerve gas agents like sarin, soman and tabun.

This work is in conjunction with colleagues, Aruna Weerasinghe and Fasil Abebe, who performed the spectroscopic and synthetic procedures, while I performed the X-ray structural analysis to determine possible binding modes and generally characterize the sample when suitable crystals were available.

## 6.2. RHODAMINE-B FOR THE DETECTION OF Cr<sup>3+</sup>

Chromium, as Cr<sup>3+</sup>, is involved in several cellular processes [162,163,164] and its deficiency can increase the risk factors associated with diabetes and cardiovascular diseases[165]. Agricultural and industrial activities can cause the accumulation of chromium in the environment [166]. Sensing of trivalent chromium can be difficult as it is known to quench many fluorophores due to its paramagnetic nature. Therefore, great importance is attached to developing selective chemosensors for chromium.

Rhodamine has been derivatized for the sensing of chromium by Mao et al. [167] and also Zhou et al. for detection in living cells [168]. We have synthesized a highly sensitive rhodamine sensor for chromium compared to the above-mentioned systems, by functionalizing rhodamine with thiophene-2-furaldehyde, sensor **1** (Figure 6.1). Sensor **1** shows very good

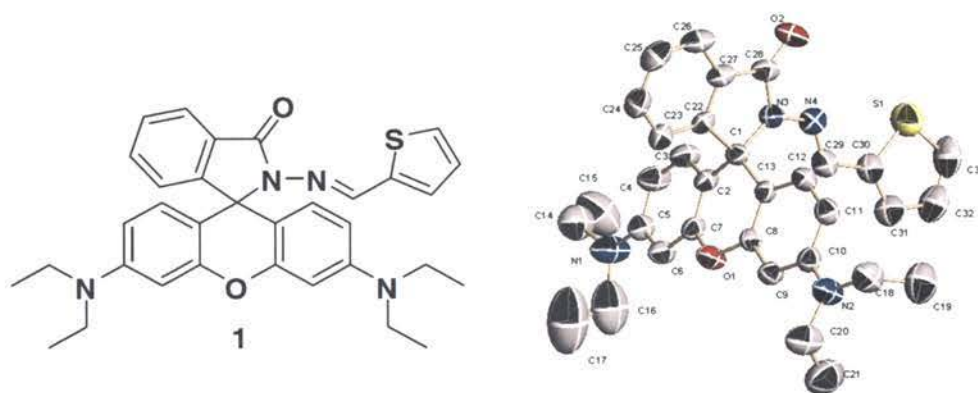


**Figure 6.1.** Structure of sensor **1**. Displacement ellipsoids at 50%. Hydrogens removed for clarity.

sensitivity as well as selectivity for  $\text{Cr}^{3+}$ . Both nitrate and perchlorate salts of chromium yielded essentially the same result. Moderate interference was found with  $\text{Hg}^{2+}$ , for which the nitrate salt showed emission enhancement while the perchlorate did not.

Compound **1** was designed to bind metal ions via the carbonyl O, imine N, and thiophene S as donors. The structure was verified by NMR, UV, MS, and single crystal X-ray diffraction. The single crystal was formed through slow evaporation from an acetonitrile solution. Sensor **1** crystallized in  $P2_1/c$  with unit cell dimensions of  $a = 17.6430(10) \text{ \AA}$ ,  $b = 11.5764(7) \text{ \AA}$ ,  $c = 29.3069(18) \text{ \AA}$ ,  $\beta = 102.799(3)^\circ$ . The  $R_1 = 0.0570$ ,  $wR2 = 0.1381$  and a goodness of fit of 1.026. The binding pocket is described by expected bond lengths and angles (Table 6.1). During binding with a metal ion, the thiophene moiety is expected to be in approximately the same conformation as seen in the crystal structure (Figure 6.1) except perhaps with a little torsional adaptation.

**Table 6.1.** Selected geometric parameter for compound **1**. Bond lengths (Å), bond angles (°) and Torsion angles(°) are shown.

C1-C2	1.511(6)	C2-C1-C13	110.0(3)	N3-C1-C2-C3	-39.7(5)
C1-C13	1.511(6)	N3-C1-C2	113.4(3)	C9-C8-C13-C1	-171.8(4)
N3-N4	1.376(5)	N3-C1-C13	112.0(3)	C13-C1-C22-C27	111.7(4)
N3-C1	1.491(5)	N3-C1-C22	98.8(3)	C22-C1-C13-C12	-70.3(5)
N3-C28	1.395(6)	N4-N3-C28	116.2(4)	C28-N3-C1-C2	125.9(4)

The spectroscopic studies were performed in acetonitrile in which sensor **1** formed a colorless solution and upon addition of  $\text{Cr}^{3+}$ , developed a UV absorbance at 559 nm with a shoulder at 520 nm. The association constant of compound **1** with  $\text{Cr}^{3+}$  [169] is  $2.0 \times 10^4 \text{ M}^{-1}$  indicating a 1:1 binding of sensor **1** with  $\text{Cr}^{3+}$ . The fluorescence of compound **1** is very weak in the absence of any metal ion, and then upon the addition of  $\text{Cr}^{3+}$ , an enhanced (>1200-fold) peak at 583 nm corresponds to delocalization in the xanthene moiety of rhodamine and opening of the spirolactam ring (C1-C22-C27-C28-N3) by breakage of the C1-N3 bond (Figure 6.1). Interferences from 12 different cations ( $\text{Na}^+$ ,  $\text{K}^+$ ,  $\text{Ni}^{2+}$ ,  $\text{Zn}^{2+}$ ,  $\text{Cd}^{2+}$ ,  $\text{Hg}^{2+}$ , and  $\text{Pb}^{2+}$ ,  $\text{Ca}^{2+}$ ,  $\text{Mn}^{2+}$ ,  $\text{Fe}^{3+}$ ,  $\text{Co}^{2+}$ , and  $\text{Cu}^{2+}$ ) were measured. Sensor **1** showed a certain emission enhancement with  $\text{Hg}^{2+}$  (<600-fold), while  $\text{Zn}^{2+}$  and  $\text{Pb}^{2+}$  showed very weak responses. The fluorescence spectra of Zn and Pb show a hypsochromic shift with respect to  $\text{Cr}^{3+}$  emission of 583 nm by 7-10 nm (Figure 6.2). The mechanism of action is similar to that of other spirocyclic chemosensors



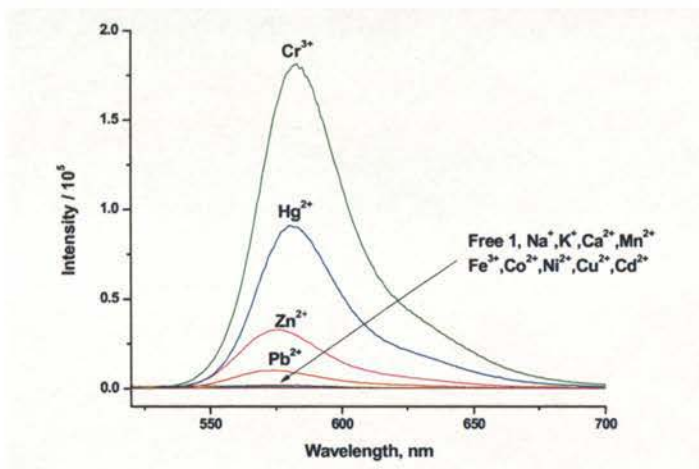


**Figure 6.2.** Fluorescence changes of **1**. Compound **1** (10  $\mu\text{M}$ ) with  $\text{Na}^+$ ,  $\text{K}^+$ ,  $\text{Ca}^{2+}$ ,  $\text{Cr}^{3+}$ ,  $\text{Mn}^{2+}$ ,  $\text{Fe}^{3+}$ ,  $\text{Co}^{2+}$ ,  $\text{Ni}^{2+}$ ,  $\text{Cu}^{2+}$ ,  $\text{Zn}^{2+}$ ,  $\text{Cd}^{2+}$ ,  $\text{Hg}^{2+}$ , and  $\text{Pb}^{2+}$  (10  $\mu\text{M}$ ) in  $\text{CH}_3\text{CN}$  (excitation at 510 nm).

due to the chelation of  $\text{Cr}^{3+}$  with the carbonyl oxygen, inamine nitrogen, and thiophene sulfur. The sensing of the compound **1** is reversible, as the fluorescence enhancement is reversed upon the addition of EDTA, which extracts the metal and returns the sensor to its original unbound form.

Overall, sensor **1** showed high sensitivity and selectivity towards  $\text{Cr}^{3+}$  over other interference cations except  $\text{Hg}^{2+}$ , which showed a significant but smaller effect. The sensitivity of our sensors matches that of the powerful  $\text{Hg}^{2+}$  sensor developed by Zhan et al. [170].

### 6.3. ELECTRONIC EFFECTS ON THE DETECTION OF DCP

Diethyl chlorophosphate (DCP) is a commonly studied as a mimic of nerve gas agents like sarin, tabun and soman which can be fatal in minutes when inhaled or absorbed through the skin [171]. Nerve gas agents are highly toxic organophosphonates,

which can inhibit acetylcholinesterase, a highly critical enzyme in nerve function.[172-173]. Different types of detection methods have been developed so far based on fluorescence[174-178], enzymes[179-183], interferometry[184], surface acoustic wave sensing[185, 186], and electrochemistry[187]. However, many of the methods suffer drawbacks such as lack of selectivity, operational complexity or limited portability.

Rhodamine spirolactam compounds are well-suited for fluorescence detection of a variety of analytes and have already been successfully used for a variety of metal ions, such as  $\text{Cu}^{2+}$ [188, 189],  $\text{Fe}^{3+}$ [157, 190, 191],  $\text{Pb}^{2+}$ [192],  $\text{Hg}^{2+}$ [193-195] and  $\text{Cr}^{3+}$ [158]. It is well known that the equilibrium between the non-fluorescent colorless ring-closed form and the highly fluorescent pink-colored ring-open form, provides a better model for the development of turn-on sensors. Recently, Kang et al. have reported some rhodaminehydrazides as sensors for nerve agent mimics, such as diethyl chlorophosphate (DCP) in the solid phase. Han et al. also reported a rhodamine compound sensitive to organophosphates [196] down to 25 ppm; however the fluorescence response only occurs after incubation for 20 minutes. Here we report a series of rhodamine-based compounds as sensors for nerve gas agents in solution and in significantly reduced time.

We have synthesized six new rhodamine B derivatives with an electron rich furan moiety. Different substituent groups in the furan ring were used to study the effect of electronics and sterics on the sensitivity of the sensor toward DCP. Chemosensors **1-6** were synthesized using Schiff-base condensation between the amine-containing compound **7**[188] and the corresponding aldehyde in ethanol (Figure 6.3). In order to

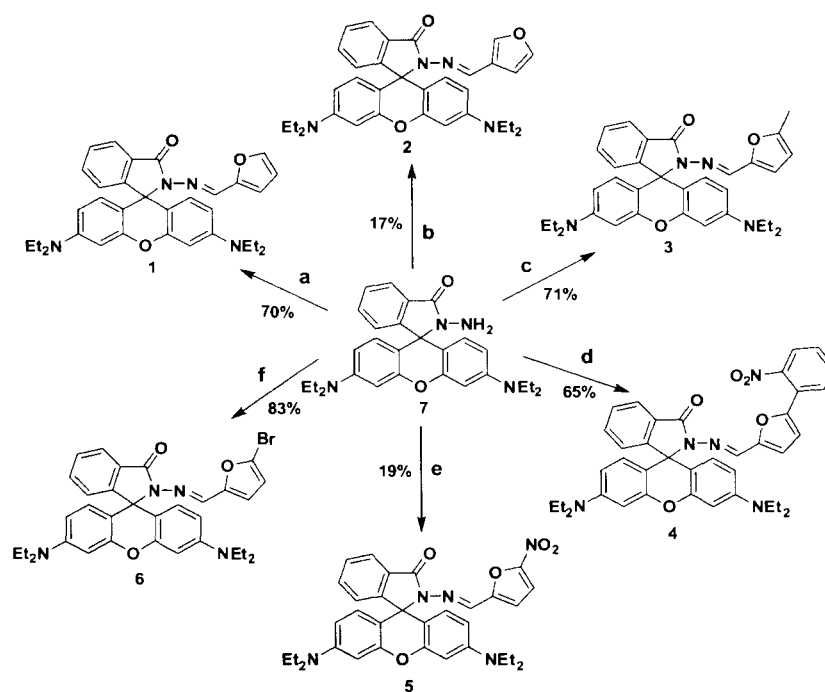


**Figure 6.3.** Synthesis of 1-6. Compound 7 was refluxed with the corresponding aldehyde in ethanol: a. 2-furaldehyde, b. 3-furaldehyde, c. 5-methyl-2-furaldehyde, d. 5-(2-nitrophenyl)-2-furaldehyde, e. 5-nitro-2-furaldehyde, f. 5-bromo-2-furaldehyde.

verify the structures of the Schiff base derivatives, as well as to obtain information about possible binding pockets for the substrates of these detectors, attempts were made to crystallize each of the compounds 1-7. Though not successful in all cases, a representative set containing 1, 2, 3, 4, and 6, of the complexes were grown from acetonitrile as single crystals and their structure determined by X-ray crystallography. The structures were verified using  $^1\text{H}$  NMR,  $^{13}\text{C}$  NMR, mass spectrometry and elemental analysis.

Of all crystal structures, compound 1 and 4 contained a molecule of acetonitrile in the asymmetric unit (Figure 6.4a). The acetonitrile molecule inhabits a void space

between the rhodamine molecules and extends infinitely in the  $[110]$  direction. Empirical absorption corrections were done on each sample, but were only significantly needed

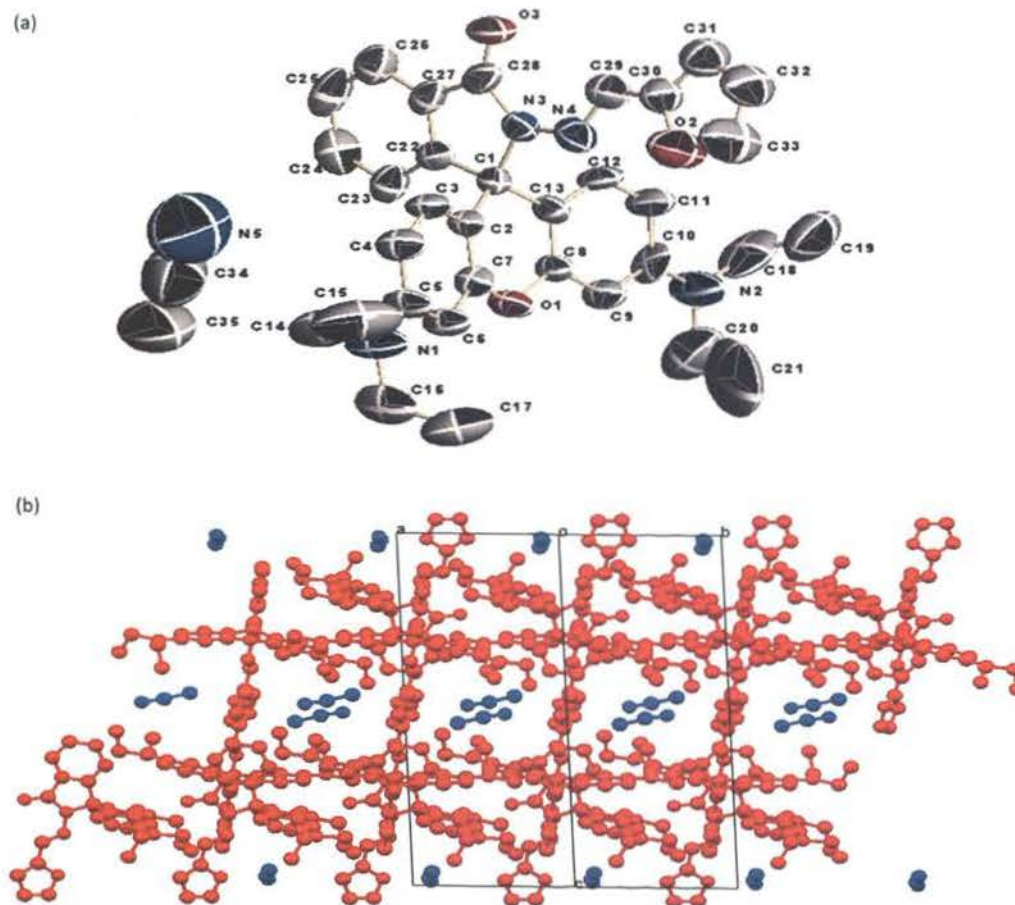


**Figure 6.4.** ORTEP and packing diagrams of compound **1**. (a) 50% displacement ellipsoids, showing the occluded acetonitrile molecule. Hydrogens removed for clarity. (b) Packing diagram of **1** with rhodamine molecules in red and acetonitrile solvent in blue looking down the  $[110]$  direction.

in the case of compound **6** due to the presence of bromine absorbing much more of the X-rays. It is not surprising that compound **3** and **6** crystallize with synonymous cell

dimensions (Table 6.2) as the methyl and bromide substituents geometrically occupy the same space. The  $R_1$  value for compounds **2** and **6** are a little large due to unresolved disorder in the N-ethyl groups on the xanthene ring. The bond lengths and angles of all the structures conform to expected ranges and differ in only a couple instances between the structures. Angle N4-N3-C28 is 10-15° larger for compounds **1** and **4** compared to the other structures due to the "cis" orientation of the N4-C29 bond relative to the N3-C28 and C28-O3 bonds (Figure 6.4). In all the other structures, an "trans" conformation is present. Overall the conformation of the structures in the solid state provide a clue to the possible conformations in the liquid phase especially since these structures are relatively free of strong intermolecular interactions such as hydrogen bonds. As in Figure 6.4, each of the structures requires a conformational change for binding to occur with atoms of the imine-moiety.

**Table 6.2.** Crystal data and refinement parameters.

Compound	<b>1</b>	<b>2</b>	<b>3</b>	<b>4</b>	<b>6</b>
CCDC	730371	759587	759585	759584	759586
	$C_{35}H_{37}N_5O_3$	$C_{33}H_{34}N_4O_3$	$C_{34}H_{36}N_4O_3$	$C_{41}H_{40}N_6O_5$	$C_{33}H_{33}BrN_4O_3$
Crystal system	monoclinic	monoclinic	orthorhombic	monoclinic	orthorhombic
Space group	P 1 21/n 1	P 1 21/c 1	P c a 21	P 1 21/n 1	P c a 21
<u>Unit cell dimensions</u>					
a (Å)	11.868(6)	17.4993	20.7388(2)	11.8149(5)	20.5931(5)
b (Å)	11.787(10)	11.5789	11.9816(2)	11.5722(5)	12.0025(2)
c (Å)	22.553(11)	29.1461	12.2015(2)	26.1223(11)	12.2360(4)
$\alpha$ (°)	90	90.000	90	90	90
$\beta$ (°)	93.81(3)	103.191	90	98.9570(10)	90
$\gamma$ (°)	90	90.000	90	90	90
Volume(Å <sup>3</sup> )	3148.(3)	5749.8	3031.88(8)	3528.0(3)	3024.36(15)
Z	4	8	4	4	4
Density (calc) mg/cm <sup>3</sup>	1.215	1.237	1.202	1.312	1.347

**Table 6.2.** Crystal data and refinement parameters. (cont.)

Abs. coeff. (mm <sup>-1</sup> )	0.079	0.080	0.078	0.088	1.399
*D / R / P	1910 / 0 / 521	14261 / 0 / 730	6181 / 1 / 376	7761 / 0 / 629	6674 / 1 / 374
S	1.026	1.014	1.159	0.99	1.127
<u>R indices I&gt;2σ(I)</u>					
R1	0.0403	0.0712	0.0593	0.0502	0.0669
wR2	0.1089	0.1906	0.1648	0.1099	0.1644

\*D/R/P – data/restraints/parameters

All the spectroscopic studies were performed in 50% CH<sub>3</sub>CN, 50% 0.01 M Tris-HCl buffer (pH=7.0) medium in which compounds formed colorless solutions. Generally rhodamine-based compounds are protonated at acidic conditions and emit strong fluorescence. The colorless solutions were very weakly fluorescent and showed no absorption above 450 nm, properties, which are characteristic of the predominant ring-closed spirolactam.

Compound 1 showed the highest fluorescence enhancement (>165-fold) at 583 nm in the presence of DCP compared to the compounds 2-7 (Figure 6.5). Interestingly, 1 also shows an absorbance enhancement with Cu<sup>2+</sup>, but no fluorescence change, showing sensing depending to the interaction phenomenon with no interference from the corresponding analyte. Interference from metal ions, HCl and another nerve gas mimic, DMMP (dimethyl methylphosphonate) were also measured for each system. Slight enhancement with Cr<sup>3+</sup> was found for compounds 1 and 3. Compound 4 also showed

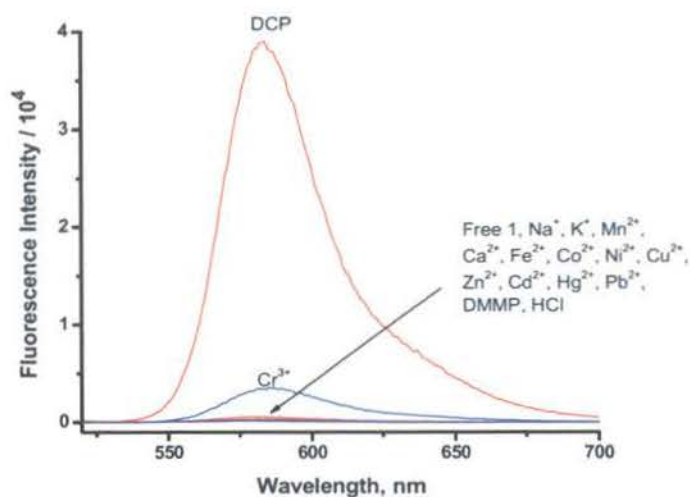


**Figure 6.5.** Fluorescence spectra of compound **1**. Compound **1** (10 mM) with DCP, DMMP, HCl, and metals (340 mM) in 50% CH<sub>3</sub>CN, 50% 0.01 M Tris-HCl buffer (pH=7.0) ( $\lambda_{ex}$ =510 nm).

fluorescence enhancement (10-fold) with Cu<sup>2+</sup>. Lack of interference with DMMP indicates the importance of the chloride leaving group of DCP in the sensing mechanism.

In order to study the importance of the furan moiety on the sensing of DCP, a variety of substituted analogs were tested. Compound **2**, with the position of the oxygen moved to the 3-position of the furan ring showed significantly lower fluorescence with DCP than **1**. Electron withdrawing groups, -NO<sub>2</sub> and Br both exhibited lower emission intensities than all compounds tested, while the electron-donating methyl group on compound **3** showed an increase in DCP-induced enhancement. The calculated binding constant is  $3.4 \times 10^3 \text{ M}^{-1}$ , which is the highest of the compounds studied. This clearly indicates that an electron-donating group can improve the sensitivity of the sensor. Association constants for each compound are shown in Table 6.3. The fluorescence enhancement while not instantaneous in the buffer solution, appears and saturates in 4-9

minutes, about half the time previously reported for a similar rhodamine sensor[196]. The detection limit of 1 in the buffer system is 170  $\mu\text{M}$ .

**Table 6.3.** Association constants of compounds 1-6 with DCP.

Compound	Association constant, $K/M^{-1}$
1	$3.0 \times 10^3$
2	$1.69 \times 10^3$
3	$3.4 \times 10^3$
4	$2.1 \times 10^3$
5	17
6	$1.75 \times 10^3$

Evidence of the interaction of DCP with compound 1 was shown via NMR studies that showed a broadening in the imine-H peak and also some of the xanthene hydrogens. However no interaction was noticeable in the furan hydrogen peaks. Addition of EDTA removes the fluorescence back to the non-fluorescent ring-closed form of the spirocycle. Based on an interaction between the phosphorus of DCP and the carbonyl of rhodamine, it is expected that a similar competitive interaction is occurring between the polarizable P=O of DCP and carbonylates of EDTA.

In conclusion, rhodamine spirolactam ring-opening compounds 1-7 were used to selectively and sensitively detect the presence of DCP by fluorescence enhancement. Electron withdrawing groups on the furan moiety cause a significant decrease in the sensitivity of the sensors while electron-donating groups show an increase. The



compounds show significantly reduced timescales of 4-9 minutes and reversibility in the presence of EDTA.

#### 6.4. FLUOROSCEIN FOR THE DETECTION OF $\text{Ni}^{2+}$ AND $\text{Co}^{2+}$

Xanthene spirolactams made with fluorescein enjoy a greater solubility in water than rhodamine analogs. Fluorescein fluorophores are desirable for their visible excitation and emission and maximum brightness at physiological pH [197]. In the lactam form, fluorescein derivatives are nonfluorescent and when in the ring-open form can exhibit a color change and fluorescent enhancements. We have applied the concept to modified fluorescein spirolactam molecules for the detection of cobalt and nickel ions. Many fluorescent sensors display amplification for transition metal ions, such as  $\text{Zn}^{2+}$ , [198, 199]  $\text{Cu}^{2+}$ , [200, 201]  $\text{Fe}^{3+}$ , [202, 203] but fluorescence molecules suitable for use with typical transition metal fluorescence quenchers, viz  $\text{Ni}^{2+}$  and  $\text{Co}^{2+}$ , are scarce. Bharadwaj [204] and Qian [205] reported two sensors that provided an enhanced fluorescence response toward  $\text{Ni}^{2+}$  and  $\text{Co}^{2+}$  in the absence of oxidizing agents. However, subsequently, de Silva et al. [206], indicated that these results must be treated with caution, as the onset of fluorescence is most likely attributable to the protonation of an amino receptor. Hence, there is still a need to develop the readily available fluorescent sensors which display an enhanced fluorescence due to the coordination with  $\text{Co}^{2+}$  or  $\text{Ni}^{2+}$  ions.

Here we report two new fluorescein-derived colorimetric sensors, **1** and **2**, which are rapid and selective, and capable of detecting paramagnetic  $\text{Co}^{2+}$  and  $\text{Ni}^{2+}$  in aqueous media. Compounds **1** and **2** were designed to bind metal ions via the carbonyl O and

inamine N groups as donors. Both function as excellent  $\text{Co}^{2+}$  and  $\text{Ni}^{2+}$  sensors while other common metals, particularly the alkalis, alkaline earths, and transition metals produce little or minimal spectral change.

Compounds **1** and **2** were prepared (Figure 6.6) The structures were determined by X-ray diffraction and confirmed using  $^1\text{H}$  NMR,  $^{13}\text{C}$  NMR, mass spectrometry and elemental analysis. Both structures show the junction of mean planes of atoms at the point

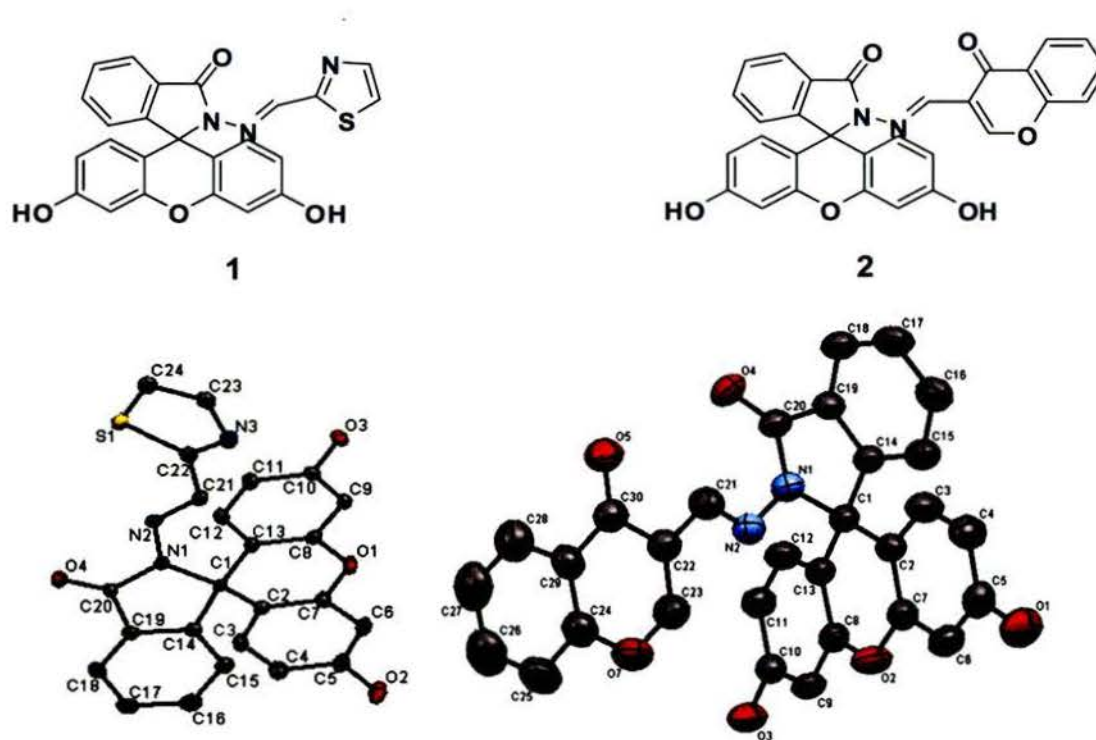


**Figure 6.6.** Structure of sensors **1** and **2**. Hydrogen removed for clarity and structures shown with 50% ellipsoids.

of C1 and at an angle of  $88.38^\circ$  for **1** and  $87.94^\circ$  for **2**. The carbonyl group (O4) from the 5-membered spirolactam ring participates in H-bonding with a hydroxyl group of the fluorescein moiety in a neighboring molecule in both compounds.

The structure of compound **2** also contains 4 hydrogen bonds per molecule. Each carbonyl oxygen is H-bonded (avg.  $2.862 \text{ \AA}$ ) to a hydroxyl group of the neighboring molecule in order to form 1D chains rather than associated dimers (Figure 6.7a). Each H-bonded chain is closely associated due to the aromatic stacking interactions between the fluorescein moieties with an inter-plane separation of  $3.616 \text{ \AA}$  (Figure 6.7b). The packing of these cross-shaped molecules also provides large voids occupied by disordered THF molecules.

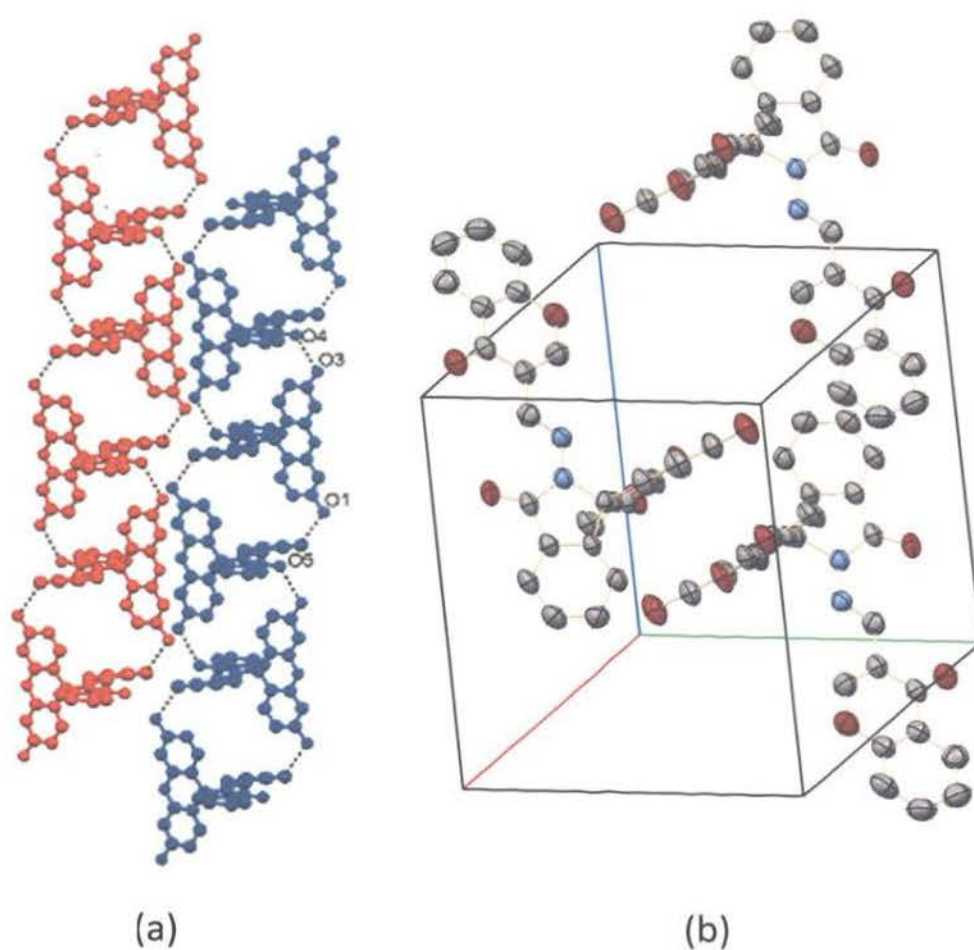


**Figure 6.7.** Packing diagrams for compound 2. (a) 2-dimensional H-bonded chains in Compound 2 (b) ORTEP packing diagram for Compound 2. THF molecules present in the interstitial spaces are removed for clarity.

In Compound 1, one hydroxyl group of the fluorescein moiety hydrogen bonds with the carbonyl oxygen of the neighboring molecule related by a 2-fold screw axis about [010] and at a donor-acceptor distance of 2.7045(15) Å. The other hydroxyl group begins a network of three H-bonds generated through both ethanol oxygens to the nitrogen atom within the thiazole ring (Figure 6.8). This network of hydrogen bonding is

likely the predominant factor orienting the thiazole ring within the crystal structure showing the plane of the ring at  $18.75^\circ$  rotated from the carbonyl. The sulfur atom

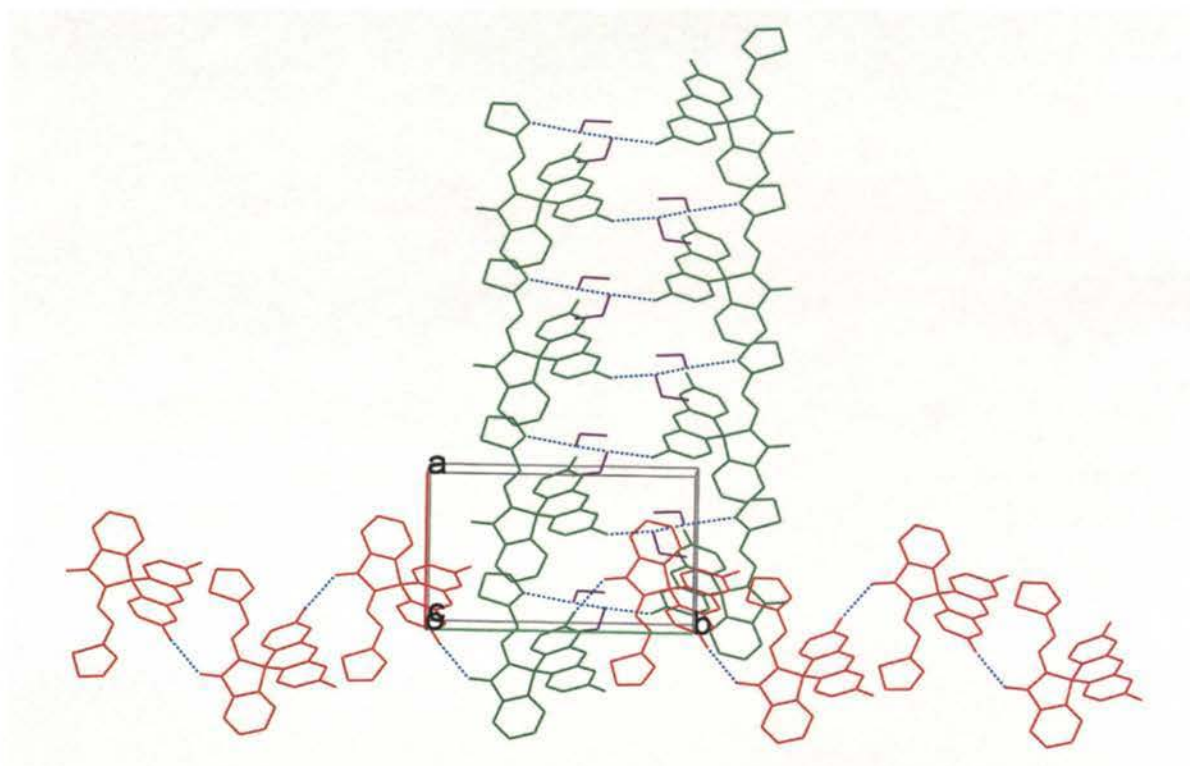


**Figure 6.8.** Packing diagrams for Compound 1. Hydrogen bonding framework in the *ab* plane is shown. Fluorescein molecule in red and green; ethanol in purple; H-bonds shown as blue, dashed lines.

points in the same general direction as the carbonyl group and cation binding pocket. However, since nitrogen is a much harder base compared to sulfur, it is postulated that rotation occurs about the C21–C22 bond. This yields a pocket of hard donors, the carbonyl oxygen and imine nitrogen, which are more favorable ligands for the hard  $\text{Ni}^{2+}$  and  $\text{Co}^{2+}$  ions (Figure 6.6).

All spectroscopic studies were performed in 2% DMSO in aqueous solution in which the sensors formed colorless solutions and titration experiments were carried out at

ambient temperature. The fluorescence spectra were obtained by excitation of the fluorescein fluorophore at 470 nm. The sensing and optical measurements were performed in 10 mM Tris–HCl buffer solution with a pH of 7.5 to keep the dye molecules in their ring closed form. The resulting solutions were shaken well before recording the absorption and emission spectra. Chlorides of  $\text{Ca}^{2+}$ ,  $\text{K}^+$ ,  $\text{Fe}^{3+}$ ,  $\text{Fe}^{2+}$ ,  $\text{Pb}^{2+}$ ,  $\text{Co}^{2+}$ ,  $\text{Zn}^{2+}$ ,  $\text{Cd}^{2+}$  and nitrates of  $\text{Cr}^{3+}$ ,  $\text{Hg}^{2+}$  and  $\text{Ni}^{2+}$ , ions were evaluated for their metal-binding properties with compounds **1** and **2** (10  $\mu\text{M}$ ) in DMSO–water. Solutions of free **1** and **2** are nearly void of absorption in the visible. The absorption spectrum of **1** and **2** (10  $\mu\text{M}$ ) in DMSO–water exhibited only a very weak band above 400 nm, ascribed to a trace of the ring-open form of the compounds, but addition of 1 equiv  $\text{Co}^{2+}$  and  $\text{Ni}^{2+}$  showed a new absorbance peak at 500 nm with an immediate color change visible to naked eye (Figure 6.9). Interestingly, both ions showed the higher absorbance enhancement (18-fold) than other metals showing no significant interference.

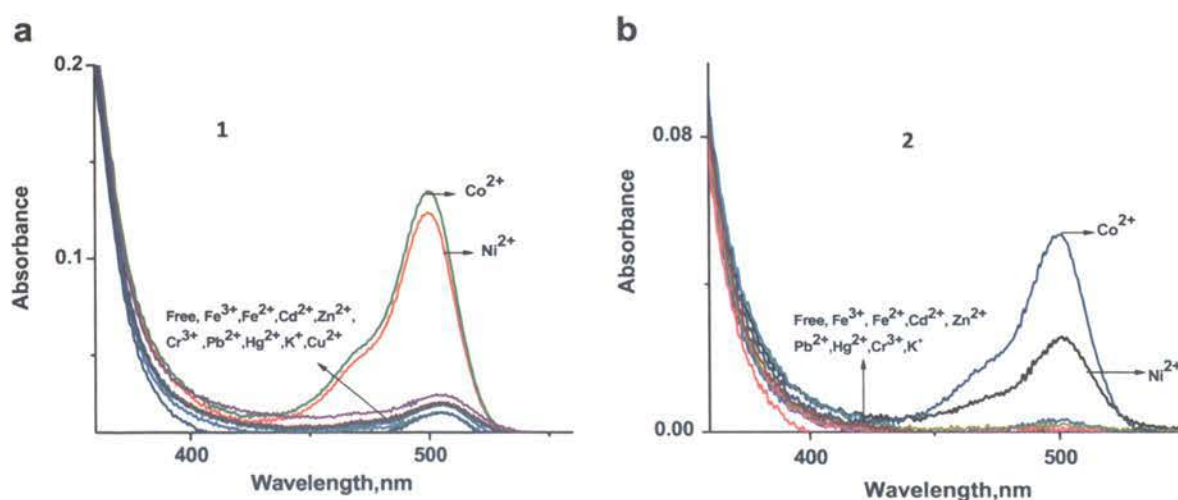


**Figure 6.9.** UV–vis absorption spectra of **1** and **2**. Respectively, **1** and **2** (a and b) (10  $\mu\text{M}$ ) upon addition of respective metal ions (1 equiv) in DMSO–water (2% DMSO) at pH 7.5 in aqueous solution.

The compounds are very weakly fluorescent in solution. Fluorescence intensity changes of **1** and **2** (10  $\mu\text{M}$ ) upon the addition of metal ions (10  $\mu\text{M}$ , 1 equiv) in aqueous solution showed a remarkable sensitivity and selectivity toward  $\text{Co}^{2+}$  and  $\text{Ni}^{2+}$  (Figure 6.10). The observed fluorescence enhancement at 515 nm ( $\lambda_{\text{ex}} = 470 \text{ nm}$ ) was over

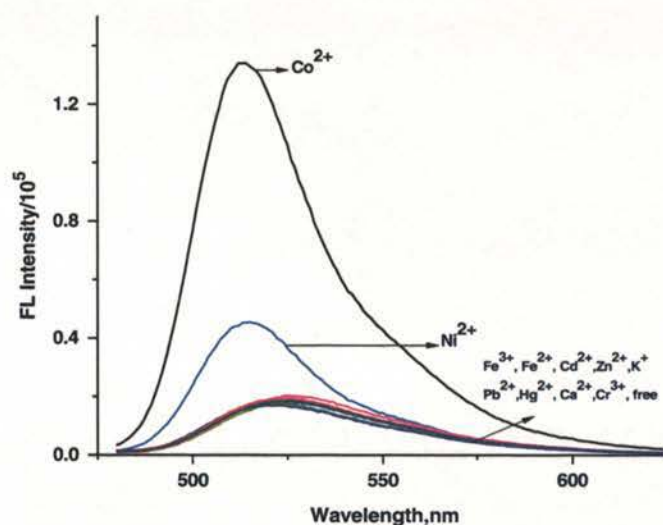


**Figure 6.10.** Fluorescence emission changes in **1**. Compound **1** (10  $\mu\text{M}$ ), upon addition of different metal ions (1 equiv) in 2% DMSO–water at pH 7.5 (excitation at 470 nm).

200-fold, which is extremely high compared to other metals. Saturation of the fluorescence signal occurred at 100  $\mu\text{M}$  of  $\text{Co}^{2+}$ . Interestingly, the 2- $\text{Ni}^{2+}$  complex was not fluorescent at all. But, the absorption enhancement and visible color change make it a selective sensor for  $\text{Ni}^{2+}$ . To evaluate the selectivity, compounds **1** and **2** were treated with various common metal ions including  $\text{Ca}^{2+}$ ,  $\text{K}^+$ ,  $\text{Fe}^{3+}$ ,  $\text{Fe}^{2+}$ ,  $\text{Pb}^{2+}$ ,  $\text{Co}^{2+}$ ,  $\text{Zn}^{2+}$ ,  $\text{Cd}^{2+}$ ,  $\text{Cr}^{3+}$ ,  $\text{Hg}^{2+}$ , or  $\text{Ni}^{2+}$  ions. The metal ions only induced minimum perturbation in the fluorescence spectra. To explore the utility of **1** as a cation-selective chromogenic

chemosensor, a competition experiment was carried out by adding 20  $\mu\text{M}$   $\text{Co}^{2+}$  to a solution of **1** in the presence of selected other cations (each at 20  $\mu\text{M}$ ). The competing cations alone did not lead to significant absorption changes of **1**. However, additions of **2** equiv of  $\text{Co}^{2+}$  to the solution produced the spectral and color changes characteristic of  $\text{Co}^{2+}$ . When the colored, **1**- $\text{Co}^{2+}$  solution was treated with 1.0  $\text{mmol L}^{-1}$  EDTA (1 equiv), the yellow color almost disappeared, indicating that the coordination of the sensor with  $\text{Co}^{2+}$  is chemically reversible. Additional EDTA eliminated the color completely, indicating complete removal of the metal ion from the sensor binding pocket. The 1:1 stoichiometry of each sensor was confirmed by the Job's plot of the fluorescence changes. From a fluorescence titration, the association constant of **1** with  $\text{Co}^{2+}$  and  $\text{Ni}^{2+}$  was observed to be  $2.1 \times 10^4$  and  $4.5 \times 10^3 \text{ M}^{-1}$ , respectively.

In conclusion, we have synthesized two new fluorescent chemosensors **1** and **2** that are very stable in aqueous solution for more than a month. Sensor **1** showed high sensitivity and selectivity toward  $\text{Co}^{2+}$  and  $\text{Ni}^{2+}$  over other interference cations. Sensor **2** was also very selective for  $\text{Co}^{2+}$  and  $\text{Ni}^{2+}$ . Even though it is non fluorescent, it is highly colored and the high absorption enhancement enables the selective identification of  $\text{Ni}^{2+}$  over other metal ions.

## 6.5. CONCLUSION

The use of spirocyclic derivatives of rhodamine and fluorescein dyes are extremely versatile and promising for the fluorescent enhancement structural change of the ring-opening process. Optical detection of metal ions as well as organophosphate compounds is of interest for environmental as well as biological detection. Here we have



produced xanthene spirolactam systems selective and sensitive for  $\text{Cr}^{3+}$ ,  $\text{Ni}^{2+}$ ,  $\text{Co}^{2+}$  and DCP, expanding the application possibilities of this class of compounds for not only fluorescence, but also visible detection. Structural characterization by X-ray diffraction elucidated the possible binding pocket of the similar xanthene derivatives to be in the area between the carbonyl-O, imine-N and the O,S, or N of the heterocyclic 5-membered ring. While the crystal structures indicate alternate conformations in the solid state than expected in the liquid-binding state, the structures combined do provide a picture of the amount of geometric flexibility of the binding pocket to interact with a variety of substrates. The electronic affects of the varied imine moieties provide the added selectivity for the various analytes.

**BIBLIOGRAPHY**

- [1] Garcia, Y.; Kahn, O.; Rabardel, L.; Chansou, B.; Salmon, L.; Tuchagues, J.P., *Inorg. Chem.* **38**:4663-4670, (1999).
- [2] Nehei, M.; Shiga, T.; Maeda, Y.; Oshio, H., *Coordination Chemistry Reviews* **251**:2606-2621 (2007).
- [3] Shongwe, M.S.; Al-Rashdi, B.A.; Adams, H.; Morris, M.J.; Mikuriya, M.; Hearne, G. *Inorg. Chem.* **46**:23 9558-9568, (2007).
- [4] Kohler, L.; Schoffers, E.; Driscoll, E.; Zeller, M.; Schmiesing, C., *Chirality*, **24**:245–251 (2012).
- [5] Fondo, M.; Garcia-Deibe, A.M.; Ocampo, N.; Sanmartin, J.; Bermjo, M.R., *Dalton Trans.*, 4260-4270, (2006).
- [6] Cremades, E.; Cauchy, T.; Cano, J.; Ruiz, E., *Dalton Trans.* 5873-5878, (2009).
- [7] Mukherjee, P.; Biswas, C.; Drew, M.; Ghosh, A., *Polyhedron*, **26**:3121-3128, (2007).
- [8] Mukherjee, P.; Drew, M.G.B.; Gomez-Garcia, C.J.; Ghosh, A. *Inorg. Chem.* **48**: 4817-4827, (2009).
- [9] Butcher, R.J.; O'Conner, C.J.; Sinn, E., *Inorg. Chem.* **20**: 3486-3493, (1981).
- [10] Aromi, G.; Brechin, E., *Struct. Bonding*, **122**:1, (2006).
- [11] Cremades, E.; Cano, J.; Ruiz, E.; Rajaraman, G.; Milios, C.J.; Brechin, E.K., *Inorg. Chem.* **48**:16, 8012-9, (2009).
- [12] Weyhermuller, T.; Wagner, R.; Hkanra, S.; Chadhuri, P. *Dalton Trans.* 2536-2546, (2005).
- [13] Assmus, A. Early History of X Rays. *SLAC Beamline*. **25**(2):10-24 (1995).
- [14] Stumm von Bordwehr, R.A. History of the X-ray Absorption Fine Structure. *Ann. Phys. Fr.* **14**: 377-466 (1989).
- [15] de Broglie, M., *Comptes Rendus* **157**: 924-926 (1913).
- [16] Glusker, J.P. Trueblood, K.N. *Crystal Structure Analysis: A Primer*. 2<sup>nd</sup> Ed. Oxford University Press. Oxford, England.(1985).
- [17] Lonsdale, K.. *Proceedings of the Royal Society of London. Series A: Mathematical, Physical and Engineering Sciences* **123**: 494-515 (1929).
- [18] Hodgkin, D.C.; Pickworth, J.; Robertson, J.H.; Trueblood, K.N.; Prosen, R.J.; White, J.G., *Nature*. **176**: 325-8 (1955).

- [19] Kendrew, J.C.; Bodo, G.; Dintzis, H.M.; Parrish, R.G.; Wyckoff, H.; Phillips, D.C., *Nature*. **181**(4610) 662-6 (1958).
- [20] Giancoli, D.C. *Physics for Scientists and Engineers, 3<sup>rd</sup> Ed.* Prentice Hall, Upper Saddle River, New Jersey, 2000.
- [21] von Laue, M. Röntgenstrahlinterferenzen. *Physikalische Zeitschrift*, **14**(22/23): 1075, (1913).
- [22] Bragg, W.H.; Bragg, W.L. *X-rays and Crystal Structure*. G. Bell and Sons, London, 191.
- [23] West, A. R. *Basic Solid State Chemistry, 2<sup>nd</sup> Ed.* John Wiley & Sons, West Sussex, England, 1999.
- [24] International Tables for X-Ray Crystallography, Volume III, Lonsdale, K. Ed. The Kynoch Press, Birmingham, England. (1968).
- [25] Mueller, P. *Crystal Structure Analysis, Spring 2010*. (Massachusetts Institute of Technology: MIT OpenCourseWare), <http://ocw.mit.edu> (Accessed January 5, 2012). License: Creative Commons BY-NC-SA.
- [26] Lake, C.; Craven, B.M. *Lecture Notes: 2011 ACA Summer Course in Small Molecule Crystallography*, Revision 5, 2003.
- [27] Bennett, D.W. *Understanding Single-Crystal X-Ray Crystallography*. Wiley-VCH GmbH & Co. Weinheim. 2010.
- [28] Cambi, L.; Szego, L. *Ber* 66 (1933) 656.
- [29] Galet, A.; Gaspar, A.B.; Munoz, M.C.; Real, J.A., *Inorg. Chem.* **45**:4413-4422 (2006).
- [30] Maeda, Y.; Tsutsumi, N.; Takashima, Y., *Inorg. Chem.* **23**: 2440-2447 (1984).
- [31] Frederick, F.C.; Coleman, W.M.; Taylor, L.T., *Inorg. Chem.* **22**: 792-795 (1983).
- [32] Wang, N., *Acta Cryst.* **E61**: m1304-m1306 (2005).
- [33] Sun, Y., *Acta Cryst.* **E61**: m335-m337 (2005).
- [34] Ma, J.; Wu, T.; She, X.; Pan, X., *Acta Cryst.* **E61**: m695-m696 (2005).
- [35] O'Reilly, R.K.; Gibson, V.C.; White, A.J.P.; Williams, D.J., *J. Am. Chem. Soc.* **125**: 8450-8451 (2003).
- [36] Gibson, V.C.; O'Reilly, R.K., US Patent 2006/0258867 A1, PCT No. PCT/GB04/01071 Nov. 16, 2006.

- [37] Viswanathan, R.; Palaniandavar, M.; Balasubramanian, T.; Muthiah, P.T., *Dalton Trans.* 2519-2525 (1996).
- [38] Oehmke, R.W.; Bailar, J.C. *J. Inorg. Nucl. Chem.*, **27**:2209 (1965).
- [39] Imbert, C.; Hrachlan, H.P.; Lanzmaster, M.; Heeg, M.J. Hryhorczuk, L.M. McGarvey, B.R.; Schlegel, B.; Verani, C.N., *Inorg. Chem.* **44**(21): 7414-7422 (2005).
- [40] Tang, J.; Costa, J.S.; Smulders, S.; Molnar, G.; Bousseksou, A.; Teat, S.J.; Li, Y.; Albada, G.A.; Gamez, P.; Reedijk, J., *Inorg. Chem.* **48**(5): 2128-2135 (2009).
- [41] Kahn, O.; Martinez, J., *Science*, **279**:44-48 (1998).
- [42] Kahn, O.; Martinez, C.J. *Science* **279**:44-48 (1998).
- [43] Bonhommeau, S.; Molnar, G.; Galet, A.; Zwick, A.; McGarvey, J.A.R.; Bousseksou, A. *Angew. Chem. Int. Ed.* **44**(26): 4069-4073 (2005).
- [44] Wreugdenhi, W.; et al. *Polyhedron* **9**: 2971 (1990).
- [45] Cobo, S.; Ostrovskii, S.; Bonhommeau, L.; Vendier, G.M.; Salmon,; Tanaka, K.; Bousseksou, A. *J. Am. Chem. Soc.* **130**: 9019-9024 (2008).
- [46] Wang, S.; Ferbinteanu, M.; Marinescu, C.; Dobrinescu, A.; Ling, Q.; Huang, W., *Inorg. Chem.* **49**: 9839-9851 (2010).
- [47] Gaspar, A.; Munoz, M.C.; Niel, V.; Real, J.A. [CoII94-terpyridone)<sub>2</sub>]<sub>2</sub>X<sub>2</sub>: a novel cobalt(II) spin crossover system. *Inorg. Chem.* **40**: 9-10 (2001).
- [48] Kilner, C.; Halcrow, M., *Dalton Trans.* **39**: 9008-9012 (2010).
- [49] Kahn, O. *Molecular Magnetism*, Wiley-VCH, Weinheim, 1993, p 10.
- [50] Sorai, M.; Seki, S. *J. Phys. Chem. Solids* **35**:555 (1974).
- [51] Bousseksou, A.; Molnar, G.; Matouzenko, G., *Eur. J. Inorg. Chem.* 4353-4369 (2004).
- [52] Gutlich, P.; Ksenofontov, V.; Gaspar, A., *Coord. Chem. Rev.* **249**: 1811-1829 (2005).
- [53] Molnar, G.; Niel, V.; Real, J.A.; Dubrovinsky, L.; Bousseksou, A.; McGarvey J.J. *J. Phys Chem. B* **107**: 3149 (2003).
- [54] Juhasz, G.; Hayami, S.; Sato, O.; Maeda, Y., *Chemical Physics Letters* **364**: 164-170 (2002).
- [55] Decurtins, S.; Gutlich, P.; Kohler, C.P.; Spiering, H.; Hauser, A. *Phys. Lett.* **105**:1 (1984).

- [56] McGarvey, J.J.; Lawthers, L. *J. Chem. Soc. Chem. Commun.* 906 (1982).
- [57] Lawthers, I.; McGarvey, J.J.; *J. Am. Chem. Soc.* **106**: 4280 (1984).
- [58] Hauser, A. in Gutlich, P.; Goodwin, H.A. (Eds.) Spin Crossover in Transition Metal Compounds Vol II, Springer, *Top. Curr. Chem.* **234**:155 (2004).
- [59] Hauser, A. *Top. Curr. Chem.* **234**:155 (2004).
- [60] Funck, K.F.; Prosvirin, A.V.; Mathoniere, C.; Clerac, R.; Dunbar, K.R., *Inorg. Chem.* **50**: 2782-2789 (2011).
- [61] Sour, A.; Boillot, M.L. Riviere, R.; Lesot, P. *Eur. J. Inorg. Chem.* 2117 (1999).
- [62] Ivanova, T.A.; Ovchinnikov, I.V.; Turanov, A.N., *Physics of the Solid State* **49**(11): 2132-2137 (2007).
- [63] Sorai, M.; Maeda, Y.; Oshio, H. *J. Phys. Chem. Solids* **51**:941 (1990).
- [64] Maeda, M.; Takashima, Y.; Nishida, Y. *Bull. Chem. Soc. Jpn.* **49**: 2427 (1976).
- [65] Sorai, M.; Seki, S. *J. Phys. Soc. Jpn.* **33**: 575 (1972).
- [66] Slichter, C.P.; Drickamer, H.G. *J. Chem. Phys.* **56**:2141 (1972).
- [67] Tido, E. W. Y.; Faulmann, C.; Roswanda, R.; Meetsma, A.; Koningsbruggen, P.J., *Dalton Trans.* **39**: 1643-1651 (2010).
- [68] Hayami, S.; Kawahara, T.; Juhasz, G.; Kawamura, K.; Uehashi, K.; Sato, O. *J. Am. Chem. Soc.* **123**: 11644 (2001).
- [69] Haddad, M.S.; Federer, W.D.; Lynch, M.W.; Hendrickson, D.N. *Inorg. Chem.* **20**:123 (1981).
- [70] Yamada, M.; Ooidemizu, M.; Ikuta, Y.; Osa, S.; Matsumoto, N.; Iijima, S.; Kojima, M.; Dahan, F.; Tuchagues, J.P. *Inorg. Chem.* **42**: 8406-8416 (2003).
- [71] Conti, A.J.; Chadhu, R.K.; Sena, K.M.; Rheingold, A.L.; Hendrickson, D.N., *Inorg. Chem.* **31**: 2670-2680 (1993).
- [72] Jameson, G.N.L.; Werner, F.; Bartel, M.; Absmeier, A.; Reissner, M.; Kitchen, J.A.; brooker, S.; Caneschi, A.; Carbonera, C. Letard, J.F.; Linert, W., *Eur. J. Inorg. Chem.* 3948-3959 (2009).
- [73] Hayami, S.; Maeda, Y. *Inorg. Chim. Acta* **225**:181 (1997).
- [74] Oshio, H.; Kitazaki, K.; Mishiro, K.J.; Kato, N.; Maeda, M.; Takashima, T. *Dalton Trans.* 1341 (1987).

- [75] Ikuta, Y.; Ooidemizu, M.; Yamahata, Y.; Yamada, M.; Osa, S.; Matsumoto, N.; Iijima, S.; Sunatsuki, Y.; Kojima, M.; Daham, F.; Tuchangues, J.P. *Inorg. Chem.* **42**:7001-7017 (2003).
- [76] Roux, C.; Zarembowitch, J.; Gallois, B.; Granier, T.; Claude, R., *Inorg. Chem.* **33**: 2273-9 (1994).
- [77] Tweedle, M.F.; Wilson, L.J. *J. Am. Chem. Soc.* **98**:4824 (1976).
- [78] Nakajima, H.; Takana, T.; Kobayashi, H.; Tsujikawa, I. *Inorg. Nucl. Chem. Lett.* **12**:689 (1976).
- [79] Kunze, K.R.; Perry, D.L.; Wilson, L.J. *Inorg. Chem.* **16**:594 (1977).
- [80] Floquet, S.; Boillot, M.L.; Rivieree, E.; Varret, F.; Boukheddaden, K.; morineau, D.; Negrier, P. *New J. Chem.* **27**:341 (2003).
- [81] Griffen, M.; Shakespeare, S.; Shepherd, H.J.; Harding, C.J.; Letard, J.F.; Desplanches, D.; Goeta, A.E.; Howard, J.A.K.; Powell, A.K.; Mereacre, V.; Garcia, Y.; Naik, A.D.; Muller-Bunz, H.; Morgan, G.G., *Angew. Chem. Int. Ed.* **50**: 896-900 (2011).
- [82] Gamez, P.; Costa, J.S.; Quesada, M.; Guillem, A., *Dalton Trans.* 7845-7853 (2009).
- [83] Holland, J.M.; McAllister, J.A.; Kilner, C. A.; Thornton-Pett, M.; Bridgeman, A.J.; Halcrow, M.A., *Dalton Trans.* 548-554 (2002).
- [84] Maeda, Y.; Noda, Y.; Oshio, H.; Takashima Y.; Matsumoto, N. *Hyperfine Interact.* **84**:471 (1994).
- [85] Matsumoto, N.; Ohta, S.; Yoshimura, C.; Ohyoshi, A.; Kohata, S.; Okawa, H.; Maeda, Y. *Dalton Trans.* 2575 (1985).
- [86] Mueller, P.; Herst-Irmer, R.; Spek, A.L.; Schneider, T.R.; Sawaya, M.R. *Crystal Structure Refinement: A Crystallographer's Guide to SHELXL*, P. Müller, Ed., Oxford University Press, 2006.
- [87] Spek, A.L. (2003). *J. Appl. Cryst.* **36**, 7-13. and Spek, A.L. (2009). *Acta Cryst.* **D65**, 148-155
- [88] Van der Sluis, P.; Spek, A. L.; *Acta Crystallographica. Section A: Foundations of Crystallography* **A46**(3), 194-201, (1990).
- [89] Marchivie, M.; Guionneau, P., Letard, J.F. and Chasseau, D. *Acta Cryst.* **B59**: 479-486, (2003).

- [90] Collet, E.; Boillot, M.L.; Herbert, J.; Moisan, N.; Servol, M.; Lorenc, M.; Toupet, L.; Buron-Le Cointe, M.; Tissot, A. and Sainton, J., *Acta Cryst.* **B65**, 474-480, (2009).
- [91] Dorbes, S.; Valade, L.; Real, J.A.; Falmann, V. *Chem Commun.* **59**, (2005).
- [92] Sim, P.; Sinn, E.; Petty, R.H.; Merrill, C.L.; Wilson, L.J. *Inorg. Chem.* **20**: 1213, (1981).
- [93] Timkin, M.D.; Hendrickson, D.N.; Sinn, E. *Inorg. Chem.* **24**:3947 (1985).
- [94] Mueller, P. *Crystal Structure Analysis, Spring 2010*. (Massachusetts Institute of Technology: MIT OpenCourseWare), <http://ocw.mit.edu> (Accessed January 5, 2012). License: Creative Commons BY-NC-SA.
- [95] Glusker, J.P. Trueblood, K.N. *Crystal Structure Analysis; A Primer. 2<sup>nd</sup> Ed.* Oxford University Press. Oxford, England,(1985).
- [96] Flack, H.D. *Acta Cryst.* **A39**: 876-881, (1983).
- [97] Spek, A.L. The Platon Crystallographic Package Documentation- Version 29-09-2010.(2010) [www.cryst.chem.uu.nl/platon/PLATON-MANUAL.pdf](http://www.cryst.chem.uu.nl/platon/PLATON-MANUAL.pdf), (Accessed: 12Jan2012).
- [98] Hooft, R, Straver, L. & Spek, A.L. (2008) *J. Appl. Cryst.*, **41**, 96-103.
- [99] Hooft, R. Absolute Structure, ©2007-2011, <http://www.absolutestructure.com/inbrief>, (Accessed: 29Feb2012).
- [100] Giacovazzo, C. ed. (1992). *Fundamentals in Crystallography*, I.U.Cr. & O.U.P. Oxford, UK.
- [101] Mueller, P., *Crystal Structure Refinement Fall 2009*. (Massachusetts Institute of Technology: MIT OpenCourseWare), <http://ocw.mit.edu> (Accessed January 5, 2012). License: Creative Commons BY-NC-SA.
- [102] G. M. Sheldrick, *SHELXTL Reference Manual*, **1997**, Bruker-AXS, Inc., Madison, WI
- [103] Herbst-Irmer, R. *Twin Refinement with SHELXL*. <http://shelx.uni-ac.gwdg.de/~rherbst/twin.html>. (Accessed 05Jan2012).
- [104] Noll, B.; Ruf, M., *Using APEX2 to Analyze Twinned Crystals*, Bruker AXS Inc. Webinar, 03May 2011.
- [105] Cooper, R. I.; Gould, R.O.; Parsons,S.; Watkin, D.J., *J. Appl. Cryst.* **35**:2, 168-174, (2002).

- [106] Sheldrick, G.M.; CELL NOW program for unit cell determination, Göttingen University, <http://shelx.uni-ac.gwdg.de/SHELX/>, (Accessed 05Jan2012).
- [107] CSD Space Group Statistics 01Jan2012, The Cambridge Crystallographic Data Centre, 12 Union Road, Cambridge, CB2 1EZ, UK, +44 1223 336408 [http://www.ccdc.cam.ac.uk/products/csd/statistics/stats\\_sgrankorder\\_Jan2012.pdf](http://www.ccdc.cam.ac.uk/products/csd/statistics/stats_sgrankorder_Jan2012.pdf), (Accessed 29Mar2012).
- [108] M. Murrie, *Chem. Soc. Rev.*, 2010, 39, 1986-1995.
- [109] M. Moragues-Cnovas, M. Helliwell, L. Ricard, E. Rivire, W. Wernsdorfer, E. K. Brechin, T. Mallah, *Eur. J. Inorg. Chem.* 2004,2219.
- [110] G. Aromi, S. Parsons, W. Wernsdorfer, E. K. Brechin, E. J. L. McInnes, *Chem. Commun.* 2005, 40, 5038.
- [111] E.-C. Yang, W. Wernsdorfer, L. N. Zakharov, Y. Karaki, A. Yamaguchi, R. M. Isidro, G.-D. Lu, S. A. Wilson, A. L. Rheingold, H. Ishimoto and D. N. Hendrickson, *Inorg. Chem.*, 2006, 45, 529.
- [112] R. T.W. Scott, L. F. Jones, I. S. Tidmarsh, B. Breeze, R.H. Laye, J. Wolowska, D. J. Stone, A. Collins, S. parsons, W. Wernsdorfer, G. Aromi, E.J.L. McInnes and E. K. Brechin, *Chem. Eur. J.*, 2009, 15, 12389-12398.
- [113] Costes, J. P.; Clemente-Juan, J. M.; Dahan, F.; Dumestre, F.; Tuchagues, J. P. *Inorg. Chem.* 2002, 41, 2886.
- [114] Chandrasekhar, V.; Murugesan Pandian, B.; Azhakar, R.; Vittal, J. J.; Clerac, R. *Inorg. Chem.* 2007, 46, 5140.
- [115] J. R. Friedman, M. P. Sarachik, J. Tejada and R. Ziolo, *Phys. Rev. Lett.*, 1996, 76, 3830.
- [116] A.-L. Barra, P. Debrunner, D. Gatteschi, C. E. Schulz and R. Sessoli, *Europhys. Lett.*, 1996, 35, 133-138.
- [117] S. Hill, S. Datta, J. Liu, R. Inglis, C. J. Milios, P. L. Feng, J.J. Henderson, E. del Barco, E. K. Brechin and D. N. Hendrickson, *Dalton Trans.*, 2010, 39, 4693-4707.
- [118] J. Tang, I. Hewitt, N. T. Madhu, G. Chasanet, W. Wernsdorfer, C. E. Anson, C. Benelli, R. Sessoli and A. K. Powell, *Angew. Chem., Int. Ed.*, 2006, 45, 1729.
- [119] P. Chaudhuri, *Coord. Chem. Rev.*, 2003, 243, 143; P. Chaudhuri, M. Hess, E. Rentschler, T. Weyhermuller and U. Flörke, *New J. Chem.*, 1998, 553.
- [120] S. Brooker, J. A. Kitchen, *Dalton Trans.*, 2009, 7331-7340.



- [121] Atkins, P.W.; Overton T.L.; Rourke, J.P.; Weller, M.T.; Armstrong F.A. Shriver and Atkins' Inorganic Chemistry, 5<sup>th</sup> Ed. W.H Freeman and Company, New York, NY, 2010.
- [122] Pascal, P. *Ann. Chim. Phys.* **19**:5 (1910) ; **25**:289 (1912); **24**:218 (1914).
- [123] Miessler, G.L.; Tarr, D.A. Inorganic Chemistry 2<sup>nd</sup> Ed. Prentice Hall, Upper Saddle River, NJ, 1999.
- [124] Thanyasiri, T. Structural and Magnetic Properties of some Mono- and polynuclear transition-metal, Schiff-base complexes. Ph.D. Dissertation, Dept. of Chemistry, University of Virginia, (1988).
- [125] Mabbs, F.E.; Machin, D.J.. Magnetism and Transition Metal Complexes. Chapman and Hall Publishers, London (1973).
- [126] White, D.P.; Anthony, J.C.; Oyefeso, A.O. , *J. Org. Chem.* **64**: 7707-7716, (1999).
- [127] Landis, C.R.; Nelson, R.C.; Jin, W.; Bowman, A.C., *Organometallics*, **25**: 1377-1391, (2006).
- [128] Guzei, I.A.; Wendt, M., *Dalton Trans.*, **33**: 3991-3999, (2006).
- [129] Bartholomew, J.; Fernandez, A.L.; Lorsbach, B.A.; Wison, M.R.; Prock, A.; Giering, W.P., *Organometallics*, **15**:295-301 (1996).
- [130] Paschke, R.; Liebsch, S.; Tschierske, C.; Oakley, M.; Sinn, E., *Inorg. Chem.* **42**:25, 8230-8240, (2003).
- [131] Bill, E. Program package julX Version 1.4.1, MPI for Bioinorganic Chemistry, Muhlheim/Ruhr (Germany), 2008.
- [132] Munakata, M.; Kitagawa, S.; Miyazima, M., *Inorg Chem.* **24**:11, , 1638-1643) (1985).
- [133] Butcher, R.J.; Jasinski, J.; Mockler, G.M.; Sinn, E., *J.C.S. Dalton Trans.* **12**:1099-1102, (1976).
- [134] Bardwell, D.A.; Jeffery, J.C.; Ward, M.D., *Inorganica Chimica Acta*, 236:125-130, (1995).
- [135] Hoshino, N.; Ito, T.; Nihei, M.; Oshio, H., *Synthetic Metals*, 137:1309-1310, (2003).
- [136] Rodriguez, L.; Labisbal, E.; Sousa-Pedrares, A.; Garcia-Vazquez, J.A.; Romero, J.; Duran, M.L.; Real, J., Sousa, A., *Inorg. Chem.* 45:19, 7903-7914, (2006).
- [137] Kubas, G. *Acc. Chem. Res.* **1988**, 21, 120-128.

- [138] Yamaguchi, K.; Koshino, S.; Akagi, F.; Suzuki, M.; Uehara, A.; Suzuki, S. *J. Am. Chem. Soc.* **1997**, *119*, 5752-5753.
- [139] Kolodziej, A. F. In *Progress in Inorganic Chemistry*; Karlin, K. D., Ed.; Wiley: New York, 1994; pp 494-597.
- [140] Yuchi, A.; Murakami, H.; Shiro, M.; Wada, H., *Bull. Chem. Soc. Jpn.*, **65**:3362-3373, (1992).
- [141] Burkhardt, A.; Spielberg, E.T.; Simon, S.; Gorls, H.; Buchholz, A.; Plass, W.; *Chem. Eur. J.* **15**:1261-1271 (2009).
- [142] Ilina, E.; Kessleer, V.G., *Polyhedron*, **24**:3052-3056 (2005).
- [143] Kogan, V.A.; Lukov, V.V.; Shcherbakov, I.N., *Russ. J. Coord. Chem.* **36**:6, 401-429, (2010).
- [144] Ohashi, A.; Ito, H.; Kanai, C.; Imura, H.; Ohashi, K. *Talanta*. 2005, *65*, 525.
- [145] Liang, Z.-Q.; Wang, C.-X.; Yang, J.-X.; Gao, H.-W.; Tiang, Y.-P.; Tao, X.-T.; Jiang, M.-H. *New. J. Chem.* 2007, *31*, 906.
- [146] Lunvongsa, S.; Oshima, M.; Motomizu, S. *Talanta* 2006, *68*, 969.
- [147] Tesfaldet, Z. O.; van Staden, J. F.; Stefan, R. I. *Talanta* 2004, *64*, 1189.
- [148] Gomes, D. M. C.; Segundo, M. A.; Lima, J. L. F. C.; Rangel, A. O. S. S. *Talanta* 2005, *66*, 703.
- [149] Bobrowski, A.; Nowak, K.; Zarebski, *J. Anal. Bioanal. Chem.* 2005, *382*, 1691.
- [150] de Silva, A. P.; Gunaratne, H. Q. N.; Gunnlaugsson, T.; Huxley, A. J. M.; McCoy, C. P.; Rademacher, J. T.; Rice, T. E. *Chem. Rev.* 1997, *97*, 1515.
- [151] Chen, X.; Tian, X.; Shin, I.; Yoon, *J. Chem. Soc. Rev.* 2011, *40*, 4783.
- [152] Czarnik, A. W. *Fluorescent Chemosensors for Ion and Molecule Recognition*; American Chemical Society: Washington, DC, 1992.
- [153] Lakowicz, J. R. *Principles of Fluorescence Spectroscopy*; Plenum Press: New York, 1983.
- [154] Lakowicz, J. R. *Fluorescence spectroscopy of biomolecules*. In *Encyclopedia of Molecular Biology and Molecular Medicine*; Meyers, R. A., Ed.; VCH Publishers: New York, 1995.
- [155] Szmazinski, H.; Gryczynski, I.; Lakowicz, J. R. *Photochem. Photobiol.* 1993, *58*, 341.

- [156] Yanagida, T.; Ishii, Y. *Single Molecule Dynamics in Life Science*; Wiley-VCH: Weinheim, Germany, 2009.
- [157] Weerasinghe, A. J.; Schmiesing, C.; Varaganti, S.; Ramakrishna, G.; Sinn, E. *J.Phys. Chem. B* 2010, 114, 9413;
- [158] Weerasinghe, A. J.; Schmiesing, C.; Sinn, E. *Tetrahedron Lett.* 2009, 50, 6407.
- [159] Chen, X.; Jou, M. J.; Lee, H.; Kou, S.; Lim, J.; Nam, S.-W.; Park, S.; Kim, K.-M.; Yoon, J. *Sens. Actuators, B* 2009, 137, 597.
- [160] Dujols, V.; Ford, F.; Czarnik, A. W. *J. Am. Chem. Soc.* 1997, 119, 7386.
- [161] Chen, X.; Pradhan, T.; Wang, F.; Kim, J.S.; Yoon, J., *Chem. Rev.* 2012, 112, 1910–1956.
- [162] Sarkar, M.; Banthia, S.; Samanta, A. *Tetrahedron Lett.* 2006, 47, 7575;
- [163] Latva, S.; Jokiniemi, J.; Peraniemi, S.; Ahlgren, M. *J. Anal. At. Spectrom.* 2003, 18,84;
- [164] Huang, K.; Yang, H.; Zhou, Z.; Yu, M.; Li, F.; Gao, X.; Yi, T.; Huang, C. *Org.Lett.* 2008, 10, 2557
- [165] Singh, A. K.; Gupta, V. K.; Gupta, B. *Anal. Chim. Acta* 2007, 585, 171.
- [166] Zayed, M.; Norman, T. *Plant Soil* 2003, 249, 139.
- [167] Mao, J.; Wang, L.; Dou, W.; Tang, X.; Yan, Y.; Liu, W. *Org. Lett.* 2007, 9, 4567.
- [168] Zhou, Z.; Yu, M.; Yang, H.; Huang, K.; Li, F.; Yi, T.; Huang, C. *Chem. Commun.* 2008, 3387.
- [169] Connors, K. A. *Binding Constants-The Measurement of Molecular Complex Stability*; John Wiley & Sons: New York, 1987.
- [170] Zhan, X. Q.; Qian, Z. H.; Zheng, H.; Su, B. Y.; Lan, Z.; Xu, J. G. *Chem. Commun.* 2008, 1859;
- [171] de Jong, R. H. *Anesth. Analg.* 2003, 96, 819.
- [172] Ember, L. R. *Chem. Eng. News* 1994, Aug., 1, 26;
- [173] Pavlov, V.; Xiao, Y.; Wilner, I. *Nano. Lett.* 2005, 4, 649.
- [174] Zhang, S.-W.; Swager, T. M. *J. Am. Chem. Soc.* 2003, 125, 3420;
- [175] Dale, T. J.; Rebek, J., Jr. *J. Am. Chem. Soc.* 2006, 128, 4500;
- [176] Rathfon, J. M.; AL-Badri, Z. M.; Shunmugam, R.; Berry, S. M.; Pabba, S.; Keynton, R. S.; Cohn, R. W.; Tew, G. N. *Adv. Funct. Mater.* 2009, 19, 689;

- [177] Knapton, D.; Burnworth, M.; Rowan, S. J.; Weder, C. *Angew. Chem., Int. Ed.* 2006, 45, 5825;
- [178] Dale, T. J.; Rebek, J., Jr. *Angew. Chem., Int. Ed.* 2009, 48, 7850.
- [179] Russell, R. J.; Pishco, M. V.; Simonian, A. L.; Wild, J. R. *Anal. Chem.* 1999, 71, 4909;
- [180] Russell, A. J.; Berberich, J. A.; Drevon, G. E.; Koepsel, R. R. *Annu. Rev. Biomed. Eng.* 2003, 5, 1;
- [181] Ashley, J. A.; Lin, C. H.; Wirsching, P.; Janda, K. D. *Angew. Chem., Int. Ed.* 1999, 38, 1793;
- [182] La Rosa, C.; Pariente, F.; Hernadex, L.; Lorenzo, E. *Anal. Chim. Acta* 1995, 308, 129;
- [183] Kumaran, S.; Morita, M. *Talanta* 1995, 42, 649.
- [184] Sohn, H.; Letant, S.; Sailor, M. J.; Trogler, W. C. *J. Am. Chem. Soc.* 2000, 122, 5399.
- [185] Yang, Y.; Ji, H.-F.; Thundat, T. *J. Am. Chem. Soc.* 2003, 125, 1124;
- [186] Hartmann-Thompson, C.; Hu, J.; Kaganove, S., N.; Keinath, S. E.; Keeley, D. L.; Dvornic, P. R. *Chem. Mater.* 2004, 16, 5357.
- [187] Khan, M. A. K.; Kerman, K.; Petryk, M.; Kraatz, H. B. *Anal. Chem.* 2008, 80, 2574.
- [188] Xiang, Y.; Tong, A.; Jin, P.; Ju, Y. *Org. Lett.* 2006, 8, 2863;
- [189] Dujols, V.; Ford, F.; Czarnik, A. W. *J. Am. Chem. Soc.* 1997, 119, 7386.
- [190] Xiang, Y.; Tong, A. *Org. Lett.* 2006, 8, 1549;
- [191] Zhang, M.; Gao, Y.; Li, M.; Yu, M.; Li, F.; Li, L.; Zhu, M.; Zhang, J.; Yi, T.; Huang, C. *Tetrahedron Lett.* 2007, 48, 3709.
- [192] Kwon, J. Y.; Jang, Y. J.; Lee, Y. J.; Kim, K. M.; Seo, M. S.; Nam, W.; Yoon, J. J. *Am. Chem. Soc.* 2005, 127, 10107.
- [193] Zhan, X. Q.; Qian, Z. H.; Zheng, H.; Su, B. Y.; Lan, Z.; Xu, J. G. *Chem. Commun.* 2008, 1859.
- [194] Huang, J.; Xu, Y.; Qian, X. *J. Org. Chem.* 2009, 74, 2167.
- [195] Wu, J. S.; Hwang, I. C.; Kim, K. S.; Kim, J. S., *Org. Lett.*, 9:907 (2007).
- [196] Han, S.; Xue, Z.; Wang, Z.; Wen, T. B., *Chem. Commun.*, 8413, (2010).

- [197] Gonc-alves, M.; Sameiro, T., *Chem. Rev.*, **109**:190, (2009).
- [198] Atilgan, S.; Ozdemir, T.; Akkaya, E. U., *Org. Lett.*, **10**:4065, (2008).
- [199] Teolato, P.; Rampazzo, E.; Arduini, M.; Mancin, F.; Tecilla, P.; Tonellato, U., *Eur. J.Chem.*, **13**: 2238 (2007).
- [200] Kim, H. J.; Hong, J.; Hong, A.; Ham, S.; Lee, J. H.; Kim, S. J., *Org. Lett.*, **10**: 1963, (2008).
- [201] Martinez, R.; Zapata, F.; Caballero, A.; Espinosa, A.; Tarraga, A.; Molina, P., *Org. Lett.*, **8**:3235, (2006).
- [202] Lim, N. C.; Pavlova, S. V.; Bruckner, C., *Inorg. Chem.*, **48**:1173, (2008).
- [203] Bricks, J. L.; Kovalchuk, A.; Trieflinger, C.; Nofz, M.; Buschel, M.; Tolmachev, A.I.; Daub, J.; Rurack, K. J., *J. Am. Chem. Soc.*, **127**:13522, (2005).
- [204] Gosh, P.; Bharadwaj, P. K. *J. Am. Chem. Soc.*, **118**: 1553, (1996).
- [205] Xiao, Y.; Qian, X., *Tetrahedron Lett.*, **44**:2087, (2003).
- [206] Callan, J. F.; de Silva, A. P.; Magri, D. C., *Tetrahedron*, **61**: 8551, (2005).

## VITA

Carla Sue Schmiesing Eribal was born in Auglaize County, Ohio. In June 2003, she received her B.S. degree cum Laude in Chemistry from Otterbein College, Westerville, Ohio. In August 2003, she joined the Department of Chemistry at the University of Missouri-Rolla (UMR). At the end of obligatory military service from 2004-2006, she returned to UMR until 2007, whereupon her research opportunity moved to Western Michigan University, Kalamazoo, Michigan. In May 2012, she received her Ph.D. in Inorganic Chemistry from the Missouri University of Science and Technology, Rolla, Missouri, USA.

Ms. Eribal has been a member of the American Chemical Society since 2003, the American Crystallographic Society since 2011 and the Pittsburgh Diffraction Society since 2010. She has presented her research at national and regional conferences, taught undergraduate and graduate courses, contributed to journal publications and collaborated with research groups both domestic and international.

### Publications

Kohler, Lars; Schoffers, Elke; Driscoll, Erin; Zeller, Matthias; Schmiesing, Carla, *Chirality* (2012), 24(3), 245-251.

Abebe, Fasil A.; Eribal, Carla Sue; Ramakrishna, Guda; Sinn, Ekkehard, *Tetrahedron Letters* (2011), 52(43), 5554-5558.

Weerasinghe AJ, Schmiesing C, Sinn E. *Tetrahedron* (2011) 67(16), 2833-2838.

Weerasinghe, Aruna J.; Schmiesing, Carla; Varaganti, Shankar; Ramakrishna, Guda; Sinn, Ekkehard *Journal of Physical Chemistry B* (2010), 114(29), 9413-9419.

Weerasinghe, Aruna J.; Schmiesing, Carla; Sinn, Ekkehard *Tetrahedron Letters* (2009), 50(46), 6407-6410.